# UNIVERSITÀ DEGLI STUDI DI PADOVA

**Dipartimento di Fisica e Astronomia "Galileo Galilei"**

**Master Degree in Physics**


**Final Dissertation**

# Monte-Carlo simulations for medical images interpretation in the context of the ISOLPHARM project


**Thesis supervisor**

**Prof. Marcello Lunardon**

**Thesis co-supervisors**

**Dr. Alberto Andrighetto**

**Dr. Alberto Arzenton**

**Prof. Giorgio Russo**

**Dr. Luca Morselli**

**Candidate**

**Davide Serafini**



**Academic Year 2021/2022**

# Abstract

The ISOLPHARM collaboration has the aim of producing a set of innovative, high specific activity, carrier-free radionuclides for radiopharmaceutical applications exploiting the ISOL technique at SPES. The success of a particular radiopharmaceutical cancer treatment relies on an accurate assessment of the tissue response and toxicity. Since biological effects are mediated by the absorbed dose, internal dosimetry is of fundamental importance because it allows for the maximization of the therapeutic effect while minimizing the radiation burden to other organs. The thesis work deals with internal absorbed dose Monte Carlo calculations based on Geant4 combined with standard and novel medical images.

For some years now, interest has been growing in the use of optical photons emitted by Cerenkov effect for diagnostic purposes. This technique, called Cerenkov luminescence imaging (CLI), could be used in a complementary fashion with PET and SPECT to produce 2D, fast and cost-effective functional images in pre-clinical and clinical settings. An innovative instrument designed for CLI, direct radioisotopic imaging (DRI) and other imaging techniques is the Bruker In-Vivo Xtreme II, available at the CAPiR Laboratory of the University of Catania.

Using this instrument, a number of CLI and DRI have been acquired for several radionuclides: Tc-99m, Ga-68. Specific phantoms have been designed and built to define the geometry of the source in a shape that allows the characterization of the spatial resolution, the contrast and other typical features of the instrument.

The experimental images will be used to validate the Geant4 simulation framework. The software will be then used to assess the performance of the instrument with the future Ag-111 loaded radiopharmaceutical, with the aim to extract the biodistribution activity and internal dose maps for the future in-vivo experiments at CAPiR expected by the end of this year.

# Sommario

La collaborazione ISOLPHARM nasce con lo scopo di produrre una gamma di radionuclidi innovativi, ad alta attività specifica per applicazioni di medicina nucleare. La produzione sarà realizzata con tecninca ISOL nel laboratorio SPES. L'efficacia clinica di questi radiofarmaci si basa su un accurato controllo della risposta dei tessuti trattati. Dato che gli effetti biologici sono mediati dalla dose assorbita, è essenziale riuscire a massimizzare l'effetto terapeutico e, allo stesso tempo, minimizzare il carico di radioattività sugli altri organi sani. Questi studi sono l'oggetto della dosimetria. Questo lavoro di tesi si occupa di calcolare la dose assorbita mediante simulazioni Monte-Carlo. Allo scopo verranno utilizzati Geant4 e immagini mediche di nuova generazione.

Recentemente, in ambito diagnostico sta crescendo l'interesse nell'uso di fotoni ottici emessi tramite effetto Cerenkov. Questa tecnica è nota come Cerenkov Luminescence Imaging (CLI). Può essere usata in ambito pre-clinico in maniera complementare a PET e SPECT per produrre immagini 2D funzionali in tempi rapidi e con costi contenuti. Bruker In-Vivo Xtreme II è uno strumento innovativo che è in grado di acquisire immagini tramite CLI, DRI ed altre tecniche. Questo strumento è stato acquistato dal laboratorio CAPiR dell'Università di Catania ed è ora a disposizione per esperimenti.

Al CAPiR abbiamo acquisito con questo strumento diverse immagini CLI e DRI per alcuni radionuclidi: Tc-99m e Ga-68. Un modello di fantoccio è stato appositamente disegnato e realizzato per poter confinare le sorgenti radioattive in volumi noti e così poi caratterizzare la risoluzione spaziale, il contrasto e altre proprietà dello strumento.

Le immagini ottenute durante l'esperimento sono state usate per ottimizzare una simulazione costruita con Geant4. Con la stessa simulazione abbiamo stimato la qualità delle immagini prese con radiofarmaci a base di Ag-111, prossimamente disponibili grazie all'avvio di SPES. Grazie a queste predizioni, intendiamo dedurre la distribuzione di attività e costruire una mappa della dose per i prossimi esperimenti in-vivo al CAPiR che sono attesi per la fine del presente anno.

# Contents

# Chapter 1

# Introduction

## 1.1 ISOLPHARM

Radioactive nuclei play an important role not only in nuclear medicine but also in astrophysics and nuclear physics. In the last decades huge efforts was made to build facilities able to deliver beams of radioactive nuclei, also referred as Radioactive Ion Beam (RIB) [1].

SPES facility at Legnaro National Laboratories (LNL) is going to produce a large variety of RIBs. Using a 40 MeV high intensity (up to 200 µA) proton beam impinging on a thick target of U-238, fission reactions will occur leading to the production of neutron rich radioactive isotopes with atomic number between 28 and 57. Ag-111 has 47 protons and 64 neutrons, thus it is one of the nuclei that will be available in this facility [2].

In general, after the radionuclide are produced, the RIB can be separated and selected using one technique among:

- In-Flight separation
- Isotope Separation On-Line (ISOL)

The latter is the technique that is going to be used by the SPES facility at LNL. Therefore, we will present its main features.

With ISOL technique, a thick target is used to produce the exotic species stopping the primary beam. The target has a very high temperature (typically 2000 °C [3]) so that the exotic nuclei produced can diffuse within the target itself and effuse toward the ion source [4].

In the last years, the possibility to produce isotopes of medical interest using ISOL technique has been proposed in the framework of newly designed facilities [5].

For instance, radioactive nuclei are contained in radiopharmaceuticals, that are one of the tools of nuclear medicine [6]. These drugs can deliver a predefined amount of radiation to target tissue in humans for diagnosis or therapy or both.

In this context, ISOLPHARM project plans to produce a plethora of high purity radionuclides for medical use. The facility that is going to host this project is the already mentioned SPES, that is under construction at LNL [7][8].

The ISOLPHARM method (that is a patent owned by the Istituto Nazionale di Fisica Nucleare (INFN) [10]) can be split in two main parts:

**ISOL** production of radionuclides using a RIB impinging on a secondary target

**PHARM** production of radiopharmaceuticals from the irradiated secondary target

An overview of the ISOLPHARM method is represented in Figure 1.1.

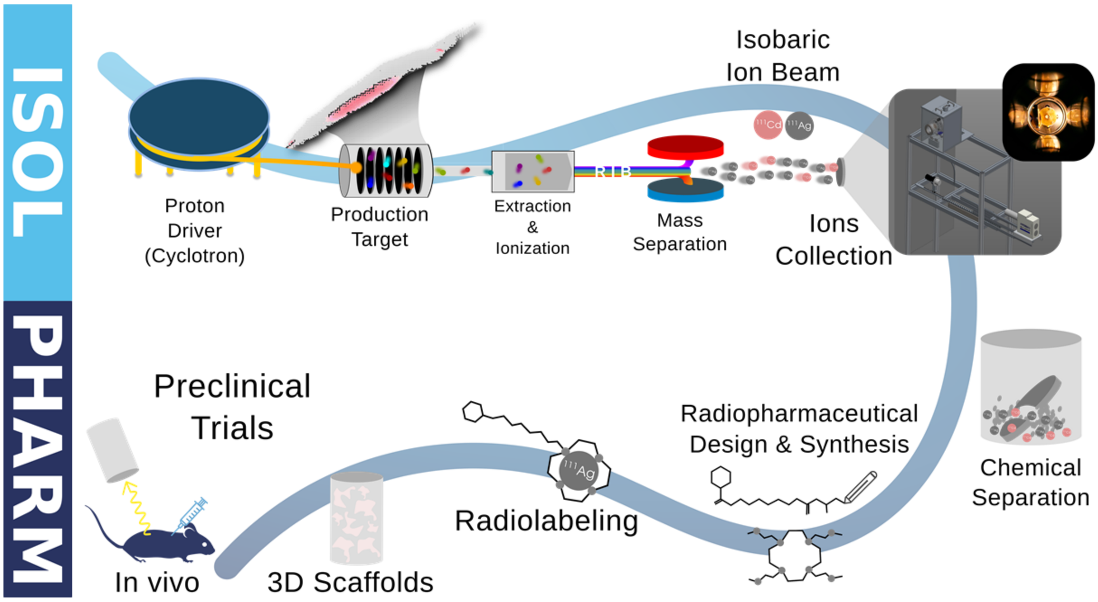


Figure 1.1: Overview of the ISOLPHARM method. The method is made of two stages: the first one involves the RIB production and purification via ISOL technique, the second one involves chemical and pharmaceutical operations to produce a radiolabeled drug. From [9].

This method involves many steps that cannot be carried out by a single figure. For this reason, ISOLPHARM is also a collaboration between people from different research fields. Engineers, physicists, chemists and druggists work together in order to finally be able to commercialize a new radiopharmaceutical.

Radiopharmaceuticals are made by several elements:

- the radionuclide that is the core of the drug
- the chelator that is a molecule able to capture the nuclide of interest
- the targeting agent whose pharmacokinetics points to the tumor
- the linker that links the chelator to the targeting agent

Recent studies are investigating the advantages of a different structure with liposomes instead of

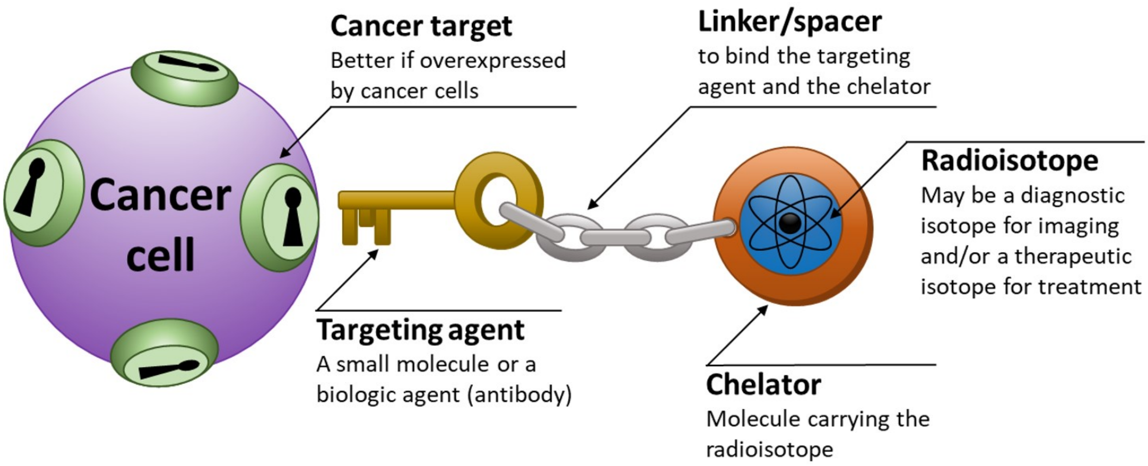


Figure 1.2: Scheme of a Radiopharmaceutical. The radioisotope is carried by the chelator that is linked to a targeting agent able to lead the radiopharmaceutical to the cancer cell. From [9]

small molecules in the role of linker. They can be charged with chelators and targeting agents. The chelators can be less powerful since the metal elements trapped in the liposome lumen do not risk to be released. Liposome structures extra-vase from the blood vessels where the porosity is increased, that is, in tumors. Figure 1.2 represents a small molecule radiopharmaceutical.

Many radionuclides can potentially be produced at SPES but Ag-111 is the most promising for cancer therapy thanks to its favorable decay properties [11]. It decays as

$$^{111}\mathrm{Ag} \rightarrow ^{111}\mathrm{Cd} + e^- + \bar{\nu}_e(+\gamma) \tag{1.1}$$

Consequently, Ag-111 has the following properties:

- $\beta$- emitter with a medium half-life (about 7 days)
- the energy of the $\beta$-rays (360 keV mean value) is such that it offers a medium tissue penetration (1.8 mm)
- mid energy $\gamma$ emitter (342 keV) for imaging purposes

More details on the radiation properties of Ag-111 can be found in table 4.4. The emission of both electrons and gamma-rays allows to perform a dose distribution imaging while delivering the dose itself [12].

ISOLPHARM collaboration heads beyond the simple production of Ag-111 at LNL. Developing a drug that encapsulates Ag-111 is also a pillar of the project. Therefore, pre-clinical studies with mice will be essential to assess the capability of involved molecules in delivering the radionuclide to the target tumor. Typically, tumors in mice must have size less than 20 mm in order to limit rodent pain and distress [13]. There are several well-established techniques to perform diagnosis with such spatial resolution, we presented two of them that are routinely used in section 1.3.

Two emerging 2D-imaging techniques can be used for Ag-111:

**Cerenkov Luminescence Imaging (CLI)** It exploits optical photons emitted via Cerenkov effect

**Direct Radioisotopic Imaging (DRI)** It exploits optical photons emitted via scintillation

A device able to perform both techniques is the Bruker In-Vivo Xtreme II, that is described in Section 2.1 on page 17. Assessing if the spatial resolution achieved by this instrument will be sufficient to detect murine tumors is one of the aspects we want to investigate.

## 1.2 Aim of the thesis

The aim of this master thesis is twofold:

1. characterize the Bruker In-Vivo Xtreme II in both CLI and DRI modes;
2. provide quantitative predictions for the forthcoming images in the Ag-111 experiments.

A Monte-Carlo simulation is used to interpret the experimental images acquired with Bruker In-Vivo Xtreme II. The same simulation is used also to predict images with Ag-111 radionuclide.

We must stress that this is the first time this specific imaging system was used by the collaboration since its purchase. We aim to pave the way to future experiments that will be able to characterize with more precision all the features of the instrument. The various quantities that we estimate within this work are reasonable and can be used as an indication. On the other hand, we cannot provide a statistical uncertainty for these quantities.

Given these premises, we will enter the main part of this dissertation introducing some basic concepts of optics, radioactivity and particle physics. These concepts are of fundamental importance to understand how the Bruker In-Vivo Xtreme II works.

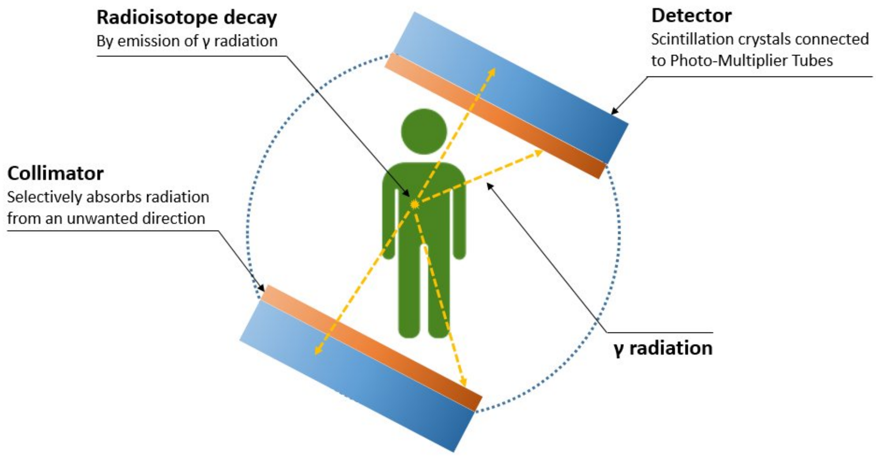


Figure 1.3: Single-Photon Emission Computed Tomography scheme. From [15]

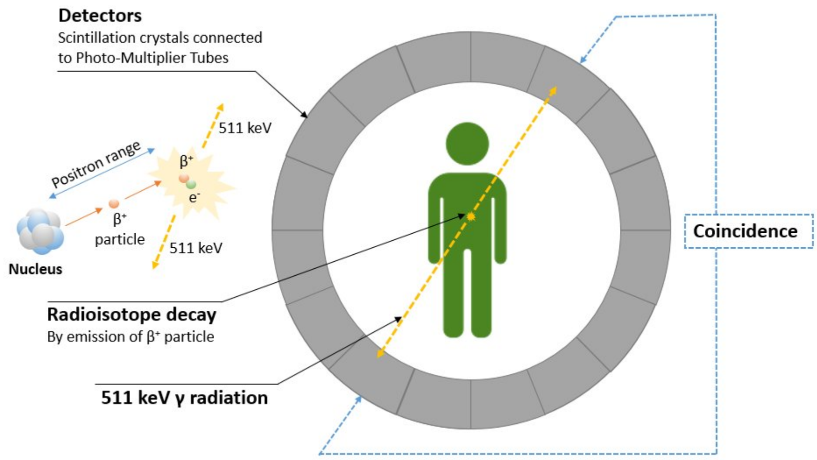


Figure 1.4: Positron Emission Tomography scheme. From [15]

## 1.3 Diagnostics in nuclear medicine

Developing drugs requires a lot of time and money and very few candidates make it to the market [14]. Applying non-invasive imaging techniques in the initial stages of the studies can help in selecting the best candidates whose on-target effects are confirmed.

Positron Emission Tomography (PET) and Single-Photon Emission Computed Tomography (SPECT) are two techniques that are used in this application. Like CLI and DRI they are based on the use of radioactive substances therefore it is worth mentioning their working principles for comparison.

SPECT is usually based on gamma camera detectors that can acquire 2D projection images around a sample or a patient. From this set of images a 3D distribution of the detected radionuclides radiation can be reconstructed [16]. Figure 1.3 shows the working principle of the SPECT.

Gamma cameras are normally provided with collimators, that play the role of mechanical lenses absorbing the gamma-rays coming from any direction different the selected one. The collimators are necessary to be able to reconstruct the spatial distribution of the activity.

Similarly, PET systems involve detection of gamma-rays generated after the decay of a radioactive nuclide. Collimators are not necessary since gamma-rays selection can rely on the fact that annihilation gamma-rays are emitted in opposite directions. Figure 1.4 shows the scheme of a PET system.

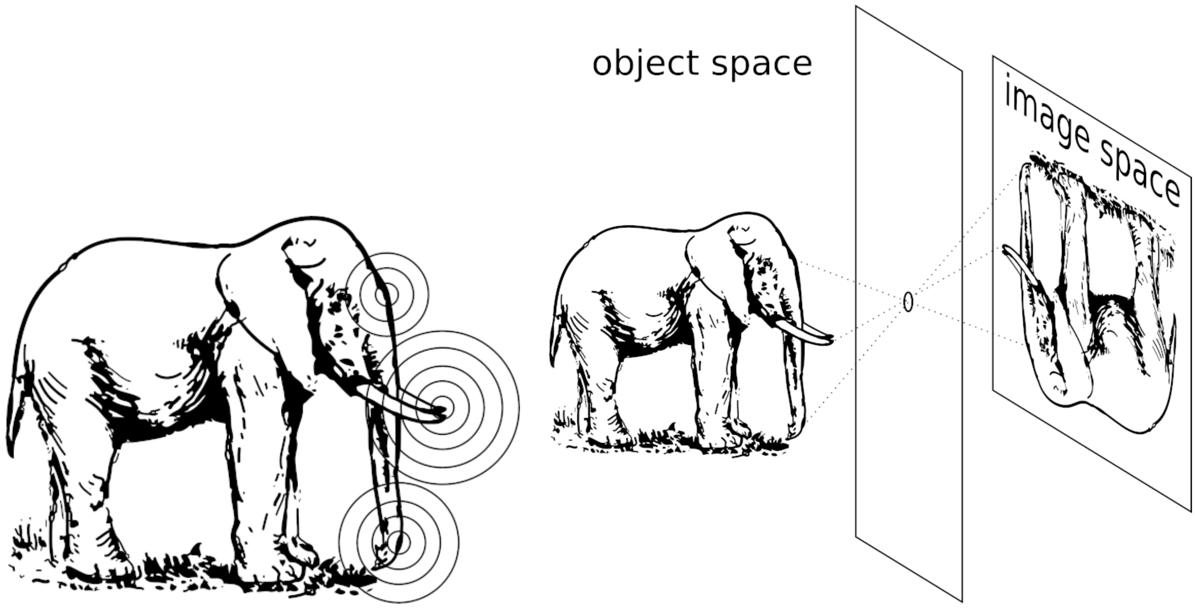


(a) Scheme representing an object, that is an elephant. From the points of the object divergent spherical electromagnetic waves are generated.

(b) Scheme representing a pinhole camera in the process of imaging an elephant. On the left there is the real object and on the right there is the real image.

Figure 1.5: Two schemes representing the concept of imaging. The elephant drawing is taken from [17].

## 1.4 Image formation

Depending on the application, diagnostics via optical rays can represent a valid alternative to PET/ SPECT systems. Detection of visible photons can be performed by small and cost-effective systems based on Charged-Coupled Devices (CCDs) contributing to the reduction of the drugs development costs. We will briefly introduce optical imaging.

Imaging means creating a unique map from a 3D region called *object space* to a 2D region called *image space* [18]. Figure 1.5 represents schematically the imaging process for an elephant. Each point of the object depicted in figure 1.5a (in this example the object is an elephant) can be thought of as a source of divergent spherical EM waves with different amplitudes [19], this construction is based on Huygens theorem [20].

An optical system that is able to intercept rays of these waves can be used to create the unique map between the object and the image spaces. Such a system can be a simple pinhole camera like the one depicted in figure 1.5b.

The disadvantage of pinhole cameras is that light collection is very inefficient consequently long acquisition times are needed in order to form an image. Lenses overcome this limitation because they are able to intercept a larger cone of rays. This greater efficiency in the light collection is usually accompanied by increased aberrations [21].

The Bruker In-Vivo Xtreme II can be considered an optical system because it uses various strategies to generate visible light from a sample and collects it through a lens scheme toward a CCD.

In the framework of medical imaging, there are five important parameters that characterize image quality [22]:

**contrast** It will be introduced in section 1.5 on the next page.

**spatial resolution** It will be introduce in section 1.6 on the following page.

**noise** Several sources of noise will be discussed subsection 2.1.3 on page 19.

**temporal resolution** In this thesis temporal resolution is not investigated.

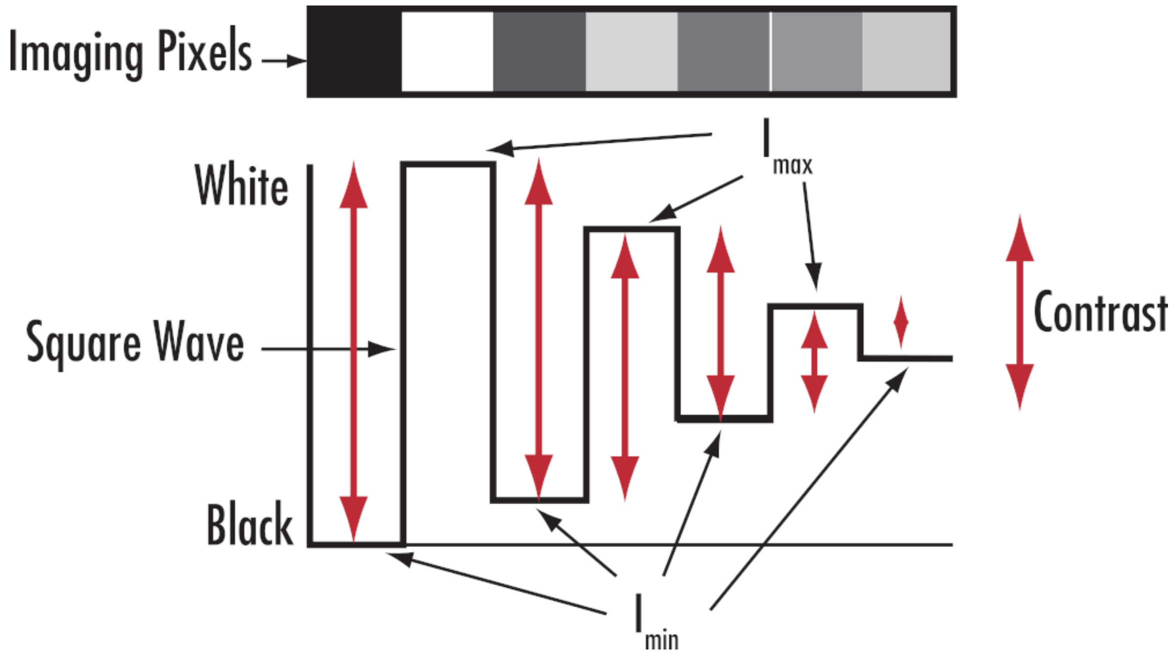


Figure 1.6: Sequence of dark and bright pixels alternated while decreasing the contrast from left to right. At high contrast black appears black and white appears white. At low contrast black and white turn into intermediate greys. From [23]

**radiation dose** Eventually, we aim to find a correlation between the intensity levels of the instrument and the activity of the sources. In future, dosimetric calculations with Monte-Carlo method can be provided using in input the activity information deduced by the acquired images.

## 1.5 Contrast

Contrast indicates how much an object stands out from the background [22]. In order to visualize this concept in a simple way, figure 1.6 shows a line of alternated dark and bright pixels with decreasing contrast from left to right. We can interpret the darker pixels as background and the brighter ones as object. In this situation, the contrast between two adjacent pixels is [23]:

$$C \equiv \frac{I_{\max} - I_{\min}}{I_{\max} + I_{\min}} \tag{1.2}$$

Typically, the contrast $C$ is a value between 0 and 1.

Low-contrast prevents the capability of detecting objects in an image. Different acquisition modalities involve different physical processes and thus the resulting contrast will differ [23].

## 1.6 Spatial resolution

The spatial resolution of an imaging system is its ability to reproduce object detail [24]. Assessing the spatial resolution of an image is not obvious since it depends also on contrast. A criterion that is usually adopted to assess the spatial resolution is the Rayleigh criterion.

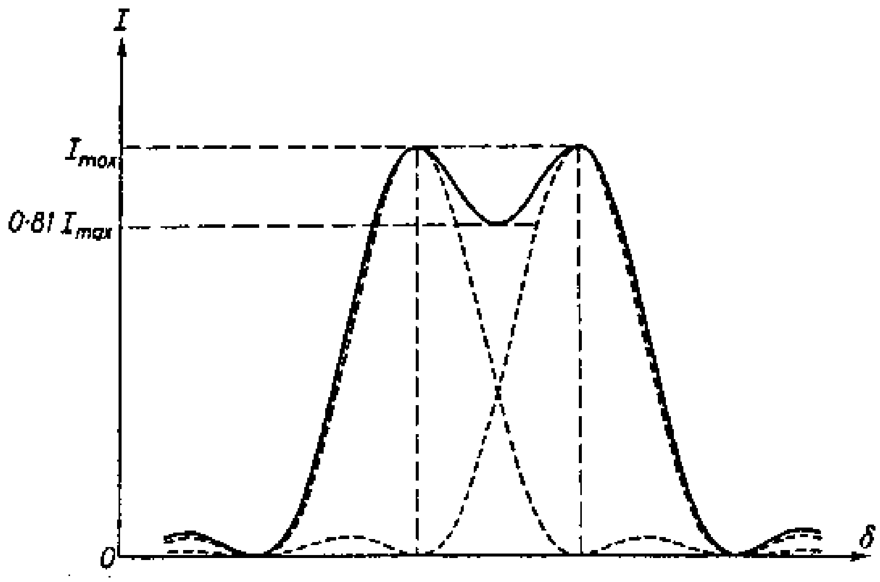


Figure 1.7: Intensity distribution of two light components just resolved according to the Rayleigh criterion, that is, when the principal maximum of one component coincides with the first minimum of the other one. The two components are monochromatic and have the same intensity. From [20].

Considering two sources of light, Rayleigh proposed that they are *just resolved* when the first intensity minimum of one coincides with the principal intensity maximum of the other, as depicted in figure 1.7. Summing the two distributions, the ratio of the intensity at the mid-point $I_{\mathrm{mid}}$ to that at the maximum $I_{\mathrm{max}}$ is [20]:

$$\frac{I_{\mathrm{mid}}}{I_{\mathrm{max}}} = \frac{8}{\pi^2} \simeq 0.81 \tag{1.3}$$

The Rayleigh criterion fixes a somewhat arbitrarily displacement of maxima at which the components may be said to be just resolved.

In order to apply Rayleigh criterion in a rigorous way, the two light components have to meet some requirements. They must be:

- point-like
- monochromatic
- of equal intensity

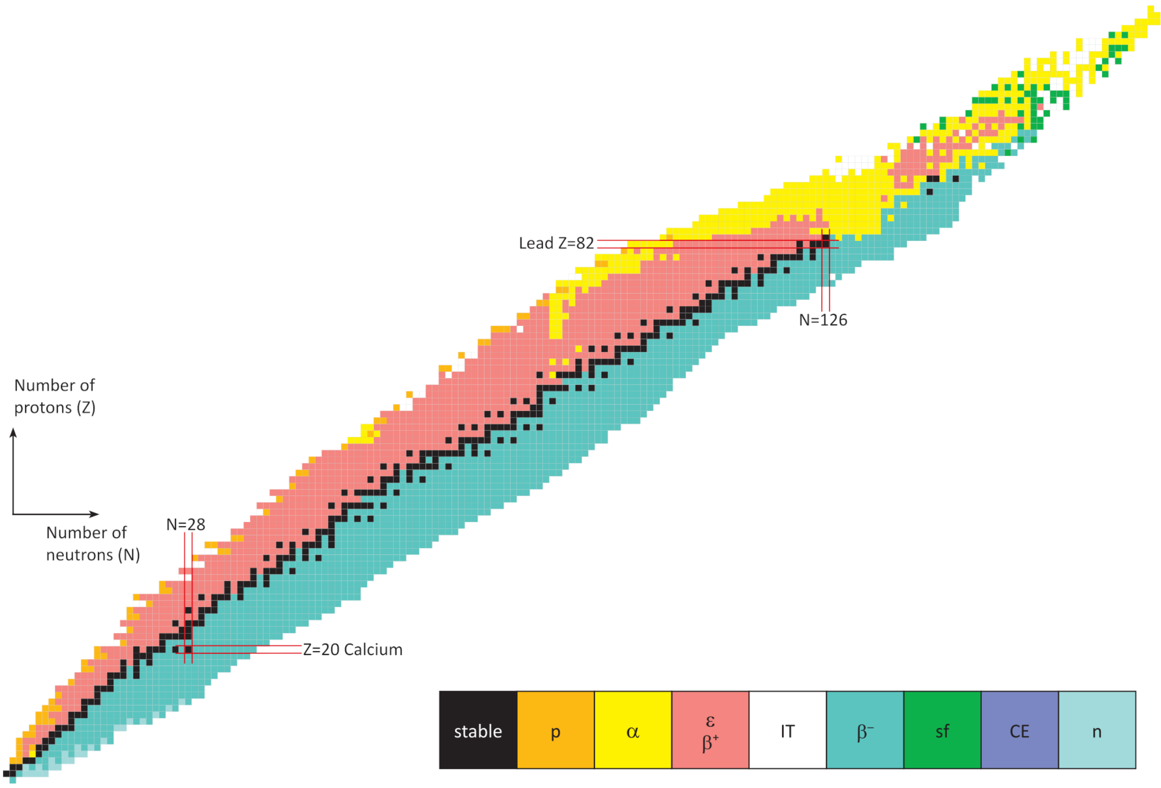


Figure 1.8: Isotopes table in which each square represents an isotope. The color indicates the mode of radioactive decay. From [27].

## 1.7 Radioactive decay

Radioactivity is the property of some nuclei to transform spontaneously into other nuclei. This transformation is called radioactive decay. During a decay energy is released in the form of kinetic energy and electromagnetic radiation [25]. Radioactive nuclei that can still be found today are either extremely long-lived or recently produced in accelerator facilities or nuclear reactors [26].

The isotope table (or Segré chart) collects all the isotopes, stable and unstable ones. Figure 1.8 represents this table: each square is an isotope and only the black ones corresponds to stable ones.

### 1.7.1 Exponential decay law

The number of radioactive nuclei $N(t)$ in a sample is ruled by the following differential equation:

$$-\frac{dN(t)}{dt} = \lambda N(t) \tag{1.4}$$

where $\lambda$ is the exponential decay constant.

Given a sample of $N(0) = N_0$ unstable nuclei at time $t = 0$, the number of nuclei that still have not decayed at time $t$ is

$$N(t) = N_0 \, e^{-\frac{t}{T_{1/e}}} \tag{1.5}$$

where $T_{1/e}$ (or $\tau = 1/\lambda$) is the mean lifetime of the nucleus. The formula can also be expressed in term of the half-life.

$$N(t) = N_0 \, 2^{-\frac{t}{T_{1/2}}} \qquad \text{where} \quad T_{1/2} = T_{1/e} \ln 2 \tag{1.6}$$

Considering a sample of radionuclides, half of it will have decayed after a time equal to the half-life of the isotope.

The activity of a radionuclide is defined as the number of decays $\Delta N$ that take place within a time interval $\Delta t$ normalized with the time interval itself [28].

$$A(t) = \frac{\Delta N}{\Delta t} = \frac{N(t) - N(t + \Delta t)}{\Delta t} \equiv -\frac{dN(t)}{dt} \tag{1.7}$$

Recalling the exponential law (equation 1.5)

$$A(t) = \frac{\overbrace{N_0}^{A_0}}{\tau} \exp\Big(-\frac{t}{\tau}\Big) \tag{1.8}$$

In the International System of Units (SI), the activity of a radionuclide is expressed in Becquerels [29], with

$$1\,\mathrm{Bq} = \frac{1\,\mathrm{decay}}{1\,\mathrm{second}} \tag{1.9}$$

The number of decaying events $\Delta N$ that take place in a finite time interval $[t_1, t_2]$ can be calculated as the difference between the number of nuclei that have still not decayed at the start $t_1$ and at the stop $t_2$.

$$\Delta N = N(t_1) - N(t_2) = N(0)\Big[\exp\Big(-\frac{t_1}{\tau}\Big) - \exp\Big(-\frac{t_2}{\tau}\Big)\Big] \tag{1.10}$$

$$\Delta N = A(0)\tau \exp\Big(-\frac{t_1}{\tau}\Big)\Big[1 - \exp\Big(-\frac{(t_1 - t_2)}{\tau}\Big)\Big] \tag{1.11}$$

Note that for time intervals small with respect to the lifetime of the radionuclide, we obtain again the definition of activity in equation 1.7.

$$\Delta N \xrightarrow{t_1 - t_2 \ll \tau} A(t_1)(t_2 - t_1) \tag{1.12}$$

Conversely, for time intervals great with respect to the lifetime of the radionuclide, we collect all the radionuclide available at the starting time $t_1$.

$$\Delta N \xrightarrow{t_1 - t_2 \gg \tau} N(t_1) \tag{1.13}$$

Unstable nuclei can decay in several way, in this work we are interested in:

- $\beta$ decay
- $\gamma$ decay

### 1.7.2 The decays of Ga-68, Tc-99m

$\beta$ decay is the process that tends to minimize the energy of the nucleus by optimizing the ratio $N/Z$ where $N$ and $Z$ are the number of neutrons and protons respectively [30]. The process is mediated by the weak interaction that changes one neutron in a proton ($\beta^-$) or viceversa ($\beta^+$). During the process a lepton-antilepton pair is created too or, in the case of electron capture, an atomic electron is turned into an electronic neutrino.

**$\beta^-$**

$$n \to p + e^- + \overline{\nu}_e \tag{1.14}$$

**$\beta^+$**

$$p \to n + e^+ + \nu_e \tag{1.15}$$

**electron capture**

$$p + e^- \to n + \nu_e \tag{1.16}$$

The energy spectrum of the emitted positron is continuous. When the positron slows down it annihilates with an electron of the medium producing two gamma rays of 511 keV energy [31].

$$e^+ + e^- \to \gamma + \gamma \tag{1.17}$$

Ga-68 decays $\beta^+$, the reaction is

$$^{68}\mathrm{Ga} \to {}^{68}\mathrm{Zn} + e^+ + \nu_e \tag{1.18}$$

The products are the daughter nucleus Zn-68 and two light particles of small mass with respect to the former product. Due to the kinematics of the process, the heavy (mass of the order of hundreds of GeV) daughter nucleus has low energy and is promptly stopped in the material. The neutrino can receive up to almost all the energy available but it interacts weakly and can be neglected within our setup. The positron can receive almost all the energy too, moreover it is interesting for imaging purposes because:

- its mean energy is enough to travel layers of material of the order of the millimeter to be detected in a charged particle detector;
- after its stop and annihilation with an electron of the medium, the annihilation gamma-rays can travel virtually any layer of material and be detected in a gamma-ray detector.

When considering a positron emitter, the number of positrons $N_2$ emitted in the energy range between $E$ and $E + dE$ is given by the following equation [32]:

$$N_2(E)dE = gF(Z,E)pE(E_{\max} - E)^2 dE \tag{1.19}$$

where $E_{\max}$ is the maximum positron energy, $p$ is the positron momentum, $g$ is a constant and $F(Z,E)$ is the Fermi function given by

$$F(Z,E) = -\frac{2\pi\alpha ZE}{p}\left(1 - \exp\frac{2\pi\alpha ZE}{p}\right) \tag{1.20}$$

where $\alpha$ is the fine structure constant

$$\alpha = \frac{e^2}{4\pi\epsilon_0\hbar c} \simeq \frac{1}{137} \tag{1.21}$$

and $Z$ is the charge of the daughter nucleus (or its atomic number). The Fermi function takes into account the Coulomb repulsion (or attraction in case of electron emission) between the positron and the daughter nucleus. We will use the number of positrons $N_2$ emitted (equation 1.19) to derive some formulas about Cerenkov effect in section 1.8.

Usually nuclei are found in their ground state, that is the state at lowest energy. Right after a $\beta$ decay or following a particle reaction, the nucleus can occupy an excited level with energy above the minimum one available. In this case, $\gamma$ decay takes place emitting the additional energy in the form of electromagnetic radiation (gamma-ray) and leaving the nucleus in a lower energy state. $\gamma$ decays continues to happen until the nucleus reaches the ground state.

Tc-99m is a metastable radionuclide because the half-life for its decay (see table 4.4 on page 40) is very long compared to typical half-lives of excited nuclei ($\sim 1$ fs). With an intensity of 98.6 %, the production of a gamma-ray of 140.5 keV energy is the most probable channel. In the other cases, the energy may be transferred to one of the atomic electrons, that usually belongs to the K, L, or M shell, in a process called internal conversion [33]. Then the excited electron escapes the attractive field of the nucleus releasing its energy in the surrounding medium.

Tc-99m is a radionuclide that decays $\gamma$. The reaction is

$$^{99\mathrm{m}}\mathrm{Tc} \to {}^{99}\mathrm{Tc} + \gamma \tag{1.22}$$

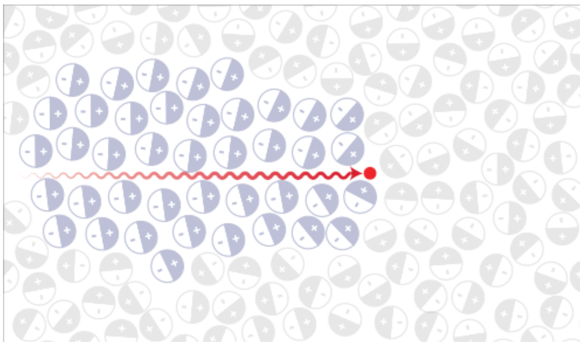

(a) A charged particle, represented as a red dot, travels in a medium from left to right. In the process it polarizes the medium.

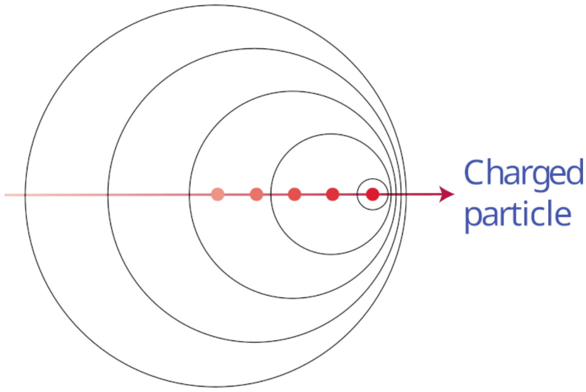


(b) A particle that travels with speed lower than the speed of light in the medium. The circles represent planar sections of light spherical wavelets emitted along the charged particle track (the red points).

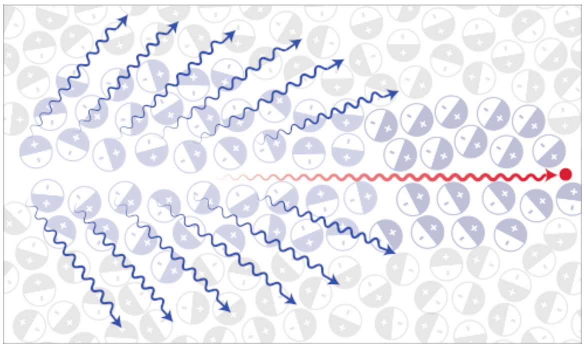

(c) The polarized medium returns to its ground state emitting visible light, represented as blue wavy lines, in a forward direction.

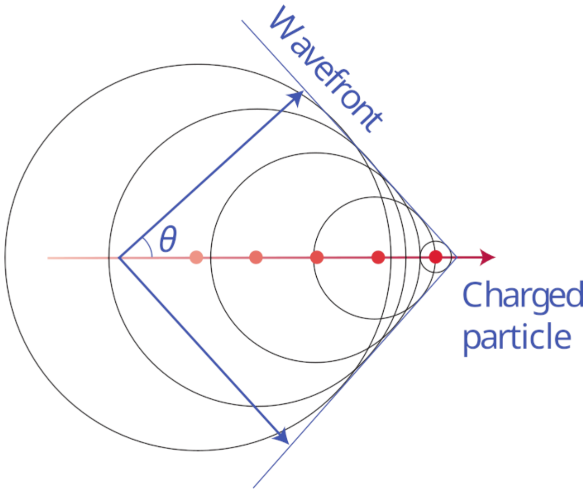


(d) If the particle is faster than light in the medium, constructive interference takes place between the spherical wavelets leading to a photonic wavefront (Cerenkov effect).

Figure 1.9: Cerenkov mechanism for a charged particle travelling in a dielectric medium is illustrated. From [35].

Tc-99 almost does not recoil, it is itself a radioactive nucleus and it decays $\beta^-$ as:

$$^{99}\mathrm{Tc} \rightarrow {}^{99}\mathrm{Ru} + e^- + \bar{\nu}_e \tag{1.23}$$

Even if a $\beta$ particle is produced in this decay, we shall not consider it because we expect to see a negligible amount of these decays during the experiment since the half-life for Tc-99 is $2 \times 10^5$ y [34] (compare this value to the half-lives in table 4.4). On the other hand, we will be able to see the gamma-rays from Tc-99m decay.

## 1.8 Cerenkov effect

A fast charged particle travelling at uniform velocity in a dielectric medium polarizes the surrounding medium along its track as represented in figure 1.9c. The electrons attached to the atoms of the medium will follow the waveform of the electromagnetic field as the particle passes [36].

When the particle is slow, after its passage the displaced electrons returns immediately to their normal positions. Then, due to destructive interference no radiation is observed. Instead, when the particle is fast, the wavelets from all the portion of the track are in phase with each other and a they constitute a wavefront inclined to the direction of the track. In this case a coherent radiation is observed. The discriminator for classifying a charged particle moving with velocity $v$ as slow or fast is the phase velocity of the light in the medium $c/n$:

**slow particle** $v < \frac{c}{n}$

**fast particle** $v > \frac{c}{n}$

The emission of this coherent light is called Cerenkov effect.

Note that this radiation is different from bremsstrahlung since Cerenkov radiation can take place even if the speed of the particle is uniform while the former requires an acceleration [37].

Between the angle $\theta$ at which the light emission takes place, the refractive index of the medium $n$ and the velocity of the particle normalized with the speed of light in vacuum $\beta = v/c$ there is a relation named after Cerenkov [36]:

$$\cos\theta = \frac{1}{\beta n} \tag{1.24}$$

Therefore, we see that Cerenkov effect can be interpreted as the electromagnetic analogue of the bow wave from a ship travelling in water with a speed exceeding that of the velocity of surface waves. From equation 1.24 one can deduce that:

- there is a threshold condition:

$$\cos\theta \leq 1 \qquad \Longrightarrow \qquad \beta \geq 1/n \tag{1.25}$$

  Particles with such small kinetic energy that their velocity is smaller than the phase velocity of light in the medium will emit no radiation.

- for every material there is a maximum angle $\theta_{\max}$ at which the light may be emitted. This angle is approximately reached when the particle travels with ultra relativistic velocities. In this ultra relativistic regime:

$$\cos\theta \xrightarrow{\beta\to 1} \frac{1}{n} \tag{1.26}$$

  Therefore

$$\theta_{\max} = \cos^{-1}\frac{1}{n} \tag{1.27}$$

Figure 1.9b represents the Cerenkov emission features. In figure 1.9b there is a 2D projection that shows the angle $\theta$ between the light direction and the particle direction, that is the vertical axis.

Frank–Tamm formula describes the number of optical photons produced per unit length as function of wavelength [38]. Its derivative gives the number of photons emitted per unit wavelength per unit length:

$$\frac{d^2N_1}{d\lambda dx} = -2\pi\alpha\frac{1}{\lambda^2}\left(1 - \frac{1}{\beta^2 n^2}\right) \tag{1.28}$$

The continuous spectrum of Cerenkov emission is cut off on the long wave side due to self-absorption of the radiation by the medium and on the short wave side because the refraction index becomes $n < 1$ and equation 1.24 cannot be satisfied [36]. Experiments that investigated the features of the Cerenkov effect found ranges of about $[430, 600]$ nm [39].

Assuming a refraction index constant within a wavelength range $[\lambda_{\min}, \lambda_{\max}]$, we can integrate equation 1.28 and obtain the number of emitted photons per unit length over the whole wavelength spectrum considered [40]:

$$\frac{dN_1}{dx} = 2\pi\alpha\left(\frac{1}{\lambda_{\min}} - \frac{1}{\lambda_{\max}}\right)\left(1 - \frac{1}{\beta^2 n^2}\right) \tag{1.29}$$

Microfluidic chips used to synthesize F-18 labeled compounds showed emission of visible light without nearby scintillators. The origin of such light was studied and its emission characteristics were found

| Isotope | Type | Mean energy (keV) | Intensity (%) | Range (mm) |
|---|---|---|---|---|
| Ga-68 | $\beta^+$ | 836 | 88 | 3.3 |
| | $\beta^+$ | 353 | 1 | 1.1 |
| Ag-111 | $\beta^-$ | 360 | 92 | 1.1 |
| | $\beta^-$ | 224 | 7 | 0.45 |
| | $\beta^-$ | 279 | 1 | 0.84 |

Table 1.1: CSDA Range of the charged particles emitted in the decay of Ga-68 and Ag-111. The range is extracted from the NIST Material database considering liquid water as medium.

to be consistent with Cerenkov radiation [41]. The charged primary particles with relativistic speed sufficient to produce Cerenkov radiation are the electrons and positrons emitted during beta decays.

Electrons and positrons are emitted with a characteristic energy spectrum, such as the ones represented in figure 3.1. When their energy is greater than the threshold for Cerenkov effect, the latter can take place. Since charged particles lose energy travelling in a medium, at some point their energy will drop below the threshold and they will eventually stop.

In the energy range we are interested in, from $(10 \text{ to } 10 \times 10^3)$ keV, the main contribution to energy loss of beta particles are ionization and atomic excitation, that are collision between beta particles and atomic electrons of the medium mediated by Coulomb interaction. Bethe-Bloch formula describes the collisional stopping power, that is the amount of energy loss per unit length $dE/dx$ due to collisions [42].

In this thesis, we are not interested in the details of Bethe-Bloch formula. Instead, we describe how to use it to determine the range of beta particles. First, we assume that Bethe-Bloch formula is able to describe the energy loss of the beta particles until they stop, this is the so called Continuous Slowing Down Approximation (CSDA) [42]. We write the range as a sum of small steps from the initial point $(x = 0)$ to the end point $(x = R)$.

$$R = \int_0^R dx \tag{1.30}$$

We rewrite the integrand using Bethe-Bloch formula. The limits of the integral change into the initial energy $(E = E_0)$ and the final one $(E = 04)$ accordingly.

$$R = \int_0^{E_0} \frac{dE}{-dE/dx} \tag{1.31}$$

Since we know $dE/dx$ (it is Bethe-Bloch formula) we can determine $R$. The range calculated in this way is called CSDA range.

Since Bethe-Bloch formula is valid only for electrons with energy approximately $> 50$ keV, one cannot calculate the entire range of the particle but only the high-energy part of it. The remaining small-energy part of the particle range has to be estimated using empirical curves [43].

In this section, we considered the medium to be liquid water. We reported in table 1.1 the CSDA ranges for the charged radiations with largest intensity. Since positrons and electrons have similar expressions for the stopping power, their ranges are similar [44][45]. We will consider also for the positrons the data are retrieved from the NIST Material database [46].

The finite range of beta particles emitted in radioactive decays implies that Cerenkov effect can happen in a region more extended than the volume in which the parent radionuclides are confined. Namely, Ga-68 and Ag-111 Cerenkov photons will originate from points that are far away from the parent radionuclide even for distances of the order of 1 mm. The former will have a larger spread of Cerenkov photons because the energy distribution of its positrons is at higher energies with respect to the energy distribution of the electrons of the latter.

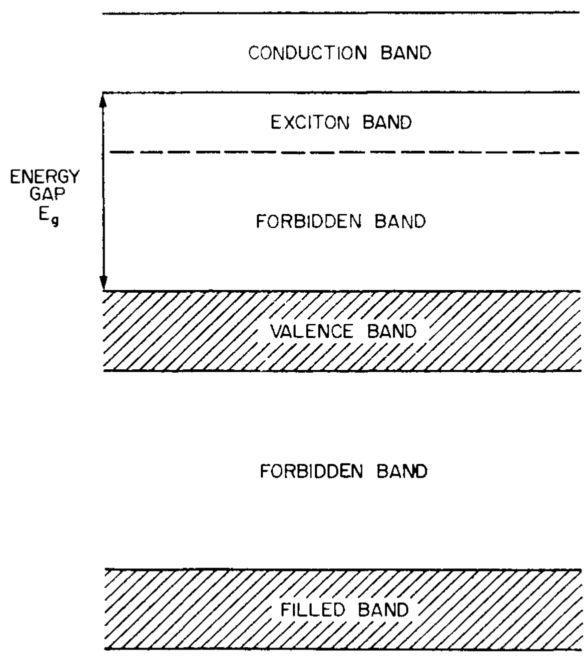


(a) Energy band scheme typical of ideal insulating crystals. From [47].

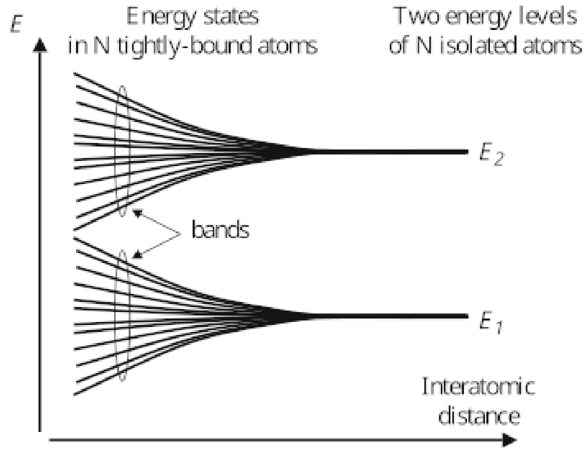


(b) Transition from energy levels of isolated atoms (right side) to energy bands of lattices (left side). At large interatomic distance the atoms do not interact and they all have discrete levels at the same energy. Decreasing the interatomic distance the atoms interact more strongly splitting the energy levels. From [49].

Figure 1.10: Formation of bands and their layout for an ideal insulating crystal.

## 1.9 Scintillation

We refer to the emission of visible (or ultraviolet) light with characteristic spectrum as luminescence [47].

The phosphor screens implemented by Xtreme are made of gadolinium oxysulfide that is an impurity-activated inorganic crystal. The luminescence of this type of materials is a crystalline property and, in particular, it is due to the presence of small concentrations of impurities. We will describe the luminescence phenomenon in phosphors, as inorganic luminescent materials are commonly called.

A suitable model for this description is the band theory of crystalline solids [48]. The energy states of the electrons in an isolated molecule consist of a series of discrete levels. In an inorganic crystal lattice the ions interact between themselves causing a perturbation of the outer electronic energy levels. Consequently, they form series of continuous allowed energy bands separated by forbidden energy bands. A scheme of this transition from energy levels to energy bands is shown in figure 1.10. Electrons can freely move in these bands that extend throughout the crystal.

An energy gap separates the highest filled band (called valence band) from the lowest empty band (called conduction band). This gap is usually of the order of few eV. Absorption of energy quanta can raise electrons from the valence band to the conduction band. In the process a positive vacancy (called hole) in the valence band is formed. The electron in the conduction band and the hole in the valence band can move independently or remain bound together. In the latter case, the system electron-hole is called exciton and is free to migrate throughout the lattice moving within a specific band, called exciton band, whose energy is below the conduction band [50]. In table 1.2 on the next page there are some analogies between single molecules and crystalline lattices that can help the clarification of these concepts.

The simple model described until now is valid only for perfect crystals. In practice, any real crystal contains defects and impurities that cause variations in the energy bands. Namely, centres of local

| Single molecule | Crystal |
|---|---|
| Excitation | Promotion of an electron into the exciton band |
| Ionization | Promotion of an electron into the conduction band |
| Formation of excited molecules following recombination of electrons and positive molecular ions | Formation of excitons following recombination of electrons in the conduction band and holes in the valence band |

Table 1.2: Comparison of some concepts regarding single molecules and inorganic crystals. The analogies are proposed in [47].

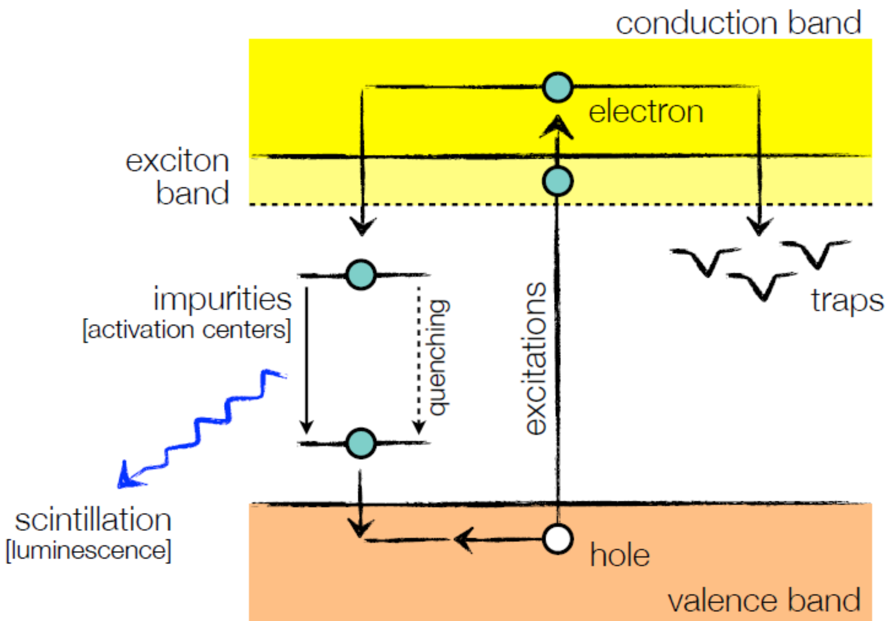


Figure 1.11: Energy bands (valence, forbidden, exciton and conduction bands in order of increasing energy) in impurity-activated crystal phosphor. Trapping, quenching, excitation and luminescence processes are showed. From [51].

electronic energy levels are produced in the forbidden region between the conduction band and the valence band. Electrons moving in the conduction band may enter these states. We can distinguish three types of centres:

**Luminescence centres** The transition from an excited state to the ground state is accompanied by the emission of a photon.

**Quenching centres** The transition from an excited state to the ground state happens via thermal dissipation and no photon is emitted.

**Traps** The excited states are metastable. From the trap states electrons can either jump back to the conduction band or fall to the valence band. In both cases the transition is radiationless.

This energy level system valid for impurity-activated crystal phosphors is shown in figure 1.11.

Luminescence centres arise from impurities in the lattice, such as interstitial atoms. The impurities introduce local discrete energy levels in the forbidden band. These levels correspond the ground and excited states of the centre. In order pass to an excited state, the luminescence centres must capture both an electron from the conduction band and a hole from the valence band. They can be captured by electron-hole recombination at the centre or through an exciton.

A theoretical model proposed by Seitz [52] can be used to discuss the conditions for quenching and

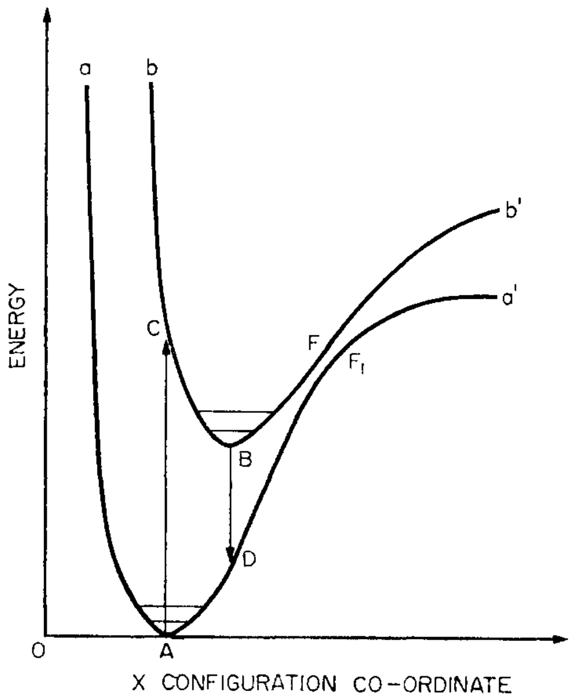


(a) Potential energy diagram of luminescence centre. $aAa'$, ground state. $bBb'$, excited state. AC, absorption transition. BD, luminescence emission transition. $FF_1$ region of internal quenching. From [47].

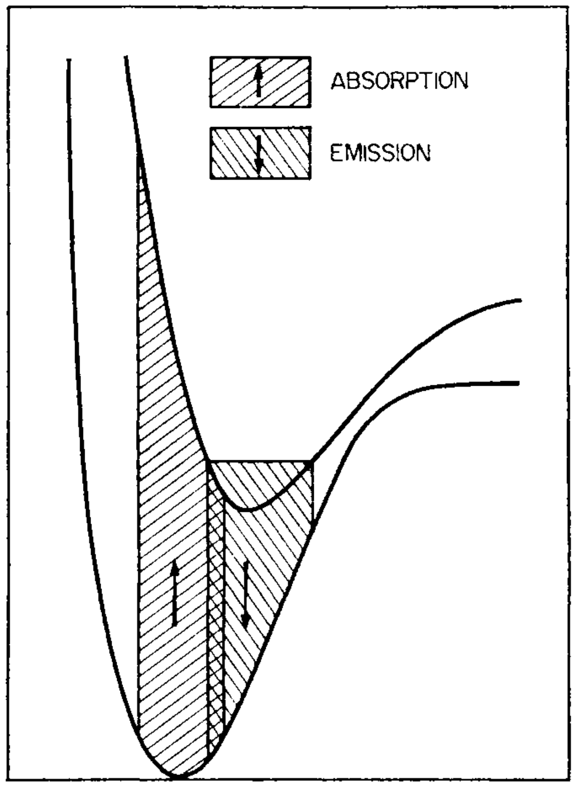


(b) Absorption and luminescence emission transitions. The overlap of the striped areas in the diagram corresponds to the overlap of the absorption and emission spectra. From [47].

Figure 1.12: Diagrams showing the features of the model for luminescence and quenching from [52].

luminescence emission of a centre. The ground state and excited electronic states of a luminescence centre have a potential energy that is function of a generic configurational coordinate of the centre. In figure 1.12a we show the energy versus configuration diagram of this potential energy. The curve $aAa'$ represents the vibrational amplitude of the centre in the ground state. Correspondingly, the curve $bBb'$ represents the vibrational amplitude of the centre in an excited state. In each curve there is a minimum point in which there is a stable energy position. At normal temperatures thermal vibrations determine displacements of the energy positions from the minima.

The features of the transitions between the ground state and the excited state within the framework of this model well reproduce the experimental observations [47].

# Chapter 2

# Bruker In-Vivo Xtreme II

## 2.1 Description of the instrument

### 2.1.1 About Bruker Corporation

The Bruker Corporation history starts in 1960 when professor Günther Laukien co-founded the company Bruker-Physik AG at Karlsruhe and became its first chairman. Laukien had studied Nuclear Magnetic Resonance (NMR) during his PhD thesis and his research career. The company started its activity developing an NMR pulse spectrometer [53].

The company was not named after professor Laukien because at that time there was a law in Germany that forbade active university professor from commercialize their research. Therefore, the co-founder doctor Emil Bruker borrowed his name for the start-up [54].

After a decade during which also clinical application were produced, the company chose to focus on pre-clinical systems. It acquired all the BioSpin companies that were specilized in NMR and it became Bruker BioSpin Group in 2001 [55]. Following a process of reorganization with other Bruker groups with different tasks, the companies unificated under the name of Bruker Corporation.

Today Bruker Corporation develops instruments for a wide range of applications: from life science research to agriculture and pharmaceutics. Correspondingly, a wide range of products is offered.

In case of imaging of small animals, Bruker Corporation offers Bruker In-Vivo Xtreme II (From here on we will refer to it as Xtreme for the sake of brevity). It is a multimodal system able to meet requirements for different situations. The system will be described in the course of this section.

### 2.1.2 System architecture

There are two models of Xtreme imaging system, both are sold with: a computer loaded with Molecular Imaging (MI) software, on-site installation, calibration, training and technical support. The two models differ in the camera (CCD) that is mounted on:

- Back-illuminated 4 MP camera
- Front-illuminated 16 MP camera

After installation, the camera can always be upgraded by a technician directly in the lab [56]. The model bought by Center for Advanced Pre-clinical *in vivo* Research (CAPiR) implements the back-illuminated 4 MP camera.

The Xtreme is able to perform different imaging techniques:

- BioLuminescence Imaging (BLI) [57] and CLI
- MultiSpectral Fluorescent Imaging (MSFI)

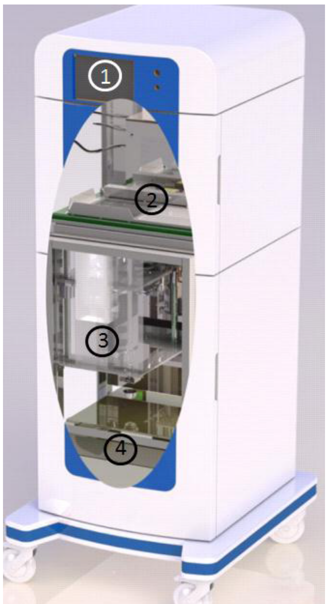


(a) Architecture of the Xtreme. (1) Microfocus X-ray source. (2) Imaging cabinet (sample room). (3) CCD detector. (4) Xenon illumination lamp. From [58].

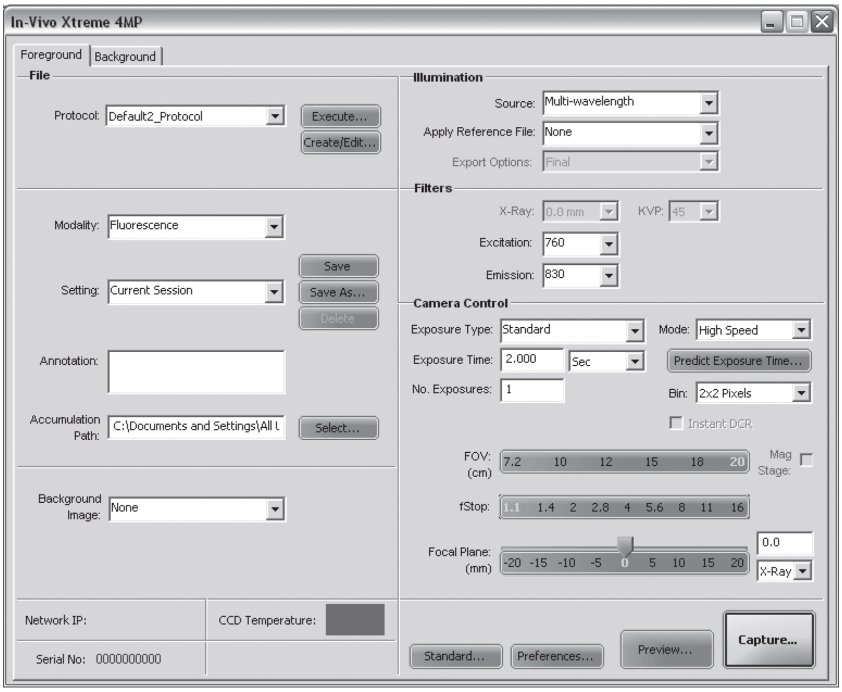


(b) Graphical interface of the MI software used to acquire the images. From [59].

Figure 2.1: A view of the Xtreme instrument and the graphical interface of the acquisition software are shown.

- Fluorescence Reflectance Imaging (FRI)
- X-ray imaging
- DRI

The key for achieving such a variety of techniques in only one instrument is exploiting optical photons. The system combines a highly sensitive CCD detector with xenon illuminator, patented phosphor screen technology, patented wide-angle emission filters and microfocus X-ray source. Thanks to this configuration the Xtreme is highly flexible and sensitive. Furthermore, there are also animal support options that allows to go from a 2D imaging mode to a 360° detection mode [58].

Differently by other systems, such as the Xenogen IVIS Spectrum, the Xtreme has a inverted detection platform with the sample placed above the CCD (figure 2.1a). This configuration provides low cross-sample shadowing, consistent flat focal plane and reduction in the length of the light path from sample to detector. The CCD used in the model acquired by the CAPiR lab has the following features:

- back-thinned/back-illuminated
- 16-bit pixel depth
- $-90\,^{\circ}$C cooled
- grade 1
- equipped with Hush technology[1]

These characteristics determines a minimal detectable radiance that is less than 60 photons/s/sr/cm$^2$.

[1] Hush technology reduces the read-noise even in high bin states

| Binning option | Number of super-pixels |
|---|---|
| 1x1 | 2048x2048 |
| 2x2 | 1024x1024 |
| 4x4 | 512x512 |
| 8x8 | 256x256 |
| 16x16 | 128x128 |
| 32x32 | 64x64 |

Table 2.1: Binning options available for CCD reading of Bruker In-Vivo Xtreme II.

The Xtreme detector, including CCD, lens, diopters and emission filters, is mounted on an elevator platform with six preset positions that have different Field of View (FoV): 7.2, 10, 12, 15, 18, 19 $\mathrm{cm}^2$. Small FOV positions allows imaging at high zoom for high resolution imaging while high FoV positions allows multi-animal imaging. Different modalities can require different FoV but this is not an issue since the detector is on the elevator stage while the sample is on a fixed support: the system can change between the preset positions without upsetting the sample animals' positions. Multimodal image registration is natural for Xtreme system.

### 2.1.3 The CCD camera

In some scientific imaging applications there may be need for very high level of sensor performance in order to achieve useful Signal-to-Noise Ratio (SNR). Indeed, this is the case for BLI, CLI, DRI and fluorescence imaging because the flux of photons that cross the CCD is very low. Many factors contribute to the noise and deteriorating the SNR of the CCD [60]. These factors that limit the sensitivity of the detector are discussed in this section in the context of the Xtreme detector.

- Shot noise is a consequence of the statistical nature of the arrival rate of photons incident on the CCD [61]. The signal of the CCD is made of the photoelectrons generated within the semiconductor device. Due to the statistical nature of the arrival rate of photons, the signal is described by a Poisson distribution. A discrete random variable $X$ follows a Poisson distribution if its Probability Density Function (PDF) has the form [62]:

$$P_X(x) = \begin{cases} \frac{\alpha^x e^{-\alpha}}{x!} & x = 0, 1, 2, ... \\ 0 & \text{otherwise} \end{cases} \tag{2.1}$$

  In this case, the variable $X$ has

$$\text{expected value} \quad E[X] = \lambda \qquad \text{and} \qquad \text{variance} \quad \sigma^2[x] = \lambda \tag{2.2}$$

  Therefore, the variance on the signal due to the shot noise is equal to the magnitude of the signal itself. Shot noise cannot be reduced improving the design of the camera [63]. In section 5.6 we will discuss how shot noise affect the images that we acquired in the experiment.

- Dark noise is due to thermal excitation of electrons. This noise is generated even without any light source because it arises directly in the CCD. After the electrons are collected within the wells of the CCD, they are read as signal independent from their source [64]. Since the generation of thermally excited electrons depends strongly on the temperature, one way to suppress the dark current is by cooling down the CCD to low temperatures. Similarly to shot noise, dark noise follows a Poisson distribution with variance equal to the average number of thermal electrons generated within the exposure time [63]. The camera of the Xtreme is cooled to $-90\,^{\circ}\mathrm{C}$.

- Read noise is a combination of noise components that are related to the conversion of charge carriers into a voltage signal and to the Analog-to-Digital (A/D) conversion. The largest part originates with the on-chip preamplifier. This contribution is uniform to every image pixel. Certain types of noise in the CCD output amplifier depends on the frequency of the read-out.

(a) Photo representing the radioisotopic screen and the sample support. From [65].

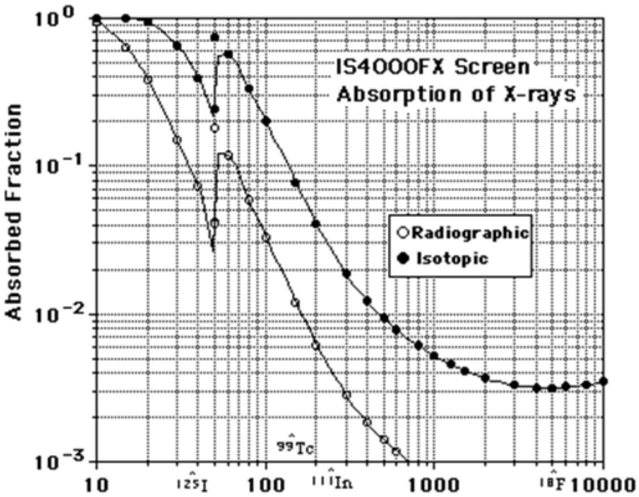


(b) Attenuation coefficient of the radiographic screen and of the radioisotopic screen. From [65].

Figure 2.2: A photo of the radioisotopic screen is shown together with the absorption fraction as function of energy.

According to the read-out rate required for the specific application, that is equal to the frame rate, the read noise specification will change and so the overall SNR [63]. The Hush technology born in reply to the efforts made to reduce the read noise during the development of the Xtreme II camera.

- Binning is not a noise contributor but can be used to adjust the sensitivity of the CCD. Binning is achieved by combining charge from adjacent pixels to form a *super-pixel.* The read noise grows at each step, or bin, that the charge needs to travel to reach the readout amplifier. Reducing the number of steps with the binning procedure causes a reduction of the read-out noise. This binning procedure reduces also the spatial resolution limit set by the pixel size. However, since light scatter in tissues is the overriding factor in determining the optical imaging resolution, the increase in the pixel size may be negligible with respect to the light scatter limit. Adjusting the binning to the right value can be a useful tool to increase the sensitivity for a particular sample without losing too much resolution. The higher the binning selected the more SNR the user can obtain. The binning options are resumed in table 2.1. In the 32x32 binning option the detection limit is as low as 41 p/s/cm2/sr.

### 2.1.4 Illuminator and Filters

The Xtreme has a 400 W Xenon illuminator. This lamp provides high intensity optical beams with wavelength spectrum in (350 to 1000) nm. There is also a wheel that allows to choose between 28 excitation filters. These filters are of the bandpass type and can select a wavelength range between (410 to 760) nm with band width of 10 nm.

Another wheel allows to select also the emission filters. There are 7 bandpass filters between (535 to 830) nm with a bandwidth between (17.5 to 20.0) nm. There is also an empty slot to collect directly all the light emitted from the sample. The system employs patented wide-angle emission filters that have a blocking efficiency uniform from the center to the edge of the filter. These patented filters contribute to the high SNR and the overall image uniformity.

### 2.1.5 Radiographic Screen and X-ray Source

The system is equipped with two different phosphor screens, a photo is shown in figure 2.2a. They can be inserted between the sample and the CCD to convert high energy gamma-rays into optical photons that can be detected by the CCD. Since the phosphor screen is located above the sample, no limit in the animal size is set (apart for the size of the sample chamber itself). The two screens differ in their absorption efficiency: the radiographic screen is optimized for the detection of X-Rays while the radioisotopic screen is optimized for the detection of gamma-rays that have usually larger energy than X-Rays. Figure 2.2b on the facing page shows a graph where the absorption efficiency is plot as function of energy for both phosphor screens.

The micro focus X-Ray head provides a cone of X-Rays with a vertex with spot size $< 60\,\mu m$. The X-Rays are generated with a current of $500\,\mu A$ and a tension between 20 and 45 kVp. An X-Ray image can be produced in less than 1 s, therefore, this modality can be used to shoot background images that represent the structure of the sample.

### 2.1.6 Radioisotopic Screen

As already mentioned, the radioisotopic phosphor screen is used to convert typical PET and SPECT radionuclides gamma-rays into optical photons. The modality that used this screen, DRI, allows to image radionuclides commonly used in nuclear medicine, such as Tc-99m, that are not detectable using CLI. DRI is also useful for deep tissue penetration imaging since in tissues, gamma-rays scattering is less important than optical photons scattering. The CLI/DRI combination provides flexible radionuclide tracer 2D imaging with good temporal resolution. This imaging system integrates dedicated PET/SPECT platforms due to its multi-animal throughput, relative short exposure times (with respect to 3D imaging) and high sensitivity, e.g. down to $0.05\,\mu Ci$ of Tc-99m [66]. Large animal cohorts with varying therapeutic combinations can be screened with DRI for research importance reducing time and cost necessary using PET/SPECT. Moreover, DRI allows preclinical researchers to use small radionuclide reporters to tag the compound in exam thus minimizing the disruption of the normal biodistribution. This consideration is useful for researchers working with small compounds or developing PET and SPECT tracers [67].

### 2.1.7 Animal Chambers and Beds

The Xtreme can be upgraded with a range of animal chambers. These solutions provide for optimum animal care and user safety. There are also supports that can transform then instrument into a 3D imaging system. An advanced anesthesia system is available for multi-animal imaging.

### 2.1.8 Rotation Imaging

The optional Multimodal Animal Rotation System (MARS) facilitates automatic rotation of the animal for muli-projection imaging. This optional can be used to find the angle at which the light travels the shortest distance in tissue thus maximizing the sensitivity.

### 2.1.9 Software

The Xtreme bundle comprehends a software package named Bruker Molecular Imaging (BMI). The software controls the settings of the acquisition and manages the data files organization. There is a graphical interface that allows an intuitive and fast data analysis [68]. The tools available to improve the contrast and analyze Region Of Interest (ROI) and multiple images are enough complete to provide publication quality pictures. The capture menu can easily switch between the settings of the background and the foreground acquisitions. More complex acquisitions can be easily programmed. The images can also be analyzed in batch mode. The processed images can be exported in many file formats, Digital Imaging and COmmunications in Medicine (DICOM) too. All the acquisition modalities of the Xtreme are driven via the BMI software. Figure 2.1b on page 18 shows the graphical interface of the software during an acquisition.

### 2.1.10 Optional/Custom Items

Bruker offers the possibility to work together with the researcher to build customized items required for special applications. For instance, DRI lead collimators may be realized to improve DRI resolution.

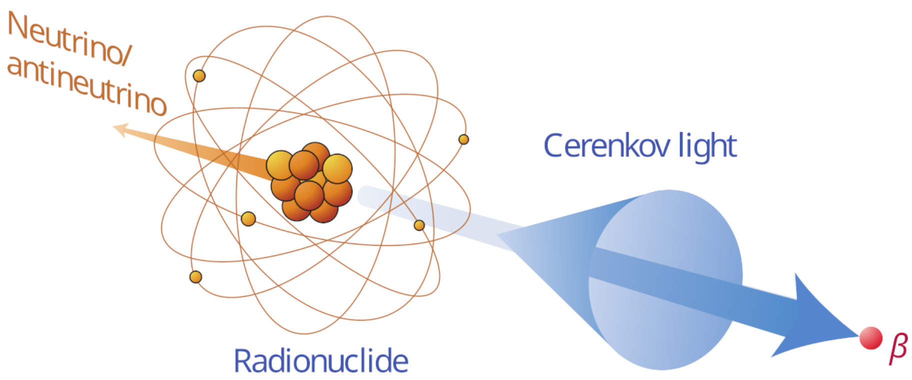


Figure 2.3: Cerenkov light is emitted (blue cone) by the medium in which a charged particle (blue arrow) travels. Radionuclides that emit $\beta$-particles with energies greater than the Cerenkov threshold (261 keV in water) result in Cerenkov Luminescence. From [35].

## 2.2 Cerenkov Luminescence Imaging

Already in 1968, Cerenkov effect (described in section 1.8) was exploited to measure the activity of radioisotopes (sometime this type of measurement is called *radioassay*) [69].

Cerenkov counting is a quite simple method for performing radioassay of $\beta$-emitting radionuclides samples. The production of visible photons takes place as depicted in figure 2.3. With respect to liquid scintillation counting, the sample preparation is easier since only an aqueous solution is necessary. For the same reason, large volumes of sample can be measured and the sample can be completely recovered after the measurement.

On the contrary the idea of using this phenomenon to produce images is pretty recent [41]. In 2009 Cho et al. observed visible light emitted from microfluidic chips used to synthesize F-18 labeled compounds. The origin of the light was investigate and since there was no scintillator or fluorescent material in the surroundings, they conclude that the emission characteristics of the light were consistent with Cerenkov radiation.

They shot a photograph of the F-18 solution and the color of the light emitted resulted bluish-white, confirming the Cerenkov radiation nature of the emission. In the same article they investigated the feasibility of measuring quantitatively the radioactivity within the microfluidic chip using the Cerenkov light emission. For this experiment, they used a detector made of a CCD coupled to a lens that was previuosly developed for imaging microfluidic platforms.

Thanks to this article, many other studies investigated the feasibility of Cerenkov based imaging. Since the visible light is produced by the sample itself without the need of external light sources, it can be classified as *Luminescence*. Instruments able to perform luminescence imaging were already a standard in laboratories where in-vivo studies were carried out. Therefore, it was only natural that these instruments would become standard also for Cerenkov Luminescence Imaging (CLI) studies.

The first article introducing CLI as meant in this thesis uses Xenogen devices (IVIS 100 or 200, Caliper Life Sciences, Alameda, CA) [70].

These devices are similar to the Bruker In-Vivo Xtreme II. Indeed, the CCD technical specs are identical [71].

The bio-distribution of a plethora of radiopharmaceuticals for therapy, imaging and both can be imaged by using CLI without the need of more expensive SPECT and PET tomographic systems. The cost-effectiveness and simplicity of the CLI technique will determine a spread of its employment in small laboratories [38].

Figure 2.4a shows a scheme that represents CLI.

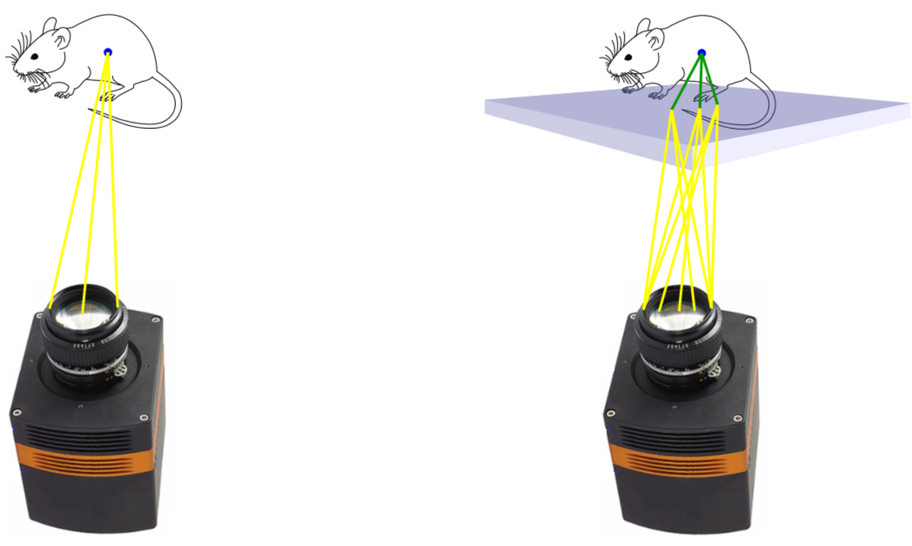

(a) CLI diagram. The optical photons are generated within the mouse and collected by the camera.

(b) DRI diagram. Ionizing radiation generated within the mouse produce optical photons in the scintillator screen and these ones are collected by the camera.

Figure 2.4: Two imaging modalities of the Bruker In-Vivo Xtreme II. The mouse drawing is from [72] and the camera photo is from [65].

## 2.3 Direct Radioisotopic Imaging

Scintillation phenomenon described in section 1.9 is frequently used in the detection of non-charged radiation. For instance, the majority of X-Ray imaging detectors use two stages [73]:

1. the X-Rays are absorbed by a phosphor and converted into visible light;
2. the visible light is then collected by an optical sensor (e.g. a CCD).

The spread of the scintillation light produced in a phosphor is proportional to the path length required to escape the phosphor itself. Therefore, the thicker the phosphor the wider the spread of the light will be.

Indeed, phosphor are usually used as thin (less than 1 mm) screens [74]. They are made combining 5–10 µm diameter phosphor particles with transparent plastic binders. The patent owned by Bruker Corporation that describes the basic concepts of DRI acquisition mode also shows the scheme for a phosphor screen. I reported this scheme in figure 2.5a.

Bruker In-Vivo Xtreme II exploits scintillation as a mechanism to produce optical photons that are collected in the CCD.

Typically, the energy of X-Rays is lower than that of gamma-rays. For this reason the instrument is equipped with two different phosphor screen:

- Radiographic phosphor screen, optimized for detection of X-Ray photons
- Radioisotopic phosphor screen, optimized for the detection of gamma-ray photons

The concept of this imaging technique can be found in a patent currently assigned to the Bruker Biospin Corporation [75].

This patent describes an assembly for an imaging system. The assemblage includes:

- a phosphor layer for prompt conversion of the ionizing radiation into light;
- an electronic camera for conversion of the light image into an electronic image.

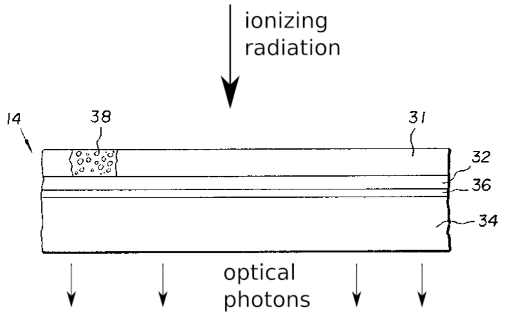


(a) Section of the phosphor screen used in the patent owned by Bruker Corporation. The numbers indicate: (14) imaging assemblage; (31) phosphor layer; (32) transparent support layer; (34) support layer; (36) air boundary layer; (38) phosphor grains. From [75].

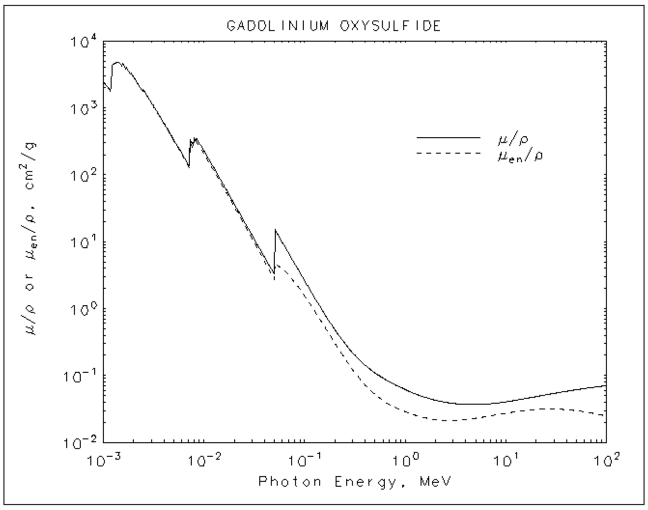


(b) Attenuation coefficient as function of energy for Gadolinium Oxysulfide. From [76].

Figure 2.5: Scheme of a Gadolinium Oxysulfide based phosphor screen and attenuation coefficient for the material itself.

The scintillator is a material such as Gadolinium Oxysulfide. Therefore, the sensitivity of the screen to the energy of the gamma-ray will be proportional to the attenuation coefficient at the same energy. Figure 2.5b shows the attenuation coefficient of Gadolinium Oxysulfide as function of the energy of the impinging gamma-ray.

A scheme that represents this system is shown in figure 2.4b. Note that the ionizing radiation may be constituted also of electrons and positrons. This possibility is considered also in the user manual of the instrument [77].

# Chapter 3

# Simulation

## 3.1 Geant4 toolkit description

In order to interpret the experimental images, we are going to simulate the acquisition performed in the experiment using Geant4 software.

Geant4 is a toolkit designed to simulate particles passing through matter. This toolkit is applied in many fields, including: nuclear and high energy physics, medical science and cosmonautics [78].

Geant4 has its origin in GEANT3, a software that was realized in order to help physicists in designing detectors and in analyzing the experimental data [79]. In turn, GEANT3 first version is Generation of Events ANd Tracks (GEANT) program [80].

The toolkit allows to consider a wide range of physics processes including hadronic, electromagnetic and optical processes. Long-lived particles as well as short-lived can be generated over a wide range of energies. They can pass through a number of pre-defined materials or user-defined ones [81].

The passage of particles is represented by tracks. The track of a particle describes the trajectory it followed from the the instant in which it was generated to the instant in which it was killed. In our application, particles are killed when their energy falls below a certain cutoff energy.

The amount of information that the Geant4 records can be decide by the user according to the application. In our case, the beta particles tracks were considered because optical photons generation due to Cerenkov effect and scintillation happens step by step during the passage of the particle in media. Instead, we did not track the optical photons inside the medium. Rather, initially we tried to track the photons from the source to the CCD in order to form a real image at the level at the CCD but, even if we obtained an image using a lens model template, we soon realized that we lacked fundamental knowledge about:

- the model for the lenses used in the real instrument;
- how to remove aberrations (that were strongly affecting the template image);
- the light path of the photons in the lower part of the instrument since that part can only be accessed by a Bruker technician.

Therefore, we conclude that it would have been simpler to resume the effect of the optical rays travel in a Gaussian blurring filter, the same that we introduced in subsection 5.2. So, the simulation of the experimental images can be divided in two parts:

1. simulate the optical photons generation (the optical photon object, as we defined it in subsection 5.2) in Geant4 and store the coordinates of the points in a matrix, that we may call object matrix;
    - for CLI the object matrix is the ensemble of points where Cerenkov effect takes place

- for DRI the object matrix is the ensemble of points where Scintillation takes place

2. apply a Gaussian blur filter to the object matrix and obtain the image matrix.

The simulation does not consider the trajectory followed by the optical photons after their generation, thus, the effect of the distance between source and sample support cannot be studied for CLI with Geant4. Instead, for DRI the effect can be analyzed since the distance between the source and the scintillator screen has an impact in the generation of the optical photons. This fact nicely agrees with the experimental evidence the CLI spatial resolution does not depend from the distance while DRI strongly does. We investigated this phenomenon in section 5.3.4.

## 3.2 Geant4 Simulation of Radioactive Decay

Simulating radioactive decays consists of the task of destroying an unstable nucleus (parent) and generating another nucleus (daughter) together with the other products [82].

The daughter nucleus should be produced with specific physical properties because mass number and atomic number are determined by the decay type. Instead, kinetics and excitation energy are determined by both parent kinetics and products kinetics. Other than generating the direct products of the decay, the software should also handle the process of de-excitation of the daughter nucleus, producing the necessary gamma-rays, X-rays and Auger electrons.

In practice, theoretical calculations of the parameters involved in the decay are not feasible in the course of the simulation. Many software manages these parameters relying on empirical pre-calculated data.

Geant4 calculates branching ratios on the basis of the data from the Evaluated Nuclear Structure DataFile (ENSDF) [83]. This database contains information on half-lives, decay types with their branching rations, emission energies and electromagnetic transition types. It is maintained by the National Nuclear Data Center (NNDC) and it is distributed also by the International Atomic Energy Agency (IAEA). The same database is used by Geant4 in photo-evaporation routines to correctly sample discrete gamma-ray transitions [84][82].

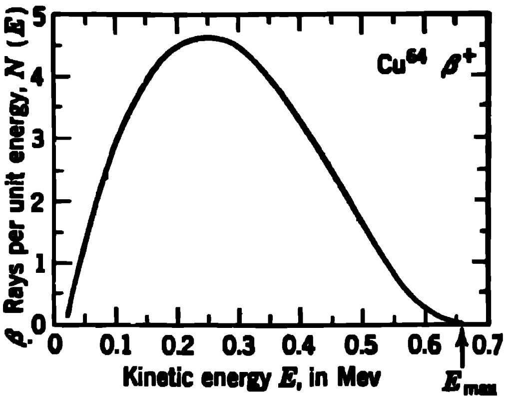


(a) Positron spectrum from [85].

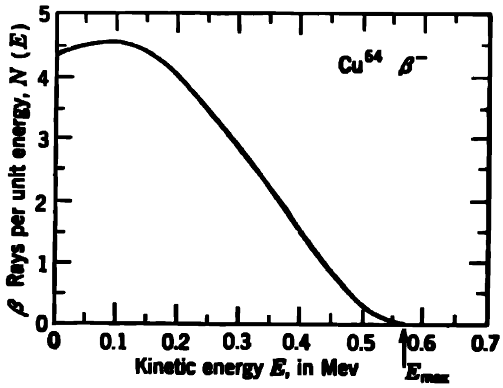


(b) Electron spectrum from [85].

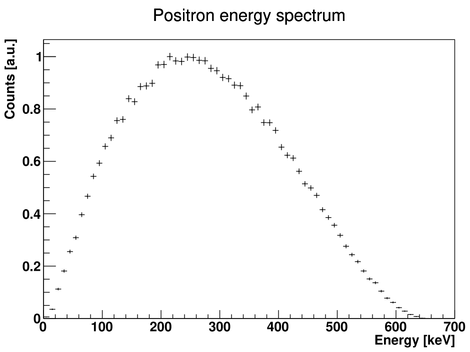


(c) Positron spectrum from the simulation.

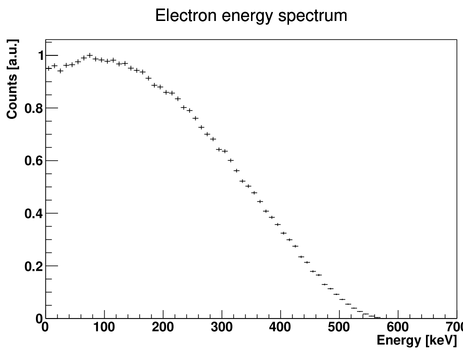


(d) Electron spectrum from the simulation.

Figure 3.1: Energy spectra of $\beta$ particles emitted in Cu-64 decay.

I test Geant4 $\beta$-decay by comparing the energy spectra of the positrons and the electrons emitted by Cu-64 radionuclides with the spectra available in literature [85]. Figure 3.1 shows the comparison:

- end-points are well reproduced as well as the overall trends
- the differences between electrons and positrons in the low energy part of the spectrum due to Coulomb interaction with the daughter nucleus are well reproduced

## 3.3 Geant4 Simulation of Cerenkov Effect

Cerenkov effect in Geant4 is treated in a specific class called G4Cerenkov. The class implements an algorithm that works with the following steps:

1. check that the primary particle is suitable to generate Cerenkov photons:
    - it must have an electric charge
    - it must have speed greater than the speed of light in the medium
2. calculate the average number of Cerenkov photons emitted per unit length
3. calculate the step length
4. calculate the average number of Cerenkov photons emitted in the step
5. the average value calculated in the previous point defines a corresponding Poisson distribution
6. the number of Cerenkov photons produced in the step is extracted from this Poisson distribution

We consider the derivative of Frank-Tamm formula in equation 1.28. The relation between the wavelength $\lambda$ of a photon and its energy $E$ is

$$E = h\nu = \frac{2\pi\hbar c}{\lambda} \tag{3.1}$$

$$dE = -\frac{2\pi\hbar c}{\lambda^2}d\lambda \tag{3.2}$$

We substitute the energy expression in equation 1.28.

$$\frac{d^2N_1}{dEdx} = \frac{\alpha}{\hbar c}\left(1 - \frac{1}{\beta^2 n^2}\right) \tag{3.3}$$

Then we integrate in the energy range $[E_{\text{min}}, E_{\text{max}}]$ in which the refraction index of the material is known.

$$\frac{dN}{dx} = \int_{E_{\text{min}}}^{E_{\text{max}}} \frac{\alpha}{\hbar c}\left(1 - \frac{1}{\beta^2 n^2}\right)dE \tag{3.4}$$

The integral can be broken in two parts.

$$\begin{aligned} \frac{\alpha}{\hbar c}\int_{E_{\text{min}}}^{E_{\text{max}}}\left(1 - \frac{1}{\beta^2 n^2}\right)dE &= \frac{\alpha}{\hbar c}\left(\int_{E_{\text{min}}}^{E_{\text{max}}} dE - \int_{E_{\text{min}}}^{E_{\text{max}}} \frac{1}{\beta^2 n^2}dE\right) \\ &= \frac{\alpha}{\hbar c}\left(E_{\text{max}} - E_{\text{min}} - \frac{1}{\beta^2}\underbrace{\int_{E_{\text{min}}}^{E_{\text{max}}}\frac{1}{n^2}dE}_{I_0}\right) \end{aligned} \tag{3.5}$$

where the refraction index of the material is a function of the energy of the photon $n(E)$.

The integral $I_0$ is numerically calculated in Geant4 algorithm via trapezoidal method:

$$\begin{aligned} I_0 &= \sum_{i=0}^{N_i}\left(\frac{1}{n^2}dE\right)_i \\ I_0 &= \sum_{i=1}^{N_i}\frac{1}{2}\left(\frac{1}{n^2(E_i)} + \frac{1}{n^2(E_{i-1})}\right)(E_i - E_{i-1}) \end{aligned} \tag{3.6}$$

We can obtain equation 1.29 in the particular case in which the refraction index is independent from the energy of the photon. The integral simplifies to

$$I_0 = \frac{1}{n^2}(E_{\text{max}} - E_{\text{min}}) \tag{3.7}$$

The number of optical photons per unit step length is calculated

$$\frac{dN}{dx} = \frac{\alpha}{\hbar c}\left(E_{\text{max}} - E_{\text{min}} - \frac{1}{\beta^2}I_0\right) \tag{3.8}$$

We obtain the formula for constant refraction index in equation 1.29 in terms of the minimum and maximum energy of the Cerenkov photons.

$$\frac{dN}{dx} = \frac{\alpha}{\hbar c}(E_{\text{max}} - E_{\text{min}})\left(1 - \frac{1}{\beta^2 n^2}\right) \tag{3.9}$$

Another algorithm evaluates the step length $L$ according to all the physics processes considered in the simulation. then, the number of optical photons in the step is calculated

$$N = \frac{\alpha}{\hbar c}\left(E_{\text{max}} - E_{\text{min}} - \frac{1}{\beta^2}I_0\right)L \equiv \langle N_{\text{step}}\rangle \tag{3.10}$$

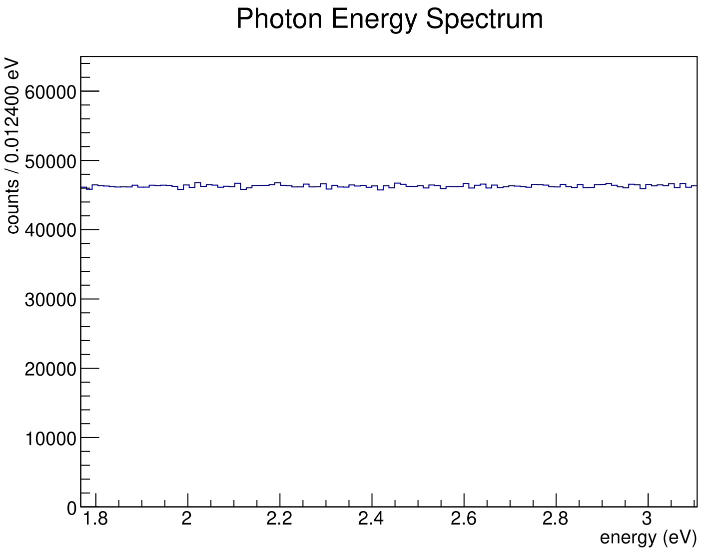


Figure 3.2: Simulated energy spectrum of Cerenkov photons.

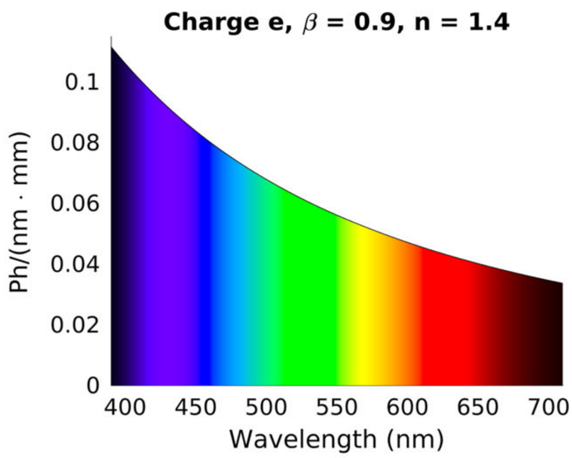


(a) Wavelength spectrum from [86].

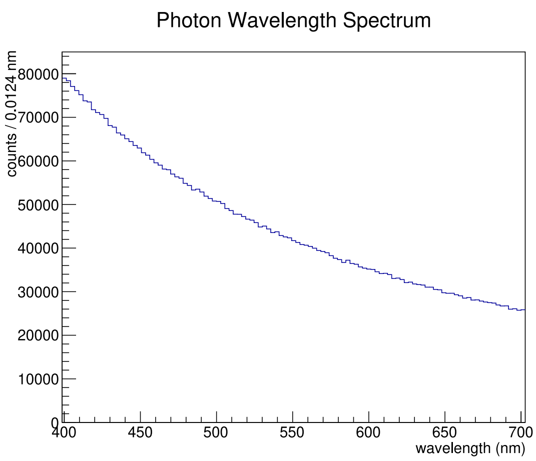


(b) Simulated wavelength spectrum.

Figure 3.3: Wavelength spectra of optical photons generated via Cerenkov effect. Comparison between a wavelength spectrum from [86] and the one we simulated with Geant4.

This value is an average quantity. The actual number of photons $N_{\text{step}}$ is picked from a Poisson distribution (see equation 2.1) with expected value $N$:

$$\text{Poisson}(N_{\text{step}}; N) = \frac{N^{N_{\text{step}}} e^{-N}}{N_{\text{step}}!} \tag{3.11}$$

We can test Geant4 algorithm for Cerenkov effect in a simple way. From equation 3.3 and in the case of refraction index independent from the optical photon energy, we expect that its energy spectrum is a box distribution. Indeed, the simulated energy spectrum in figure 3.2 shows exactly this trend. The limits of the box distribution are determined by range in which the refraction index is declared.

Also the $1/\lambda^2$ dependence of the wavelength spectrum is correctly simulated. In figure 3.3 the distribution expected by theoretical calculations [86] is compared with a simulation: the trend is similar.

## 3.4 Geant4 Simulation of Scintillation

In Geant4, scintillation is one of the process able to generate optical photons. Some macroscopic properties of a medium can be specified in order to control the scintillation parameters.

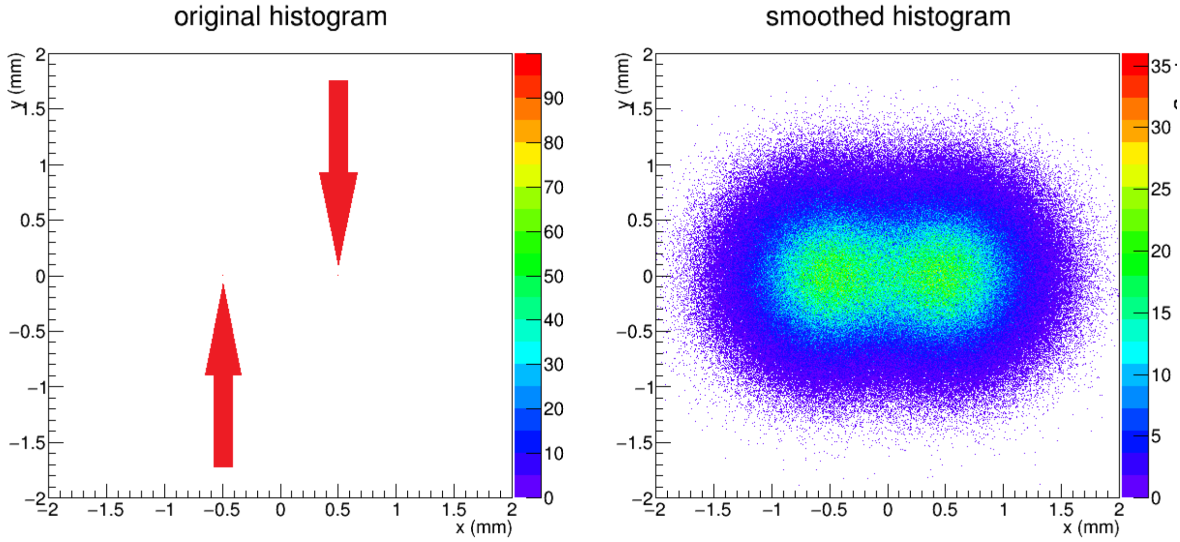


(a) Original 2D histogram.

(b) Resulting histogram after the smoothing procedure.

Figure 3.4: Method used to apply a Gaussian blur to the simulated images.

A scintillator material must be defined with some parameters, such as: the number of optical photons produced in the process (yield), the energy spectrum of these photons and the time distribution of the photon generation events. Default parameters are available. The yield can be specified according to the type of primary particle. The distribution of the emission times can be further characterised by an exponential rise time and a decay time with one or more time constants [87].

The frequency of the scintillation photons is sampled from an empirical spectrum that one can set in input. The photons originate along the track segment of the primary particle and are uniformly emitted in the full solid angle. They have a random linear polarization perpendicular to their momentum direction.

## 3.5 Gaussian smoothing of the simulated images

Gaussian blurring or Gaussian smoothing an image consists in blurring the image using a Gaussian function. It can be useful to reduce the noise level but in our case it is used to mimic the real blurring due to the optical system that takes place during the experiment. Typically it is achieved by folding the image with a Gaussian kernel [88][89].

We obtained Gaussian blur without using a kernel. We manipulated the output files from Geant4 simulation. These files are easily analyzed with ROOT software. ROOT is a framework for data processing [90] [91].

We considered a normalized 2-dimensional Gaussian function centred in the origin of the space:

$$G(x, y, \sigma) = \frac{1}{2\pi\sigma^2} \exp\left(-\frac{x^2 + y^2}{2\sigma^2}\right) \tag{3.12}$$

We used this function as PDF for the contents of each bin of an image produced as output from the Geant4 application. Figure 3.4 represents this algorithm. The starting image (figure 3.4a) has only two bins with non-zero content, since they are very small we drew two red arrows that pinpoint them. Considering one bin of the starting image, a random number with equation 3.12 as PDF is extracted for as many time as the content of the considered bin and the extracted number is filled to a new 2D histogram. This action is repeated for every bin in the starting image. The resulting image is shown in figure 3.4b.

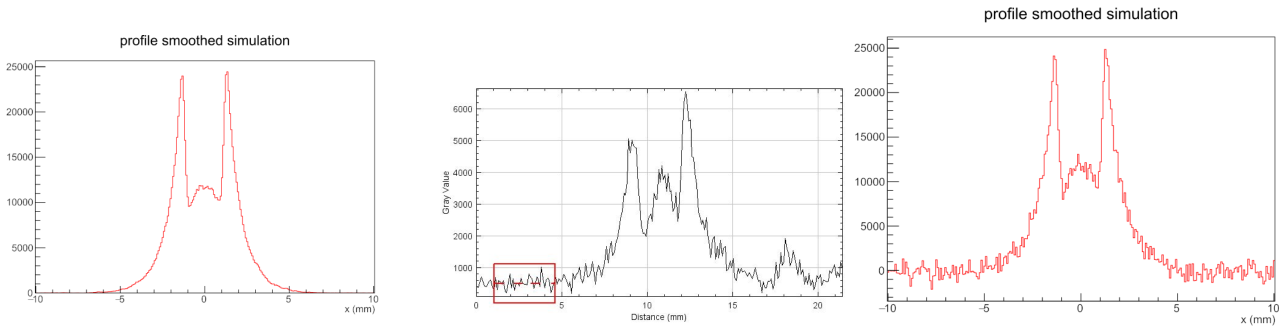


(a) Simulated profile without noise.

(b) Experimental profile. A window in the outskirt of the distribution is selected.

(c) Simulated profile with noise.

Figure 3.5: Method used to simulate noise in 1D histograms.

## 3.6 Noise model

The experimental images we acquired were subjected to several sources of noise, that we described in section 2.1. Instead, the images that we simulate are free of noise. It is easier to appreciate these different features observing the 1D histogram profiles obtained slicing the 2D images. When the number of simulated events is enough big and the binning is enough dense, the simulated sliced profiles look like smooth curves in contrast with the jagged curves of the experimental profiles.

We cannot directly use the noise-free simulations to evaluate the spatial resolution. In fact, virtually cylinders of any size can be distinguished with enough statistics and enough bins in our simulations. For the aim of this thesis, we do not need a very detailed model of noise for each 2D image. We will follow a more simple and empirical approach adding noise directly to the 1D histograms of the profiles. We will proceed as follow:

1. consider the simulated profile (figure 3.5a) and the simulated profile (figure 3.5b) of the same object;
2. select a window on the border of the experimental profile in which the trend is constant and we can expect that only noise is contributing to the bin contents;
3. estimate the standard deviation of the bin contents with respect to the average bin content;
4. scale the standard deviation by multiplying it for

$$\frac{\text{maximum bin content of the simulated profile}}{\text{maximum bin content of the experimental profile}} \tag{3.13}$$

5. build a normalized Gaussian function with such standard deviation;
6. add to every bin content of the whole simulated profile random number extracted from such Gaussian PDF.

The resulting simulated profile (figure 3.5c) should have noise whose impact on the spatial resolution is similar to the experimental profile.

# Chapter 4

# Experiment

## 4.1 Description of the phantoms

Phantoms are objects with a well defined 2D or 3D structure that are used to calibrate and optimize imaging systems. In principle, knowing both the structure of the source and the image, it is possible to deduce the response function of the imaging system.

Phantoms used in this type of applications share a structure based on several pattern of cylinders drilled in a box of uniform material. This feature is typical of Jaszczak (or Derenzo) phantoms, that are commonly used to evaluate the spatial resolution of PET systems [66][93]. In figure 4.1 there is an example of this type of phantoms. The diameter of the cylinder, that is also equal to the smallest distance between two cylinders, corresponds to the spatial resolution that is assessed: if the cylinders are distinguishable then the system has at least this resolution otherwise it has a worse one.

We used three type of phantoms during the experiment. We can describe them according to their material and to the diameters of the cylinders:

1. transparent PMMA made with diameters from 0.70 mm to 2.5 mm;
2. opaque HDPE made with diameters from 0.70 mm to 2.5 mm;
3. transparent material made with diameters from 1 mm to 11.5 mm.

From here on in we are going to refer to them as PMMA phantom, HDPE phantom and Roma phantom respectively.

Figure 4.1: Example of Jaszczak phantom. From [92].

| Diameter (mm) | Surface (mm$^2$) | Depth (mm) | Volume (mm$^2$) | n° cylinders | Volume (mm$^3$) |
|---|---|---|---|---|---|
| 0.7 | 0.4 | 10 | 3.8 | 7 | 26.9 |
| 1.0 | 0.8 | 10 | 7.9 | 7 | 55.0 |
| 1.5 | 1.8 | 10 | 17.7 | 7 | 123.7 |
| 2.0 | 3.1 | 10 | 31.4 | 7 | 219.9 |
| 2.5 | 4.9 | 10 | 49.1 | 3 | 147.3 |

Table 4.1: Features of the phantom realized at LNL. The second column named *Volume* refers to the sum of the volume of all the cylinders of the same diameter.

### 4.1.1 Phantom project and realization

Looking at the articles available in literature we expected a resolution between 1 mm and 2 mm [66]. Therefore, we prepared a design to explore the resolution in this range of distances.

As already mentioned, the structure is fundamentally derived from Jaszczak phantoms' one: a uniform volume with a pattern of empty cylinders that can be filled with a solution containing the radionuclide. Typically, phantoms used for PET and SPECT have a kind of cylindrical symmetry because there is a relative rotation between the phantom and the detectors. Instead, since the instrument we are investigating performs 2D imaging from a single point of view, we found more convenient to build the phantom within a box shape.

The project of the phantom was built with FreeCAD software. FreeCAD is a parametric 3D Computer-Aided Design (CAD) modeler for general purposes. Its development is completely open source (LGPL License). FreeCAD is aimed directly at product design and mechanical engineering but also fits in a wider range of uses around engineering, such as 3D printing, finite element analysis, architecture, and other tasks [94].

The drilled holes are inside an area of 4 cm$^2$, there are:

- 3 cylinders of 2.5 mm diameter
- 7 cylinders of 2.0 mm diameter
- 7 cylinders of 1.5 mm diameter
- 7 cylinders of 1.0 mm diameter
- 7 cylinders of 0.7 mm diameter

The cylinder of equal diameter are grouped together in structure of single or repeated triangles. The side of each triangle is equal to two times the diameter of the cylinders. In table 4.1, there are all the info about the phantom realized at LNL. The volumes $V$ are estimated as cylindrical volumes:

$$V = \Sigma h = \pi r^2 d = \pi \frac{d^2}{4} h \tag{4.1}$$

where $\Sigma$ is the surface of the single cylinder, $h$ is its depth, $r$ is its radius and $d$ is its diameter.

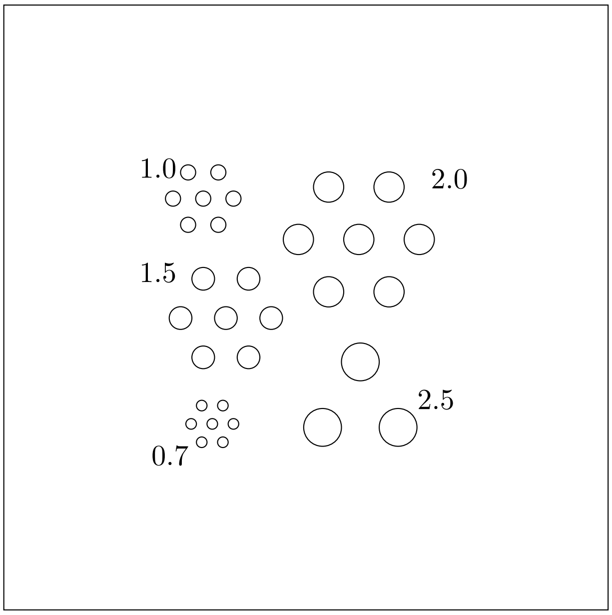


(a) Scheme of the phantom that was produced at LNL as seen from below. The numbers indicate the length in mm of the diameters of the cylinders as well as the distance between the ones of equal diameter.

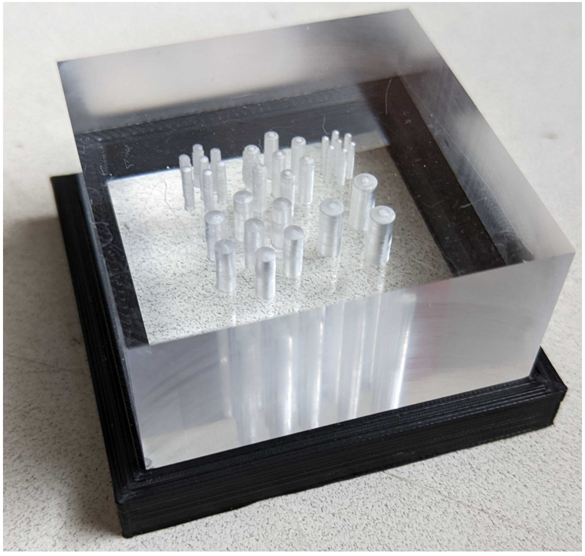

(b) Photo of PMMA phantom that was produced at LNL.

Figure 4.2: Phantom realized at LNL.

Figure 4.2a shows the pattern of the holes. The triangles and hexagons are clearly visible.

The workshop of LNL realized 10 copies of this model:

- 5 in Poly(Methyl MethAcrylate) (PMMA)
- 5 in High-Density PolyEthylene (HDPE)

PMMA is a transparent material with refraction index of about 1.5 for photons in the visible range. Instead, HDPE is opaque. We made copies in these two materials to evaluate the situation in which Cerenkov effect takes place only in the volume of the cylinder (where the radioactive material is stored) and the one in which it appears also in the surrounding volume.

| Diameter (mm) | Surface ($mm^2$) | Depth (mm) | Volume$_s$ ($mm^2$) | n° cylinders | Volume$_g$ ($mm^3$) |
|---|---|---|---|---|---|
| 1.0 | 0.8 | 19.0 | 14.9 | 3 | 44.8 |
| 1.5 | 1.8 | 19.0 | 33.6 | 3 | 100.7 |
| 2.0 | 3.1 | 19.0 | 59.7 | 3 | 179.1 |
| 3.0 | 7.1 | 19.0 | 134.3 | 3 | 402.9 |
| 4.0 | 12.6 | 19.0 | 238.8 | 3 | 716.3 |
| 5.0 | 19.6 | 19.0 | 373.1 | 3 | 1119.2 |
| 6.0 | 28.3 | 19.0 | 537.2 | 3 | 1611.6 |
| 7.0 | 38.5 | 19.0 | 731.2 | 3 | 2193.6 |
| 7.5 | 44.2 | 19.0 | 839.4 | 3 | 2518.2 |
| 8.5 | 56.7 | 19.0 | 1078.2 | 3 | 3234.5 |
| 10.0 | 78.5 | 19.0 | 1492.3 | 3 | 4476.8 |
| 11.5 | 103.9 | 19.0 | 1973.5 | 1 | 1973.5 |

Table 4.2: Features of Roma phantom. The column named Volume$_s$ refers to the volume of a single cylinder, the column named Volume$_g$ refers to the volume of a all the cylinder with the same diameter.

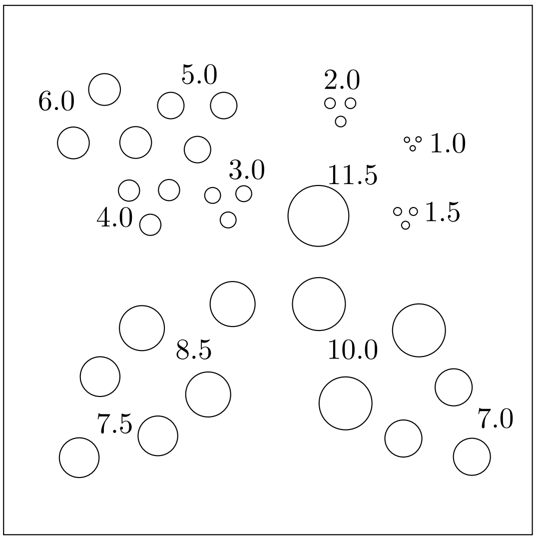


(a) Scheme of Roma phantom as seen from below. The numbers indicate the length in mm of the diameters of the cylinders as well as the distance between the ones of equal diameter.

(b) Photo of Roma phantom.

Figure 4.3: Phantom produced by another group.

Roma phantom was produced by another group and was used during the experiment too. It is bigger in size than the phantoms produced at LNL, in fact its biggest cylinder has a diameter of 11.5 mm. We used it because we discovered DRI spatial resolution could not be assessed using the phantoms we designed. Figure 4.3a shows a scheme of this phantom and table 4.2 contains the information on the geometry of the holes.

### 4.1.2 Spacers and wedges

In in-vivo experiments with mice, the lesion will not be on contact with the support of the sample room. Instead, there will be a finite distance. We expect a detriment of the spatial resolution and of the contrast resolution increasing depth because:

**for CLI** the optical photons are more attenuated and scattered if they have to travel more distance in a absorbing and scattering medium, that is the mouse body.

**for DRI** if the distance between the source and the scintillator increases then gamma-rays originated from a single point will generate larger circles of optical photons in the scintillator screen.

In order to find out how much the depth affects the spatial resolution, we realize six spacers to be

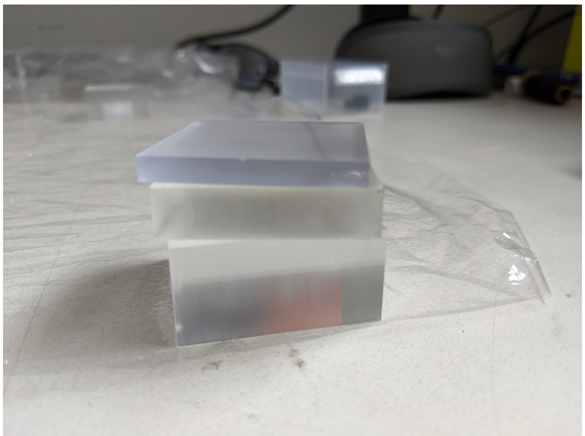

(a) Three wedges of transparent material.

(b) Three spacers with plastic boundaries.

Figure 4.4: Wedges and spacers realized at LNL.

Figure 4.5: PLA tile of thickness 1.75 mm 3D-printed.

inserted between the phantoms and the sample room floor. They vary in

- thicknesses: 5 mm, 5 mm, 5 mm;
- material: transparent material (see Figure 4.4a) and air (see Figure 4.4b)

In order to have air as material we designed a frame with FreeCAD. Then, the Standard Triangle Language (STL) files were transformed into a gcode file containing the instructions to be given to the 3D printer in order to print the volume. This transformation was executed by PrusaSlicer, a slicer software [95]. The 3D printer is located inside the LNL, for these prints we used a Poly(Lactic Acid) (PLA) wire.

Also some PLA tiles of thickness 1.5 mm and 1.75 mm were 3D printed. They original scope was to stop optical photons produce by Cerenkov effect during DRI acquisitions but during the experiment we also used them to put a small distance between the phantom and the sample support. Figure 4.5 shows one of these tiles.

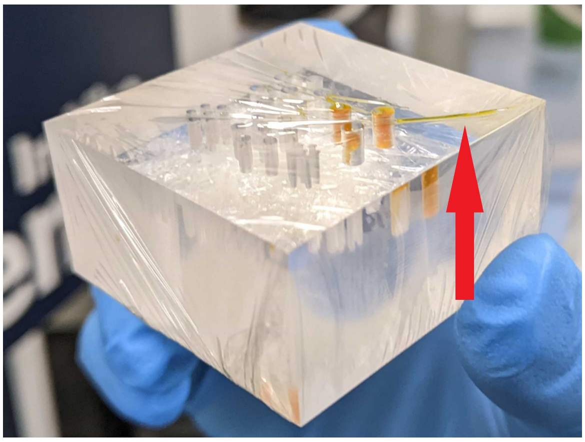

(a) Phantom where leakage occurred, it is pointed out by the red arrow.

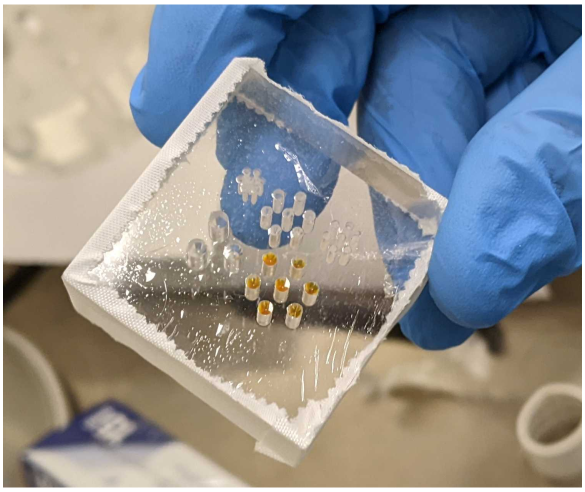

(b) Phantom where no leakage occured.

Figure 4.6: Two PMMA phantoms are filled with the dyed solution and sealed with the plastic wrap.

### 4.1.3 Critical aspects of the phantom design

In regards of the phantoms produced at LNL, their design was based on the possibility to turn them upside down without any leak of solution due to gravity. In order to avoid leakage, the plan was to add agar, a phycocolloid extracted from a group of red-purple marine algae, to the radioactive solution. Agar is a gel at room temperature and is typically used for solidifying culture media [96]. The filling procedure we planned while designing the phantoms for the experiment was the following:

1. add agar to the solution containing the radionuclide
2. fill each hole of the phantom using a 10 mL syringe for insulin injections
3. heat the phantom turning the liquid solution into a gel
4. turn the phantom upside down

The risk of radionuclide leakage would be eliminated by using agar.

In the experiment site, we found out that the volume of the holes was too small to implement this recipe:

- the phantom cylinders of 0.7 mm diameter were too small to be filled with the syringe
- even in the larger cylinders, the agar would solidify too quickly because of the small volume of the cylinders preventing a proper filling

Therefore, plastic wrap (for food conservation [97]) was used to keep the liquid solution inside the holes when the phantom was turned upside down. The film was stretched from the side of the phantom where there are the holes apertures to the opposite side. Correct sealing was verified looking at the eventual presence of colored solution on the phantom surface, for instance, figure 4.6a shows a phantom that was discarded due to leakage and figure 4.6b shows a phantom perfectly sealed. This method worked fine only with the phantoms made of PMMA. It did not work with the phantoms made of HDPE because the machining left bumps on the surface at the entrance of the holes causing a lack of adherence of the plastic wrap to the phantom surface. Then, leakage of the solution in the surrounding surface of the HDPE phantom was unavoidable.

| Isotope | First day | | | Second day | | |
|---|---|---|---|---|---|---|
| | Time | Activity (MBq) | Volume (mL) | Time | Activity (MBq) | Volume (mL) |
| Ga-68 | 10:00 | 41.75 | 10 | 9:53 | 46.40 | 10 |
| Tc-99m | 14:50 | 25.73 | 10 | 16:43 | 22.20 | 10 |

Table 4.3: Activity and volume of the radionuclides employed in the experiment. The first row indicates the day of the measurement.

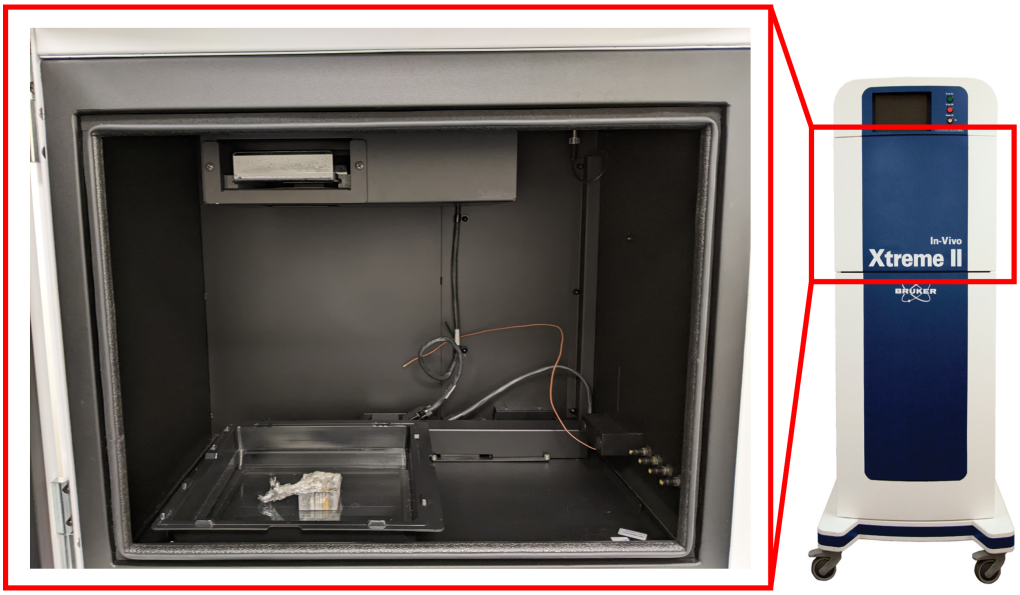


Figure 4.7: Phantom inside the sample room of the Bruker In-Vivo Xtreme II. The whole body picture is taken from [65].

## 4.2 Description of the experiment

We describe the experiment at CAPiR at Catania in which we participated. The Bruker In-Vivo Xtreme II instrument is placed in a room inside a vivarium.

Cannizzaro hospital supplied the radionuclides for the experiment: Ga-68 and Tc-99m [98]. The choice of these radionuclides was driven by:

- the possibility to investigate radiation as close as possible to the one that characterize Ag-111, namely $\beta$ radiation and $\gamma$ radiation (see table 4.4);
- the availability of the dealer and the cost of the sources.

The radionuclides were dissolved in a solution with water as solvent. The delivery of such solutions was performed two times, one for each day of the experiment. In table 4.3 I report the initial activity values, the time at which the measurement was executed and the total volumes of the radioactive solutions. The activity was measured with an Isotope Calibrator: Curiementor 3 produced by PTW-FREIBURG.

The solution was mixed with a dye, bromophenol blue, in order to facilitate the filling procedure of the phantom. In hindsight, we suspect that the dye increased the absorption of optical photons in the solution, a more accurate description of this aspect can be found in section 5.1 on page 43.

Once the solution was prepared, it was used to fill some of the holes of the phantoms. The top door of the instrument was opened allowing the insertion of the filled phantom just above the sample support (figure 4.7). The sample support is realized with a thin layer of flexible and transparent material that is kept stretched by a plastic frame. Its main function is to protect the screens (such as the radiographic screen in figure 2.2a) by isolating the sample from the floor. The door of the acquisition chamber is

| Isotope | Half-life | Type | Mean energy (keV) | Intensity (%) |
|---|---|---|---|---|
| Ga-68 | 68 m | $\beta^+$ | 836 | 88 |
| | | $\beta^+$ | 353 | 1 |
| | | $\gamma$ | 511 | 178 |
| Tc-99m | 6 h | CE | 2 | 86 |
| | | $\gamma$ | 141 | 89 |
| Ag-111 | 7 d | $\beta^-$ | 360 | 92 |
| | | $\beta^-$ | 224 | 7 |
| | | $\beta^-$ | 279 | 1 |
| | | $\gamma$ | 342 | 7 |
| | | $\gamma$ | 245 | 1 |

Table 4.4: Decay radiation information about Ag-111 and the radionuclides employed in the experiment.

made of a high atomic number material to effectively attenuate gamma-rays and X-rays. The door was shut completing the safety shell against gamma-ray exposure that guarantees radio-protection of the users with respect to the radioactive sample in the sample room and with respect to the X-rays generated during X-rays acquisitions.

Two days of measurements in a row were planned. In the morning of each day Cannizzaro hospital supplied a load of both Ga-68 and Tc-99m. Due to the different half-life of the radionuclides, we decided to take the acquisitions in the following order:

1. Ga-68 acquisitions in the morning
2. Tc-99m acquisitions in the afternoon

because the first radionuclide decays faster than the second one (see table 4.4).

### 4.2.1 Activity of the sources

Evaluating the activity used in each acquisition is not straightforward due to experimental issues. We measured the activity at a certain time and the volume of the solution, from which we can estimate the initial specific activity (Bq/mL).

Then, applying the exponential decay law (equation 1.5) we can derive the activity concentration at any time (before or after the initial time). The initial activity in an acquisition at time started at time $t$ is given by

$$A(t) = \rho_{\text{activity}}(t)V \tag{4.2}$$

where $V$ is the volume of solution deployed in the phantom for the acquisition.

We used the initial activity concentration reported in table 4.3. The volumes of solution are approximately assumed to be equal to the volumes of the cylinders in which the solution is poured. The volume of the cylinders are reported in table 4.1 and in table 4.2.

## 4.3 Uncertainties affecting the experiment

In this experiment there are many sources of uncertainty so it is difficult to define a proper uncertainty for the estimations that we will report. We describe the sources that we identified.

- The total activity of the Ga-68 and Tc-99m solutions has a relative error indicatively of the order of 1 % [99].
- The depth of each cylinder that was drilled in the PMMA phantom varies due to uncertainty in the machining. Measuring the depth of a sample of cylinders, we obtained values between 9 mm and 10 mm.

- The volume of solution delivered in each hole varied for each one because the filling procedure was affect by some uncertainties, we explain more in details this issue later in this section.
- The distances along the vertical direction, such as from sample support to phantom or from scintillator screen to phantom, were calculated summing the thicknesses of the various objects but we could not measure the thickness of the sample support and the thickness increment due to plastic wrap and adhesive tape. An uncertainty of about 0.5 mm is reasonable for these lengths.

The main source of uncertainty regarding the estimation of the activity in the samples is the variability of the volume of solution that was injected in each cylindrical hole. Air bubbles, especially for diameters smaller than 2.0 mm were almost unavoidable and difficult to remove. Nevertheless the use of the dye to assess the proper filling allowed us to reach a certain confidence that at least half of each cylinder was always occupied. We roughly estimate that repeated measurements of solution volumes would fall in a range of the order of $\pm 30\,\%$ with respect to the values reported in table 4.1 and 4.2.

$$\frac{\sigma_{\text{volume}}}{\text{volume}} \simeq 30\,\% \tag{4.3}$$

As we already emphasized in section 1.2, we do not claim a rigorous statistical reliability, a reasonable estimation is enough in this context. Of course, future experiments that aim to precisely quantify the response of the instrument need a proper uncertainty estimation that goes beyond the order of magnitude that we just gave.

# Chapter 5

# Data Analysis

## 5.1 Analysis of the images acquired during the experiment

The Bruker Molecular Imaging Software saved the acquired images as BIP files [59]. Since this format is proprietary and we do not have software that could read this format, the collaborators from Catania kindly exported all the images in DICOM. Then we could access the value of each pixel in the image through a python script.

The CCD is made of 2048x2048 pixels (4 MP) but pixels can be grouped together in order to enhance the sensitivity at the expenses of the spatial resolution. Some of the images were acquired with a 4x4 binning (512x512 super-pixels) while the remaining others with no binning, thus keeping the original number of bins.

As usually done in this field, images are presented as 2D matrices with a certain color scale. Then, assessing whether the points are distinguishable or not is decided qualitatively. A more precise analysis, as already discussed in section 1.6 on page 6, is tricky and unnecessary for the aims of this thesis. Some experimental images in this chapter are accompanied by schemes of the radionuclide positions.

In this analysis, we use also 1D histograms extracted from the 2D images with the following steps (that are represented graphically in figure 5.1):

1. select about ten pixels in the x or y directions (figure 5.1a)
2. sum the content of these pixels in order to obtain a single array of values (figure 5.1b)
3. plot the resulting 1D histogram (figure 5.1c)

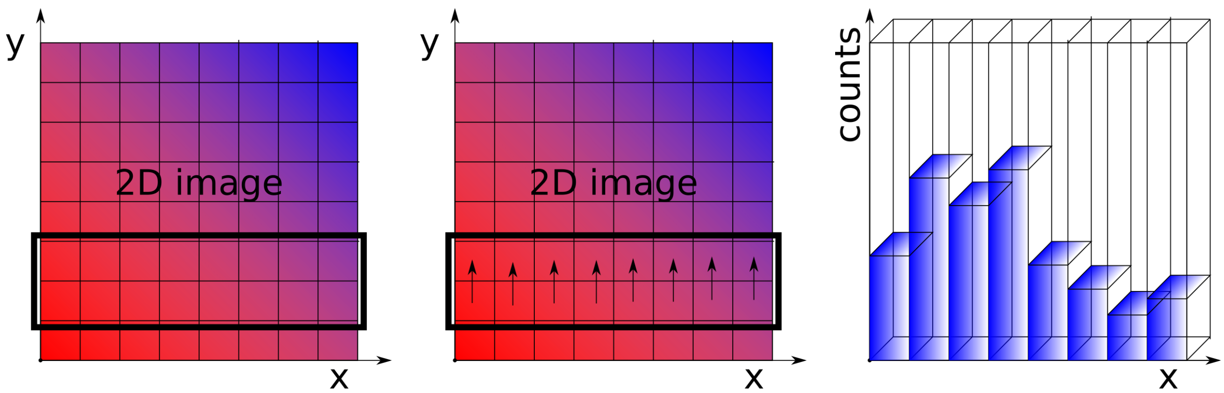


(a) First step. Selection of the pixels.

(b) Second step. Sum of the contents along one direction.

(c) Third step. Plot of the resulting 1D histogram.

Figure 5.1: Method used to slice 2D images into 1D histograms.

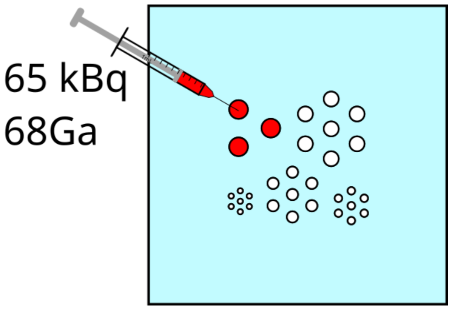


(a) Scheme of the radionuclide source layout.

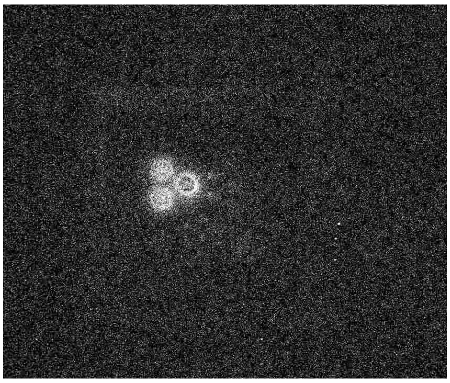

(b) Experimental 2D image acquired with the instrument.

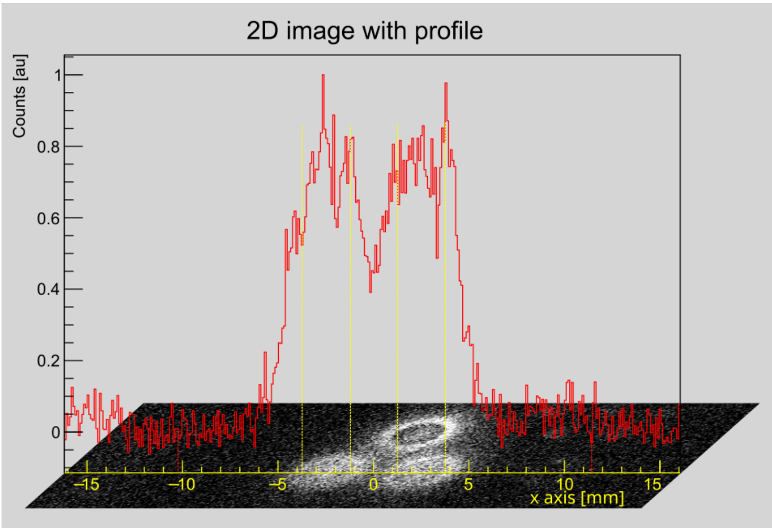


(c) Experimental 2D image sliced along two centres. The correspondent 1D histogram (red line) is superimposed with the x-axis passing along the same direction of the slice. The yellow dashed line helps the eye of the reader in recognizing the borders of the cylinders of 2.5 mm diameter.

Figure 5.2: Example of image acquired during the experiment, the source is Ga-68 and the acquisition mode is Luminescence.

We refer to the 1D histogram as a *slice* of the image.

As example, figure 5.2 shows the image of 2.5 mm diameter cylinders of PMMA phantom filled with Ga-68.

All the experimental images shown in these thesis are obtained processing the DICOM files with ImageJ software [100]. ImageJ is an image processing program. It can be used to display images but also to edit and analyze them [101]. It can read several image format including DICOM and TIFF. Many tools for analysis are available, such as profile plot and length calibrator [102]. We used ImageJ also to slice the 2D images. For instance, figure 5.2c shows a profile obtained slicing figure 5.2b. In the x-axis of the profile there is the distance in millimeters and in the y-axis there is a quantity named Counts (or Gray Value in other profiles) that corresponds to the content of the bin. ImageJ can perform slices also in direction with an angle with respect to the x- and y-axis.

It is worth noting that during the experiment we initially kept the same acquisition time used for CLI (2 min) also for DRI. Instead, we found that the images saturated already when the acquisitions last for more than 10-20 seconds. Evidently, the yield of optical photons due to scintillation on the phosphor screen is much greater than the one due to Cerenkov effect. So, in general, CLI requires an

| Binning option | conversion factor (mm / pixel) |
|---|---|
| 1x1 | 0.085 |
| 4x4 | 0.021 |

Table 5.1: Factors to change the axis unit from pixel to millimeter according to the binning used in the image.

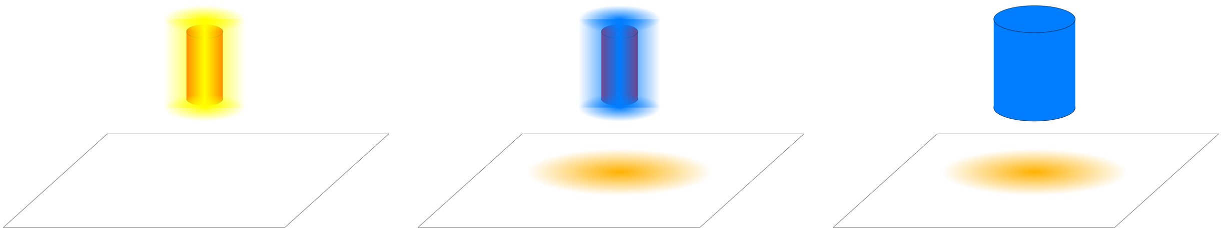

(a) Scheme of CLI for Ga-68. The light object is a halo wrapped around the radionuclide object.

(b) Scheme of DRI for Ga-68. The gamma-ray object is a halo wrapped around the radionuclide object. The light object is a circle in the phosphor screen.

(c) Scheme of DRI for Tc-99m. The gamma-ray object coincide with the radionuclide object. The light object is a circle in the phosphor screen.

Figure 5.3: Scheme that indicates where the optical photons collected by the CCD are generated in both CLI, DRI and for both Ga-68, Tc-99m. The radionuclides are deployed within a cylindrical volume, as in the real experiment.

acquisition time one order of magnitude larger than DRI.

## 5.2 Characterization of the spatial resolution

The light sources used in the experimental acquisitions are very complex:

- have wavelength with a continuous distribution
- have different intensity due to uncertainties in the filling procedure of the cylinders
- are not point-like due to the nature of the mechanisms that produce the optical photons

Furthermore, we shall not think that the final image is directly a photo of the sample as we see it with our own eyes. From the solution containing the radionuclides to the final image there is an additional level that can be considered as object. In the following list we define these three levels:

**Radionuclide object** The solution containing the radionuclide is the object we are interested in reconstruct via imaging. Indeed, determining the trajectory of the radiopharmaceutical is the aim of the pre-clinical studies.

**Light object** The ensemble of points in the 3D space from where the optical photons are indeed generated constitute the object from a ray optics point of view.

**Light image** The points in which the optical photons intercept the CCD constitute the light image from a ray optics point of view.

In the same fashion, we may define an intermediate level between the radionuclide object and the light object that is useful when discussing DRI:

**Gamma-ray object** The ensemble of points from where the gamma-rays are generated.

We will use the term light image also to indicate the image in which the axes are scaled so that the light object dimensions are preserved. Table 5.1 contains the conversion factors for the binning options used in our experiment.

Rayleigh criterion (that we introduced in section 1.6) assumes that the real object is a point in the 3D space. Instead, the real objects in our experiment have a much more complex shape. First, the radionuclide objects occupy approximately the same volume of the phantom holes, thus, they are cylinders. Second, the real object develop differently according to both the imaging modality and the radionuclide used. We will see here the cases of interest:

**CLI with Ga-68** The Ga-68 nuclei contained in the solution emit energetic positrons that travel for some distance in the surrounding material. The optical photons are generated in a kind of cylinder that is larger than the solution cylinder. Note that the density of optical photons is not uniform across the this second cylinder (the real object) because: the solution and the phantom material have different optical properties and the trajectories of the positrons in the media (that we described in section 1.8) is far from simple.

**DRI with Tc-99m** The Tc-99m nuclei contained in the solution can be approximately assumed to be at rest. They emit gamma-rays in an isotropic fashion. Then the optical photons are produced when the gamma-rays interact with the scintillator screen. In this case, we can say that the real object is 2-dimensional because all the optical photons are generated within the screen whose thickness is much less than the typical depth of the phantom holes. Considering only one cylinder of radioactive solution, the real object is expected to be a circle with non-uniform optical photons intensity.

**DRI with Ga-68** In this case the real object is given by three different contributions. In regards to the gamma-rays scintillating in the screen, the same discussion provided for DRI with Tc-99m holds. Instead, differently from Tc-99m, we have to consider that the gamma-rays object is not the solution volume because Ga-68 produce gamma-rays (annihilation radiation) at the end of the positrons track. Therefore, the gamma-rays originates from a larger distribution than the radionuclide object. Scintillation photons are generated also by the positrons themselves, that can travel a few millimeters around their original position.

The optical photon acquisition part of the instrument is fed in input with the real object and produce in output the real image. We assume that the response function of this part can be modeled with a Gaussian function. The variance of which will be determined approximately in this thesis.

Figure 5.3 represents in an intuitive way all the imaging modalities discussed in this section.

## 5.3 Data Analysis for Cerenkov Luminescence Imaging

### 5.3.1 Cerenkov Luminescence Imaging with Ga-68 in PMMA phantom

For Ga-68 in CLI mode we used the phantom made at LNL (see figure 4.2a). For phantom in PMMA and cylinder diameter 2.5 mm the experimental image is shown in figure 5.4 on the facing page. Most of the features of this image can be recognized also in other images acquired with the same modality but with filled cylinders of smaller diameter.

The circular boundary of the cylinders is clearly visible since the inside (solution with the radionuclide) has much less counts than the outside (PMMA). Thus, in the 2D image every cylinder looks like a bright ring on the dark background. These rings have a sharp inner edge and a blurry outer one. The external blurriness of the signal gives rise to a bright halo around the ring.

The distance between the cylinders is enough big that the halos of the three different cylinders are distinguishable. The inside of the two cylinders on the left is not as dark with respect to the outside as for the cylinder on the right. We think that this difference in the features of the signal is due to experimental issues. For instance, the two cylinders on the left may have been filled partially. An analogous problem shows up for the images of the cylinders with 2.0 mm diameter. As explained by the scheme in figure A.1c on page 80, we intended to fill evenly all the cylinders with the radioactive solution. Instead, looking at the 2D image in figure A.1d, we see that some rings are more luminous than others and some cylinders almost do not have a corresponding ring at all.

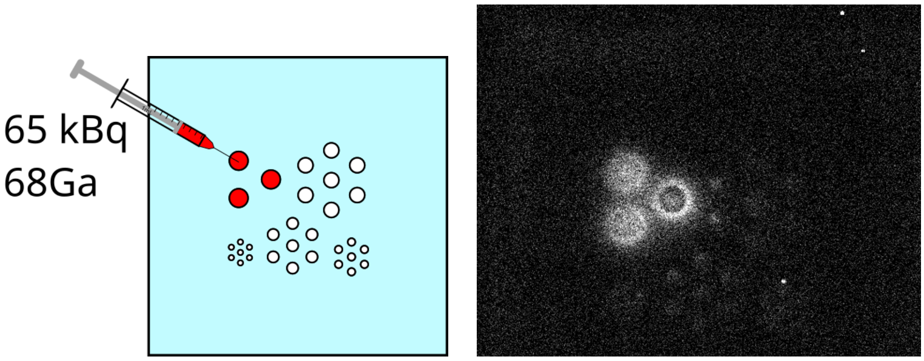


(a) 2.5 mm diameter cylinders are filled. (b) Experimental 2D image.

Figure 5.4: Experimental images: radionuclide is Ga-68 in 2.5 mm diameter cylinders of PMMA phantom. Acquisition mode is CLI and acquisition time is 2 min.

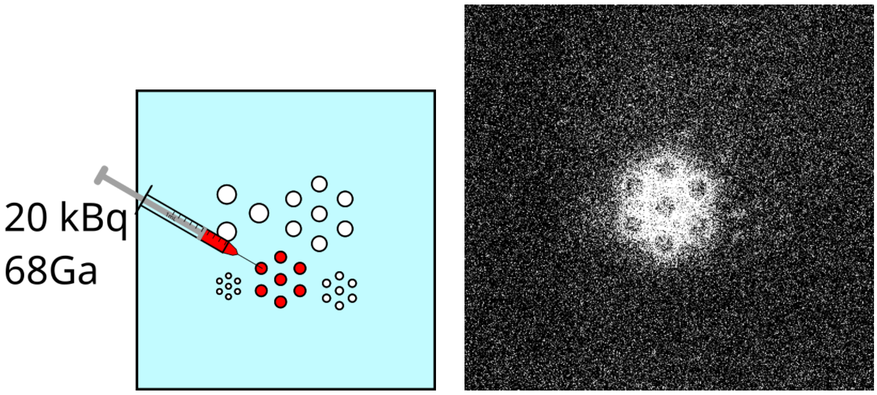


(a) 1.5 mm diameter cylinders are filled. (b) Experimental 2D image.

Figure 5.5: Experimental images: radionuclide is Ga-68 in 1.5 mm diameter cylinders of PMMA phantom. Acquisition mode is CLI and acquisition time is 2 min.

Observing carefully the experimental image in figure A.1b, one may notice also the presence of signal in the points corresponding to the other cylinders of smaller diameter. If we consider the position of the optical photons after they completed their trajectory in the phantom (instead of their origin points), then we can reproduce the same effect: signal in the sites of non-filled cylinders and with intensity that decreases the further the sites are from the filled cylinders. Since this effect is not interesting for the aims of this thesis, we will keep considering only the origin points of the optical photons in the simulations.

In figure 5.5b) we see the images for 1.5 mm diameter cylinders. In this case, the distance between the cylinders is so small that halos of different cylinders are mixed into one single bright cloud that wraps all the dark insides of the rings. A similar cloud can be seen in figure A.1h on page 80 for the image of the cylinders of 1.0 mm diameter.

In section 1.6 we introduced Rayleigh criterion to assess the spatial resolution of two point-like sources (light objects) of equal intensity. As we already stated in subsection 5.2, our light objects do not respect these conditions so we cannot directly apply Rayleigh criterion. On the other hand, we can use the same concept with a more practical approach: we refer to two cylinders as resolved if the correspondent bright rings are separated by dark regions. In the 1D profiles across the centres, this condition means that, between the two centres, there is a kind-of valley in which the counts drop. For instance, figure 5.2c shows the profile of two resolved cylinders, for $x \in [-1.25, 1.25]$ mm there is such valley. Indeed, in the corresponding 2D image in figure 5.2b we can see discern the signal of the three different cylinders.

The cylinders in figure 5.2c are the biggest ones of PMMA phantom, for the other smaller cylinders

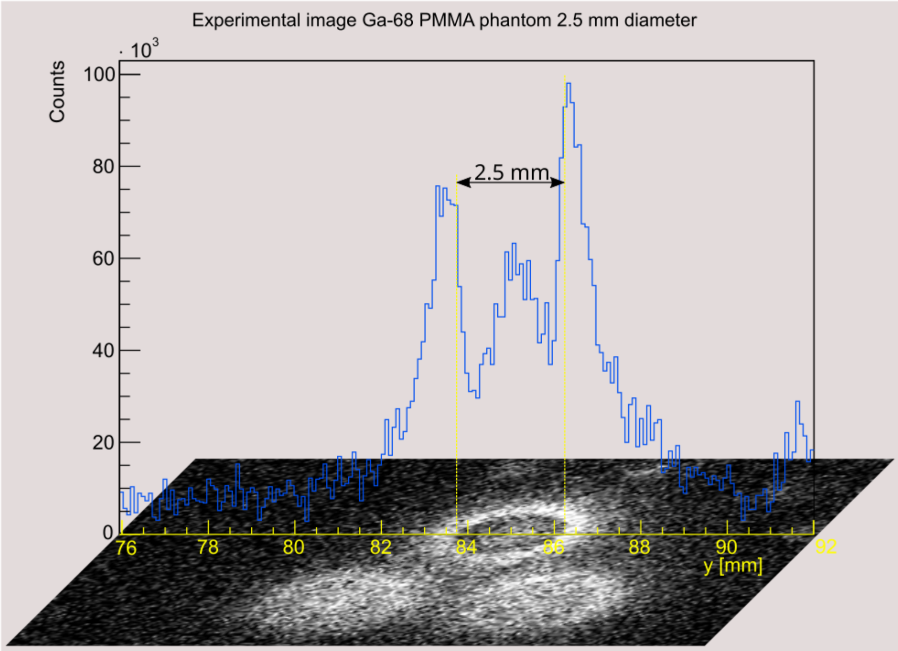


Figure 5.6: Profile across one centre for CLI with Ga-68 in PMMA phantom and 2.5 mm diameter cylinders. The x-axis of the 1D histogram indicates also the position of the slice in the 2D image. The two dashed yellow vertical lines indicate the edges of the cylinder and thus are 2.5 mm apart.

it is more difficult to discern the outside of the rings. We evaluate as resolved also the cylinders of 2.0 mm diameter. The cylinders of 1.5 mm and 1.0 mm diameter show uniform bright clouds around the cylinders and the profiles do not have any valley in the region between different cylinders.

The fact that we can always see the dark circular inside of the rings (and the corresponding valleys in the profiles) only tells us that the spatial resolution of the optical system (let us call it light spatial resolution) is much better than the 1.0 mm. The presence of the interface PMMA-solution generates a sharp border for the light object and the light spatial resolution of the instrument is so good that also the images have such sharp circular structure. On the other hand, in in-vivo experiments with mice injected with radionuclides, there is no reason to expect the presence of such interface so the images will not have this structure that is so easy to recognize.

In figure 5.6 we provide a slice passing through the right cylinder of figure 5.4b. A priori, we expected the profile to be similar to the convolution between a box and a Gaussian function. The results is very different from our expectations. We can see that there is a structure with three peaks:

- the left peak has gentle left slope and a steep right slope;
- the right peak is specular to the left one: gentle right slope and steep left slope;
- the central peak has gentle slopes at both sides and has a maximum values smaller than the lateral peaks.

The distance between the steep slopes of the lateral peaks is approximately equal to the diameter of the filled cylinders, 2.5 mm.

The shape of the profiles varies among different cylinders in the same image. Figure 5.7 on the next page shows, for instance, the profiles across the three cylinders of 2.5 mm diameter of figure 5.4b on the preceding page. It is much more difficult to recognize the increase of counts at the interface for the two cylinders on the left (figure 5.7c and 5.7d). The fact that the curve is jagged contribute in confusing the underpinning traits of the profiles.

The FWHM for the three profiles in figure 5.7 on the next page are indicated in the corresponding captions. There is not a unique peak in each profile, we assumed as maximum of each distribution the maximum bin content, without any fit. We did not subtract the background in these measurements.

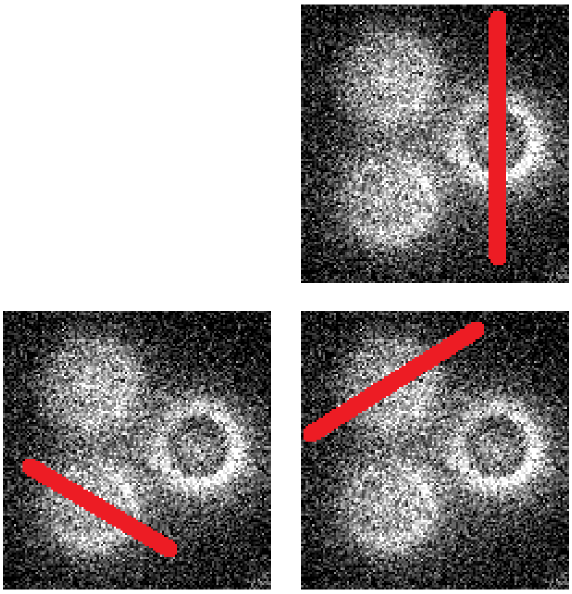

(a) Scheme of the slices positions.

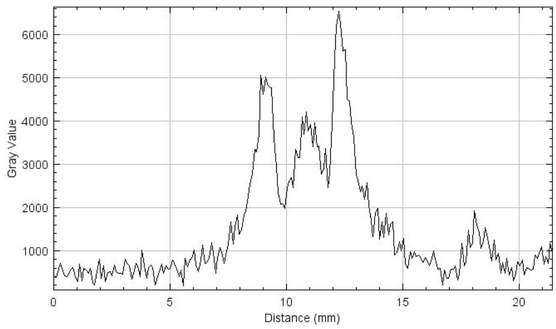


(b) Profile. FWHM is $\sim 4.2$ mm.

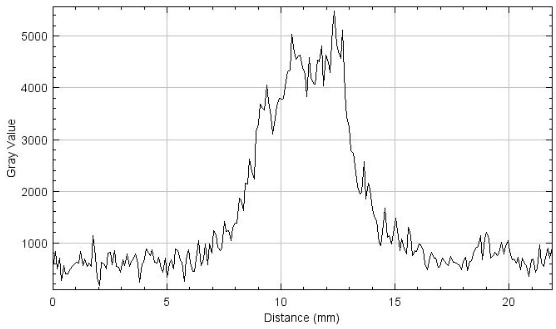


(c) Profile. FWHM is $\sim 4.4$ mm.

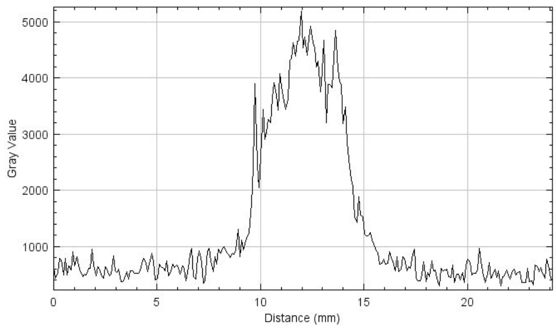


(d) Profile. FWHM is $\sim 4.5$ mm.

Figure 5.7: Profiles across the three cylinders of figure A.1b taken singularly.

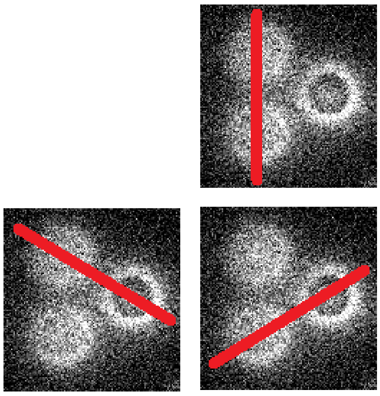

(a) Scheme of the slices positions. Each profile crosses one different cylinder.

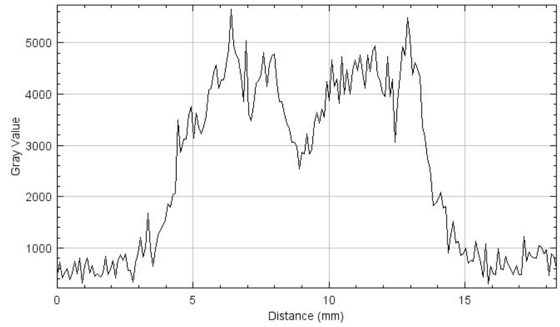


(b) Profile.

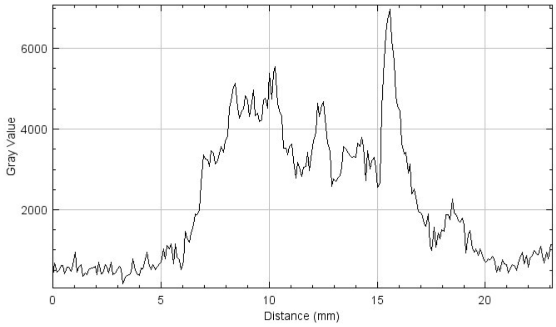


(c) Profile.

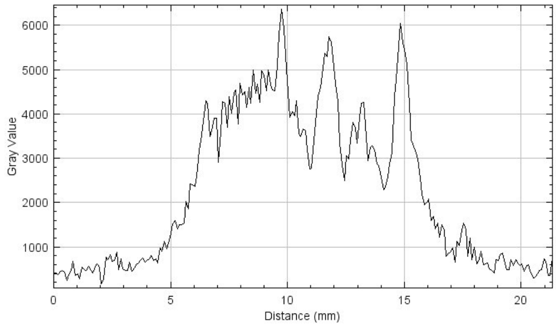


(d) Profile.

Figure 5.8: Profiles across the three cylinders of figure 5.4b.

The FWHMs differ for at most 0.3 mm that is $\sim 10\,\%$ of the measurement. We consider these small fluctuations a positive assessment of the spatial fidelity of the images.

In figure 5.8 we shows the profile of figure 5.4b on page 47 in the case of slices passing through two centers. The drop of counts in between two different cylinders is always recognizable. The presence of the drop confirms that the cylinders are resolved.

In these images with Ga-68 in PMMA phantom, each filled cylinder produces a ring distribution in almost all the images acquired (see figure A.1 on page 80). We think that this fact is compatible with a generation of optical photons that is favored in the PMMA material and close to the interface between the solution and the phantom. This behavior allows to recognize the shape of the cylinders in these images, even in the case with diameter 1.0 mm. This means that, due to a particular condition at the interface solution-PMMA, the real object is a 3D distribution with maximum intensity shaped as a hollow cylinder wrapped around the radionuclide object.

The fact that the slopes are steep but not infinitely steep can be attributed to the response function of the optical system, other than the width of the slice. We previously assumed that we could model the response function as a Gaussian function. The standard deviation of this curve will be estimated later in this section.

In simulations of CLI acquisition, the Ga-68 radionuclides are uniformly distributed over the chosen cylinders, the same cylinders that were filled in the real acquisition we are simulating. Practically, there is no time limit within a simulation so all the deployed radioisotopes decay as predicted by equation 1.13. Along some of the positrons tracks there are points in which optical photons are generated due to Cerenkov effect. The x,y,z coordinates of these points are saved. These data could be used to fill a 3D matrix that represents the discrete version of the real 3D space. Since we are not interested in the z-axis information, we could take the projection along the z-axis and get the 2D

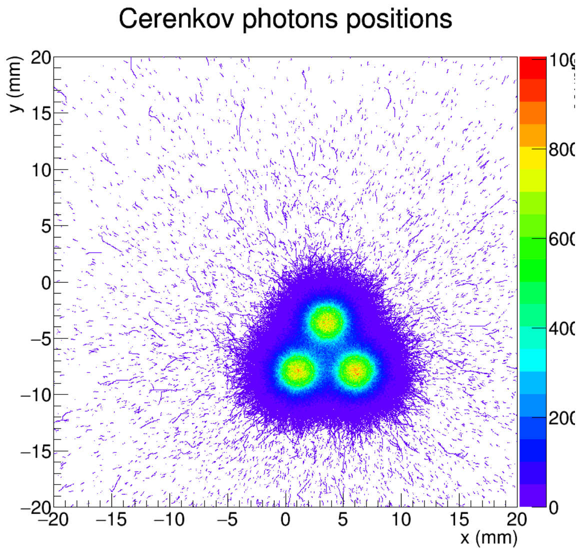


(a) Simulated image with solution refraction index equal to water one and with 100 % transmission.

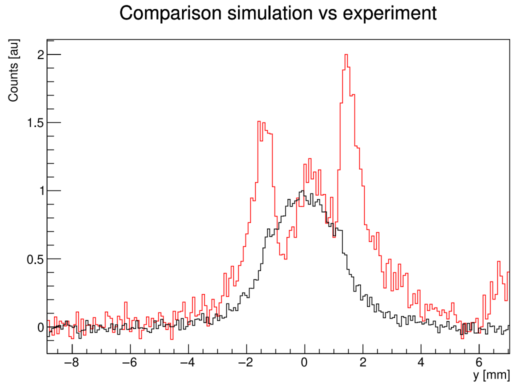


(b) Profiles of simulated image in figure 5.9a (black line) and of the experimental image in figure 5.7b (red line).

Figure 5.9: Simulation of CLI with Ga-68 in PMMA phantoms, 2.5 mm diameter cylinders. The refraction index of the solution is assumed to be the one of water. The transmission coefficient of the solution is assumed to be unitary.

matrix representing the xy plane. The method is analog to the one represented in figure 5.1 but with an additional dimension (the z-axis) and summing all the bins' contents along this dimension.

We start discussing the simulations for CLI with Ga-68 in PMMA phantoms and 2.5 mm diameter cylinders. We choose to optimize our simulations through comparison with this acquisition because it contains a very well defined ring distribution (see figure 5.6), that we think is very useful to understand what are the relevant parameters in the simulation. Initially, without any ad hoc considerations, we simulated the acquisitions simply using the refraction indexes in table 5.2 and assuming completely transparent media (media that do not absorb optical photons). The resulting 2D simulated image is shown in figure 5.9a, where the circular distributions of the cylinders are visible. This 2D image is not Gaussian blurred, in fact, we can clearly distinguish the tracks of the positrons pointed out by linear distributions of Cerenkov photons signals. On the other hand, in the profile across the centre of the cylinder on top no leaps are visible between the counts inside and outside the cylinder. Comparing the slice across one cylinder in figure 5.9b with the experimental slice in figure 5.7b we infer that the too many counts are simulated on the inside.

In the comparison of the profiles in figure 5.9b and also in all the future ones, the 1D histograms are normalized so that their height is approximately of the same order of magnitude. Therefore, the absolute number of counts in the y-axis has no meaning and should not be considered while comparing the two curves.

We can think of two different reasons that would explain the difference in the counts between the inside medium and the outside medium:

- the refraction index of the solution is much less than the refraction index of PMMA (and also less than water, the solvent);
- the solution attenuates optical photons much more than PMMA.

| Material | refraction index (adimensional) |
|---|---|
| Water | 1.34 |
| PMMA | 1.50 |
| HDPE | 1.71 |

Table 5.2: Refraction indexes of materials present in the experimental setup. Data are taken from [103][104][105].

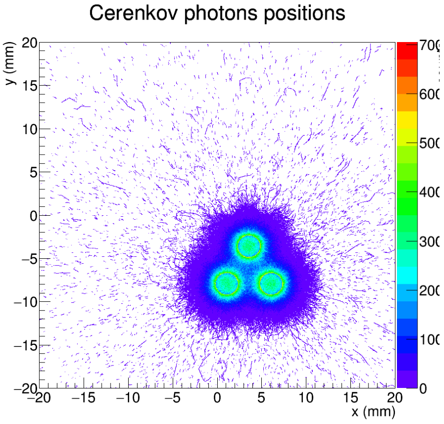


(a) Simulated image with solution refractive index equal to 1.20 and with unitary transmission.

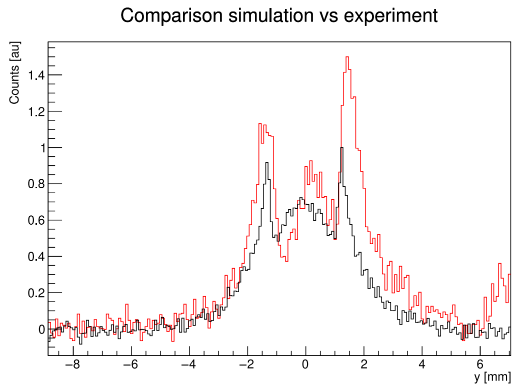


(b) Profiles of simulated image in figure 5.10a (black line) and of experimental image in figure 5.7b (red line).

Figure 5.10: Simulations of CLI with Ga-68 in PMMA phantoms, 2.5 mm diameter cylinders. The refraction index of the solution is modified

We will implement these two considerations in our simulation. Initially, we just try to see how the profile changes updating the simulation, in order:

- We reduced the refraction index value of the solution from the reference one for water (the solvent) reported in table 5.2 to 1.2. The resulting 2D image (figure 5.10a) has less counts on the inside of the cylinders because of the dependency of the Cerenkov effect on the refraction index, as stated in equation 1.28. The profile of a single hole is shown in figure 5.10b. More profiles across one cylinder are shown in figure A.4 on page 83 for acquisitions in which the refractive index of the solution varied in the range $[1.02, 1.30]$.

- We inserted a kind-of attenuation coefficient for the optical photons generated within the cylinder. From a practical point of view, for every Cerenkov photon that was generated, we extracted a random number $x$ from a box distribution in $[0, 1]$, then we compared it with a parameter $T$ in the same range.

$$\begin{cases} x < T & \text{the photon is counted} \\ x > T & \text{the photon is not counted} \end{cases} \tag{5.1}$$

  We tried several threshold values $T$, in figure 5.11a on the facing page we show the case with threshold equal to 0.5, meaning that 50 % of the Cerenkov photons generated within the cylinder were suppressed. The slice in figure 5.11b exhibits very sharp peaks right outside the cylinder volume. Figure A.5 on page 84 shows a more detailed analysis of the transmission coefficient: several profiles across one cylinder of 2.5 mm diameter are reported with transmission coefficient values in the range $[0, 1]$.

It looks like the two solutions lead to very similar images. Varying transmission coefficient, one changes the magnitude of the central peak (the Cerenkov photons generated in the solution) with a direct proportionality. Instead, varying the refraction index one obtain results that are less intuitive because of the inverse proportionality (see equation 3.10). Therefore we decide to set the refractive index of the solution as the one of water (1.34) and to vary only the transmission coefficient in order

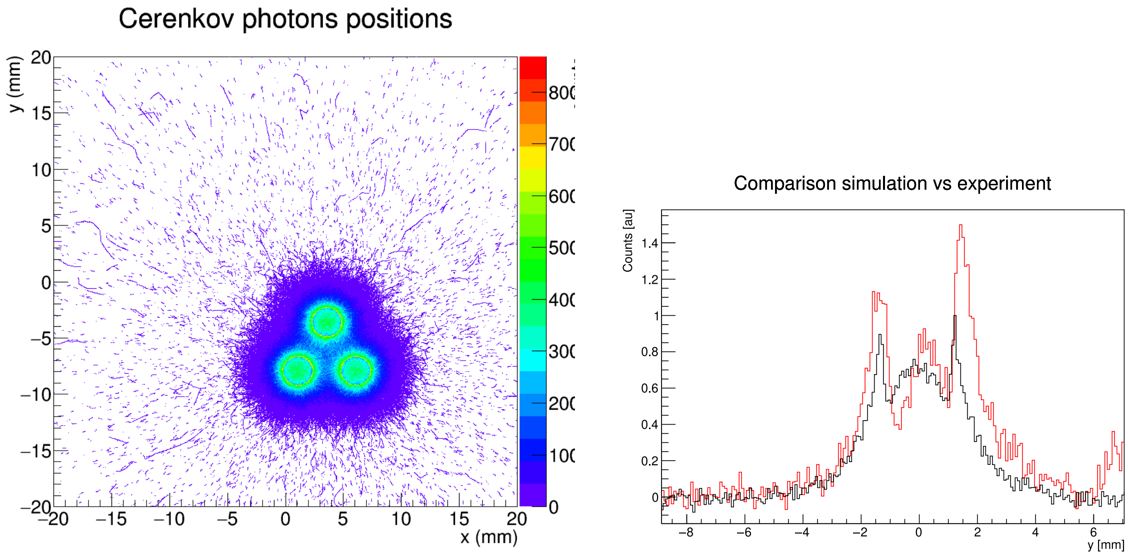


(a) Simulated image with transmission coefficient of optical photons equal to 0.5.

(b) Profiles of simulated image in figure 5.11a (black line) and of experimental image in figure 5.7b (red line).

Figure 5.11: Simulations of CLI with Ga-68 in PMMA phantoms, 2.5 mm diameter cylinders. The transmission coefficient of the solution is modified.

to match the experimental images.

We determine the width of the Gaussian blur by comparing the simulations smoothed with such filter at varying standard deviation with the experiment. In figure 5.12a we show the simulation without any processing and in figure 5.12b we show the same simulation with a Gaussian blur filter of standard deviation 0.1 mm. The simulation used in these comparisons has zero transmission coefficient for the solution. We chose this simulation because here the peaks at the interface solution-PMMA stand out and these peaks are intrinsically the sharpest structures of the images. The effect of the Gaussian blur filter is emphasized looking at these structures so we made them predominant by setting the transmission coefficient of the solution to zero thus killing the central peak. Starting by an image with such setting, we alternatively applied several Gaussian filters with different standard deviations. To do so, we used the procedure described in section 3.5. Figure A.6 on page 85 contains the images for all the Gaussian filters that we tried in order to match the experimental profile. The simulation that best matches the width of the lateral peaks is the one with $\sigma = 0.1$ mm (figure 5.12b).

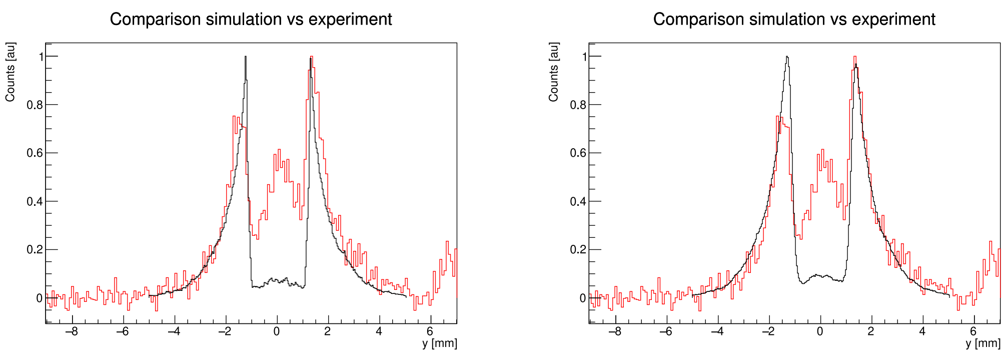


(a) Profile for no Gaussian smoothing.

(b) Profile for $\sigma = 0.1$ mm Gaussian smoothing.

Figure 5.12: Simulations (black line) of CLI with Ga-68 in PMMA phantoms, 2.5 mm diameter cylinders and transmission coefficient equal to 0. The profiles across one cylinder are superimposed with the correspondent profile of the experimental image in figure A.2b (red line).

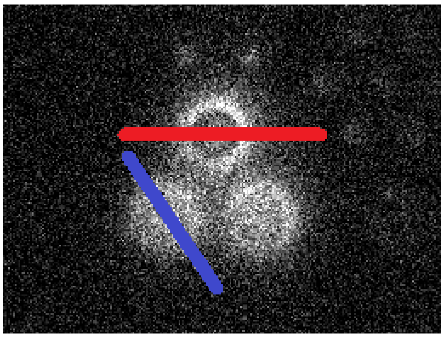

(a) Experimental 2D image from figure.

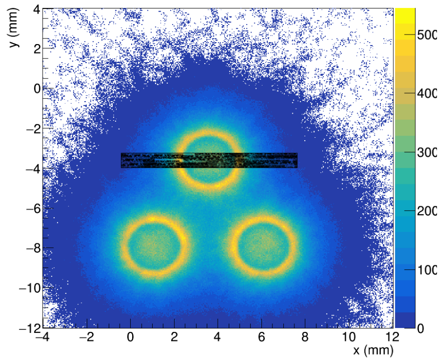


(b) Simulated 2D image.

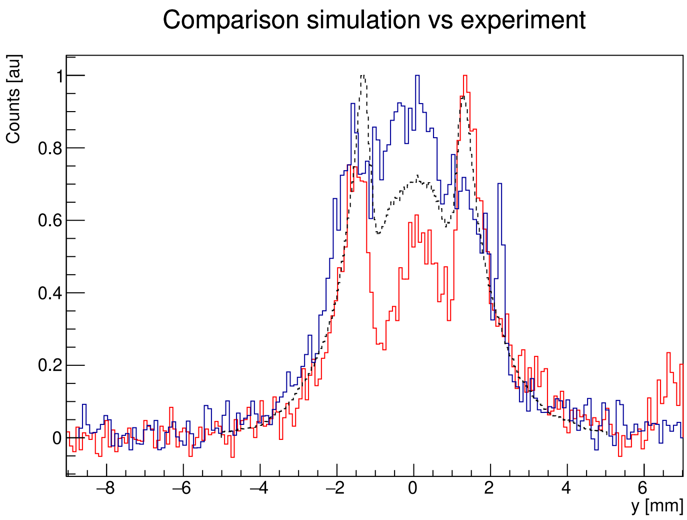


(c) Comparison between simulated and real images: the histograms are extracted from slices along a single cylinder. Both histograms are normalized to the correspondent maximum bin content.

Figure 5.13: Simulations of CLI with Ga-68 in PMMA phantoms, 2.5 mm diameter cylinders compared with the correspondent experimental images. The red and blue 1D histograms corresponds to the profiles along the red and blue slices in the experimental image. The dashed black 1D histogram corresponds to the profile along the black slice in the simulated image.

We determined the standard deviation of the Gaussian filter and this is a property of the optical system so all the images should share the same parameter. Therefore, we will apply this Gaussian filter with standard deviation 0.1 mm to all the 2D images.

We compare the simulations changing refractive index and transmission coefficient of the solution. The profile for the simulation with transmission coefficient 0.2 has the best match with the experimental profile. But this match is the best one only for this specific slice. In fact, for the other two slices the edges are not so predominant and a higher transmission coefficient gets a better agreement. Since we do not have reasons to prefer one profile to the others, we choose a transmission coefficient that is half-way in the agreement with every profile: $T = 0.4$. We plot its profile in figure 5.13 with a dashed black line. In the same plot the experimental profiles from figure 5.7b and from figure 5.7c are shown in solid red and blue lines respectively. We see that the central peak height of simulation with transmission coefficient 0.4 is right in between the two experimental profiles. Also the lateral decrease of the edges is close to the experimental trend.

We replicated the main features of the distributions resulting from the imaging process of a single cylinder. We would like to verify that the spatial resolution that we estimated looking at the 2D experimental images was correctly estimated.

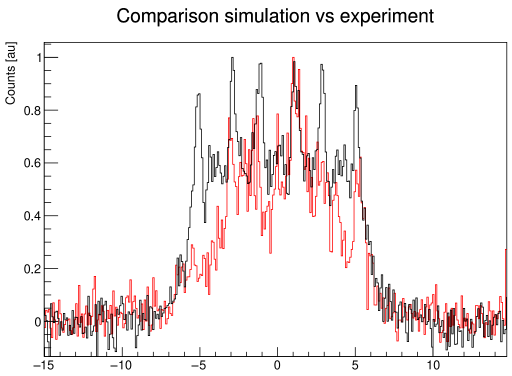


(a) Profile for 2.0 mm diameter.

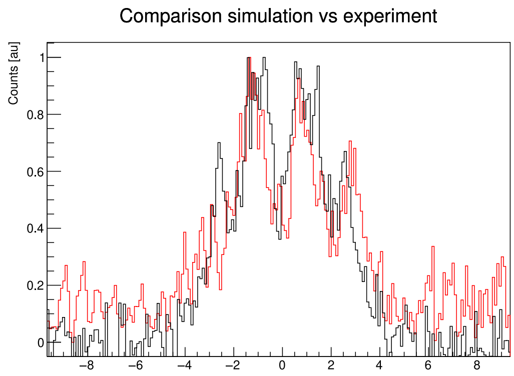


(b) Profile for 1.0 mm diameter.

Figure 5.14: Comparison between simulated profiles (black) and experimental profiles (red). For diameter 2.0 mm the distributions seem separated while for diameter 1.0 mm they seem not.

Let us consider a simulation of CLI with Ga-68 in PMMA phantom and namely a profile crossing the centres of two cylinders. Simulating enough events, it is possible to obtain distributions that are separated (according to the criterion stated earlier: drop in the 1D histogram means that they are resolved) even for the cylinders of diameter 0.7 mm. Looking at the experimental images (figure A.1h on page 80), it is straightforward that the rings of each cylinders mix up already at 1.0 mm diameter. Since the width of the simulated distributions properly matches the width of the experimental distributions, the issue is mainly related to the lack of noise in the simulation.

As already discussed in section 2.1, several sources of noise affect the final image. Indeed, the dark background of the experimental 2D images is full of bright pixels and the profiles are jagged curves. It is necessary to add this ingredient to the simulations and we do so as described in section 3.6.

In figure 5.14 we shows the simulation with noise for the acquisition with cylinder diameter 2.0 mm and 1.0 mm. The profiles are obtained with slices passing across three centres. The normalization of the curves is arbitrary, it is used to be able to plot both distributions in the same y-values range.

In figure 5.14b we clearly cannot resolve the cylinders, while in figure 5.14a we can. Indeed, in the case of diameter 1.5 mm we cannot be sure whether the cylinders are resolved or not. Concluding, for sure CLI with Ga-68 in PMMA phantom achieve a spatial resolution that allows the instrument to resolve objects in the range 1.0, 2.0 mm.

For HDPE material we could not assess experimentally the spatial resolution. Anyway, since the distribution of a single cylinder is even thinner than the one for PMMA, it is reasonable to assume that at least the same spatial resolution of PMMA material can be achieved.

### 5.3.2 Cerenkov Luminescence Imaging with Ga-68 in HDPE phantom

The CLI acquisition with Ga-68 in 2.5 mm of HDPE phantom is shown in figure 5.15b on the following page. Even if the solution was the same dyed one used in the PMMA phantoms, the dark circular centres does not appear inside HDPE phantoms. The same concept, difference attenuation in different materials, could explain this fact too: HDPE phantoms are opaque and thus the optical photons travelling in it undergo an even greater attenuation than the ones travelling in the dyed solution. Indeed, we planned the HDPE version of the phantom expecting that less Cerenkov photons originated in this material would have been collected.

With respect to CLI acquisition in PMMA, also the halo of signal around the cylinders is different. For PMMA it was more bright than the background and compact. Instead, for HDPE it looks less bright and spread out, it gradually goes to zero increasing the distance from the cylinders.

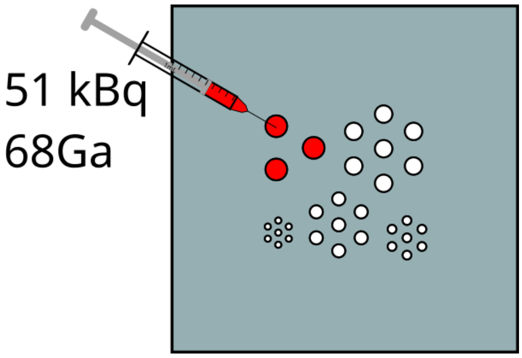


(a) Source layout with 2.5 mm diameter cylinders filled.

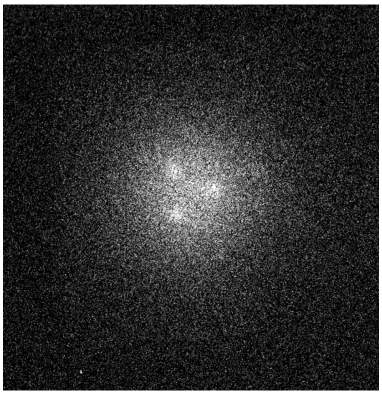

(b) Experimental image.

Figure 5.15: Experimental image: radionuclide is Ga-68, phantom is in HDPE and the cylinders have 2.5 mm diameter. The acquisition mode is CLI for 2 min.

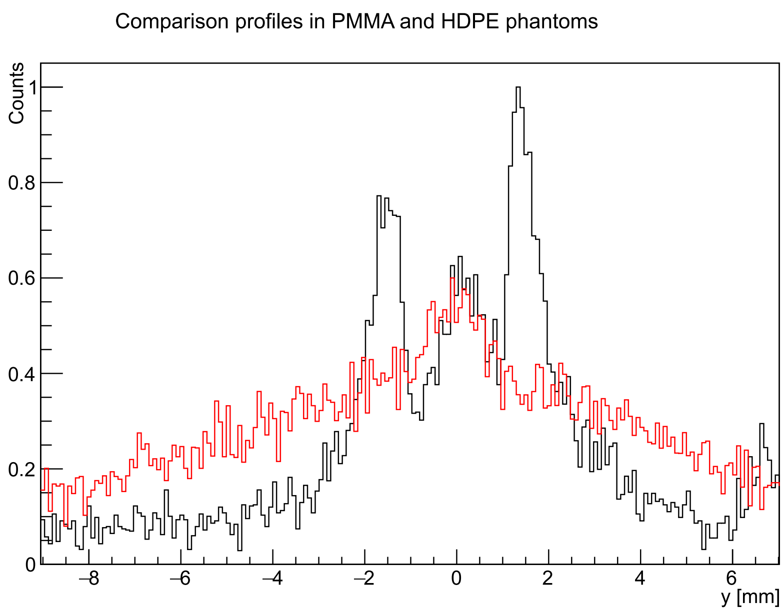


Figure 5.16: For CLI of Ga-68, here is a comparison between the case with PMMA phantom (black line, from figure 5.7b on page 49) and the case with HDPE phantom (red line, from figure 5.17 on the facing page).

In figure 5.16, we plot in the same canvas two slices: one across the right cylinder in CLI acquisition with PMMA phantom (2D image in figure A.2b) and another one across one cylinder in CLI acquisition with HDPE phantom (2D image in figure 5.17). Shifting the distribution and normalizing them so that their central peaks overlap, we can determine some similarities and differences:

- the central peak, that contains the counts of the Cerenkov photons generated within the solution, has similar width in both materials;
- the lateral peaks at the interface solution-HDPE are completely absent with respect to the case at the interface solution-PMMA;
- the signal distribution in HDPE has non-negligible tails far outside the cylinders while the PMMA distribution goes to zero within a shorter distance.

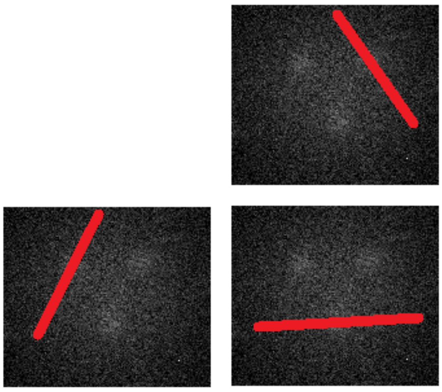

(a) Scheme of the slices positions.

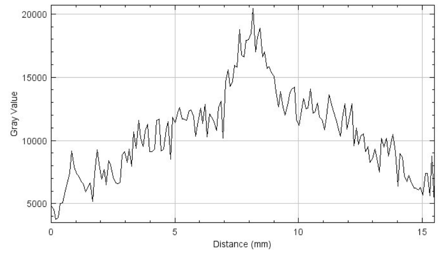


(b) Profile.

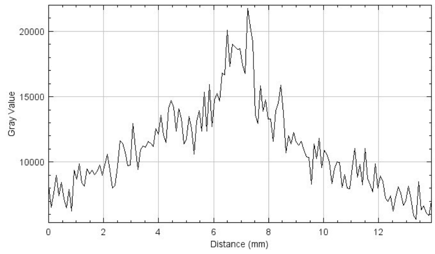


(c) Profile.

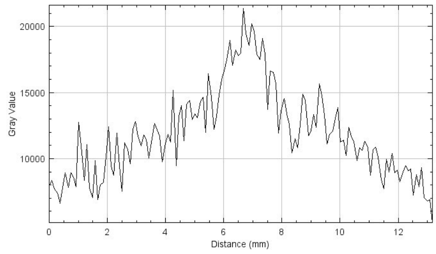


(d) Profile.

Figure 5.17: Profiles across the three cylinders of figure 5.15b with slice across single centers.

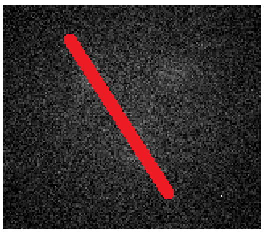

(a) Scheme of the slice position.

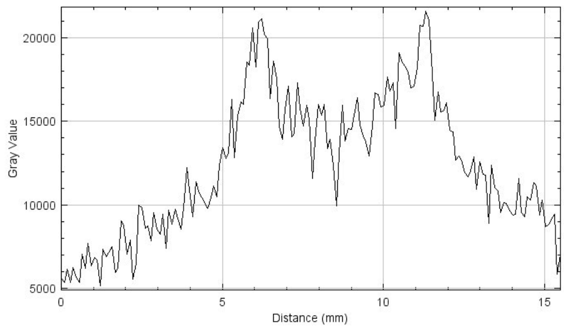


(b) Profile.

Figure 5.18: Profiles across the three cylinders of figure 5.15b with slice across pair of centers.

The profiles across different cylinders for the HDPE phantoms are more similar to each other with respect to the PMMA case. In figure 5.17 we show the the profiles for the acquisition with Ga-68 in 2.5 mm diameter cylinders of HPDE phantom. Since we were able to obtain similar profiles, we deduce that the heterogeneity between the cylinders in the case of PMMA phantom with 2.5 mm diameter did not occur during the imaging process. More likely, we did not fill evenly the cylinders so the source distributions were different from the start.

Analogously to the PMMA phantom, we plot in figure 5.18 the profiles across pairs of cylinders in the HDPE phantom. The peaks of the distributions of each cylinder are well separated by a drop of counts. Thus, the Xtreme can resolve 2.5 mm diameters also in HDPE material.

We would have further investigated the spatial resolution filling the smaller diameter cylinders too. We did not follow this plan because leakage of radioactive solution was unavoidable for smaller diameter cylinders, as we already discussed in subsection 4.1.3.

We determined the transmission coefficient of the solution and we will use it in the following simula-

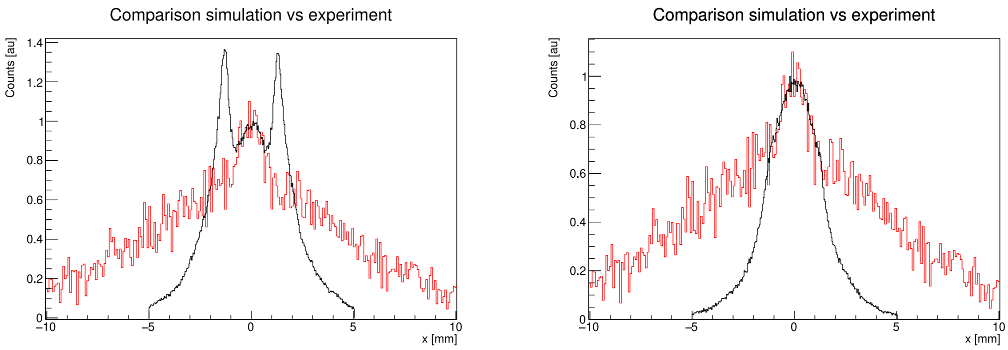


(a) Simulation 1.0 transmission for HDPE.

(b) Simulation 0.4 transmission for HDPE.

Figure 5.19: Simulations of CLI with Ga-68 in HDPE phantoms with different transmission coefficients for HDPE material. The solution has 0.4 transmission coefficient and a Gaussian filter with $\sigma = 0.1$ mm is applied. The simulated profiles (black) are superimposed on the experimental profile (red).

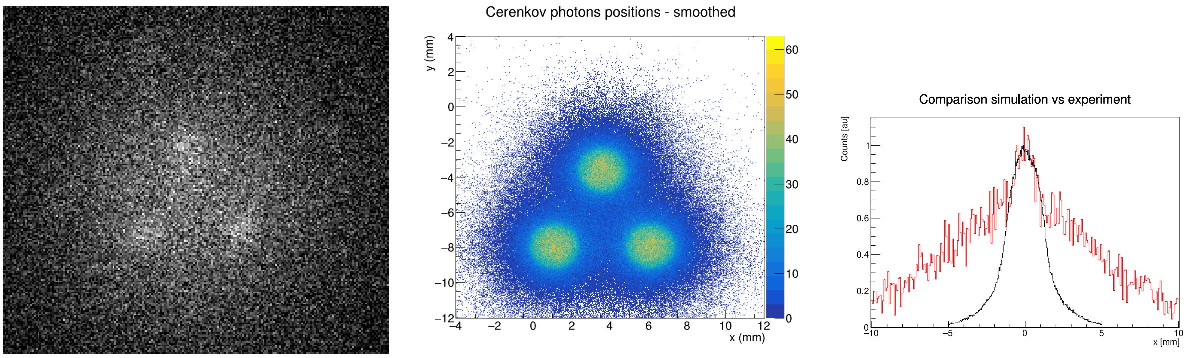


(a) Experimental 2D image.

(b) Simulated 2D image.

(c) Comparison between simulated and real images: the histograms are extracted from slices along a single cylinder. Both histograms are normalized to the correspondent maximum bin content.

Figure 5.20: Simulations of CLI with Ga-68 in HDPE phantoms, 2.5 mm diameter cylinders compared with the correspondent experimental image. The transmission coefficient for HDPE material is 0.3.

tions. We simulate CLI with Ga-68 in HDPE phantom. Keeping constant all the other parameters, we change the transmission coefficient of the phantom material in the same way as we did for the radioactive solution. Some example of these simulations are shown in figure 5.19 while all the ones produced are shown in figure 5.19. The experimental image (figure) does not show any lateral peak. We set the superior limit for the transmission coefficient in HDPE by looking for this feature in the simulations: for $T < 0.4$ no lateral peaks are visible. The real value will probably belong to the range $[0, 0.4]$.

There is an issue with simulations in HDPE phantom. As one can see in figure 5.20, independently by the transmission coefficient used for HDPE material, there is always a non-negligible tail of counts further from the source in the experimental image that we are unable to reproduce in the simulated images.

Further investigations may be able to unveil the physics underpinning this features. Regarding the spatial resolution achievable with HDPE material, in principle it could be better than with PMMA since the tails of the distribution outside the cylinders are not present. On the other hand no experimental data is available yet below 2.5 mm so it is still premature to make such guess.

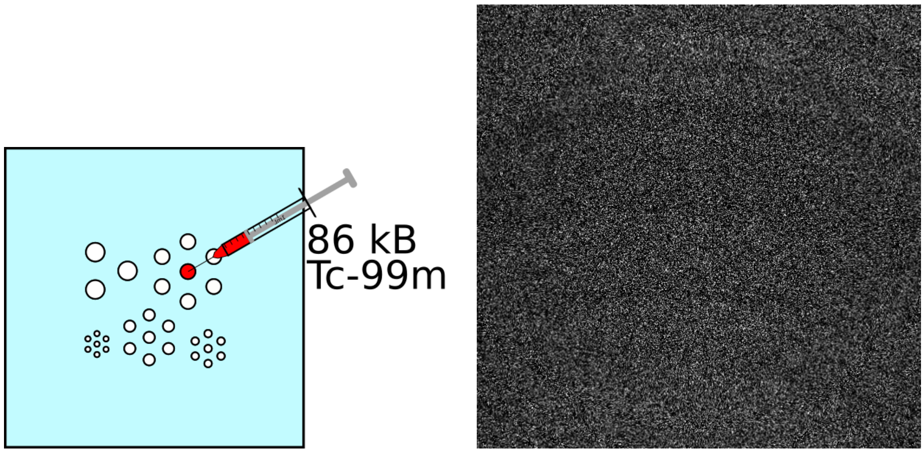


(a) 2.0 mm diameter scheme. (b) 2.0 mm diameter image.

Figure 5.21: Experimental images: source is Tc-99m, phantom is in HDPE and the acquisition mode is CLI. Acquisition time is 10 s.

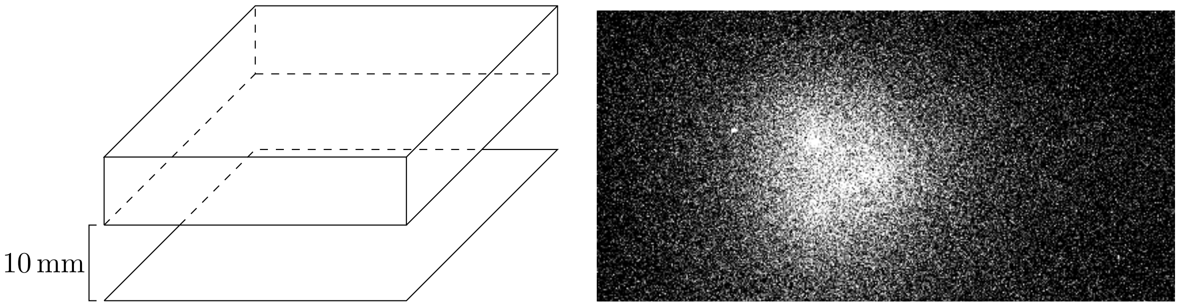


(a) Scheme at 10 mm distance phantom-support. (b) Experimental image at 10 mm distance. Acquisition time is 6 min.

Figure 5.22: CLI images with Ga-68 in 2.5 mm diameter cylinders of HDPE phantom with 10 mm distance between phantom and floor.

### 5.3.3 Cerenkov Luminescence Imaging with Tc-99m

For Tc-99m CLI was no different from background images (figure 5.21). This was expected since the electrons emitted in the decay are few and with energy smaller than the threshold one for Cerenkov effect in water.

### 5.3.4 Cerenkov Luminescence Imaging depth study

In figure 5.22 we can see the acquisition for Ga-68 in 2.5 mm diameter cylinders of HDPE phantom with 10 mm distance with respect to the sample support. The distance is set using the wedges (figure 4.4a). The contrast of the image is very low so it is difficult to identify the three cylinders. On the other hand, the spatial distribution of the cylinders seems to not have worsened.

Images for distances at also 5 mm and 15 mm can be found in figure A.8 on page 87. The contrast of the image decreases increasing the distance, at 20 mm we are almost unable to tell the three circles from the background. Instead, the spatial resolution itself does not seem to deteriorate. To some extent, we can say that the spatial resolution is weakly affected by the distance.

The simulation we prepared does not support any variation in the phantom-support distance. That occurs because Cerenkov effect takes place along the track of the generated positrons. For the generated photons only the xy-coordinates are relevant.

Therefore, in some sense, experiment and simulation agree on the fact that the phantom-support distance has little effect on the spatial resolution of CLI acquisitions.

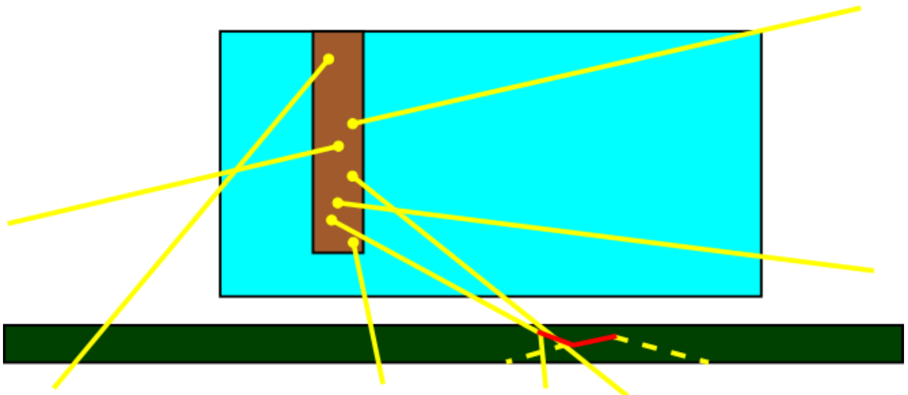

Figure 5.23: Scheme of the scintillation mechanism with Tc-99m in Roma phantom. Yellow solid lines are gamma-rays, yellow dashed lines are optical photons, red solid lines are electrons. The brown box on bottom represents the scintillator screen.

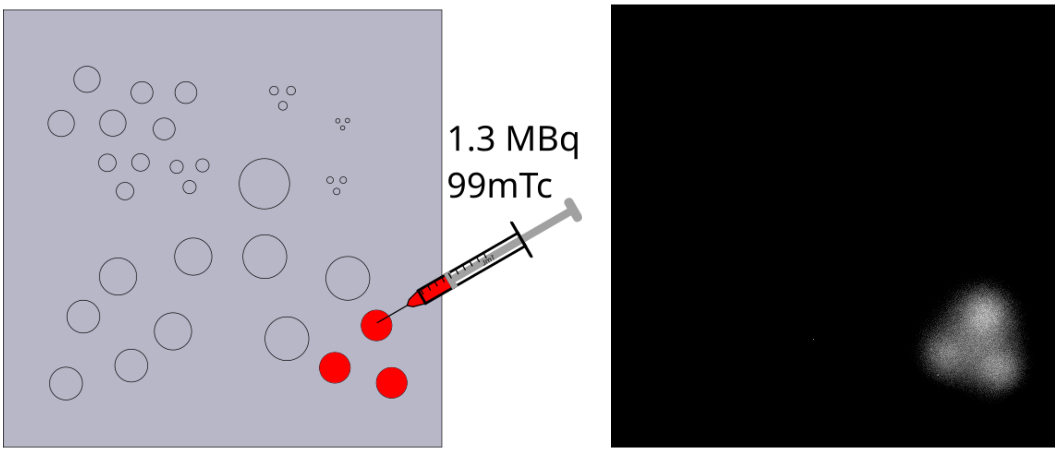


(a) Scheme.

(b) Image.

Figure 5.24: Experimental images: source is Tc-99m and acquisition mode is DRI. Diameter of filled cylinders is 7 mm. Acquisition time is 10 s.

## 5.4 Data Analysis for Direct Radioisotopic Imaging

### 5.4.1 Direct Radioisotopic Imaging with Tc-99m

When Roma phantom is filled with the radioactive solution containing Tc-99m, scintillation is triggered by the gamma-rays emitted in the decay of the radionuclide (see equation 1.22). Figure 5.23 represents the scintillation mechanism in this setup.

The first DRI experimental image that we report is with Tc-99m in 7.0 mm diameter cylinders of Roma phantom, in figure 5.24. The cylinders seems resolved and the intensity of each distribution seems homogeneous.

Indeed, in figure 5.25 on the next page we plot the profile across two cylinders of the 2D experimental image in figure 5.24b. As expected, we can distinguish the two peaks of each cylinder of 7 mm diameter. In this profile the tails of the signal due to the gamma-rays scintillation are not visible and the bins count uniformly zero. This behavior is due to adjustments of the minimum value for the z-axis (counts): we increased the minimum value so that the cylinders signals are more easily distinguishable. This operation is like imposing a cutoff in the z-axis that discards the lower part of the profile.

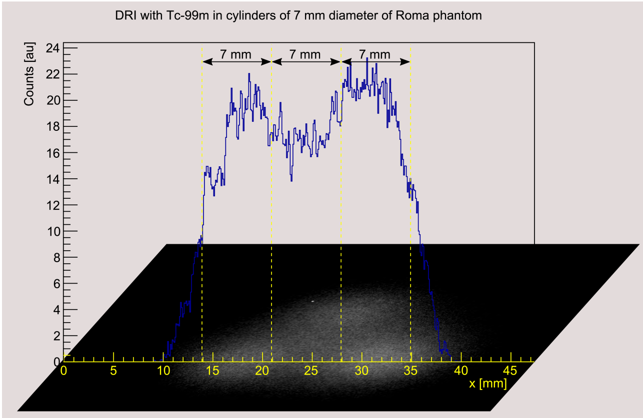


Figure 5.25: Profile across two centres for DRI with Tc-99m in Roma phantom and 7 mm cylinder diameter.

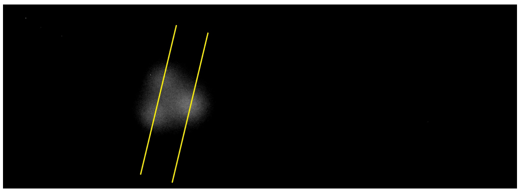

(a) 7 mm diameters image with slices superimposed.

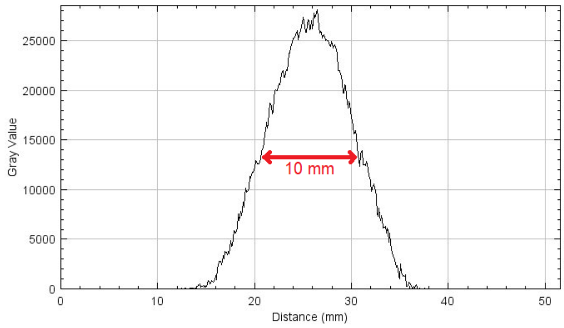


(b) 7 mm diameters image profile across one cylinder.

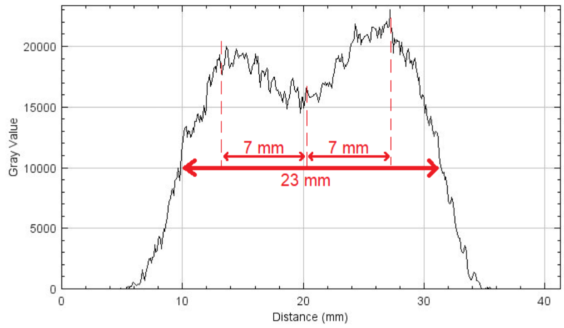


(c) 7 mm diameters image profile across two cylinders.

Figure 5.26: Experimental images: source is Tc-99m, phantom is in Roma and the acquisition mode is DRI.

We take some slices of the image in figure 5.24b. The slices are taken along lines passing through the centers of the circles, as represented in figure 5.26a. The 1-D histograms obtained by such lines are shown in figure 5.26b and in figure 5.26c. In the same fashion, we obtained other four 1-D histograms using lines passing through the other centers. We analyse these slices estimating the Full Width at Half Maximum (FWHM). On average, the histograms passing through a single cylinder have FWHM $\sim 10$ mm. The FWHM of the radionuclide object can be identified with the diameter of the cylinders (denoted $\Phi$ in equation 5.2). It means that from the radionuclide object to the real image the FWHM gets about 3 mm larger.

$$\text{FWHM} = \Phi + \Delta \tag{5.2}$$

Therefore, we expect the FWHM of the histograms passing through two cylinders to be approximately equal to the FWHM of the single-cylinder histograms plus two times the diameter of the cylinders, because such is the distance that separates the two centers of the cylinders.

$$\text{FWHM} = 3\Phi + \Delta \tag{5.3}$$

Indeed, for the two-cylinders slices we find a FWHM $\sim 23$ mm.

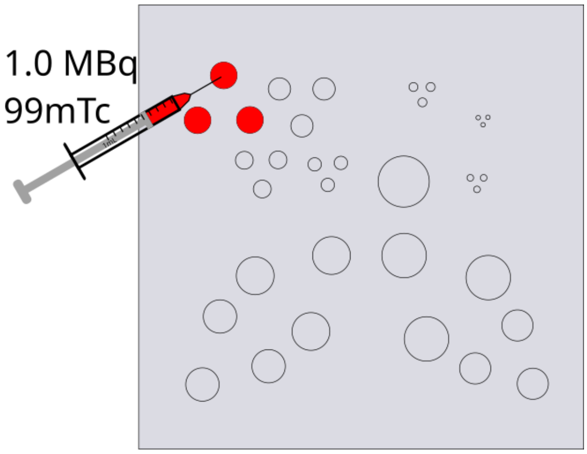


(a) Scheme.

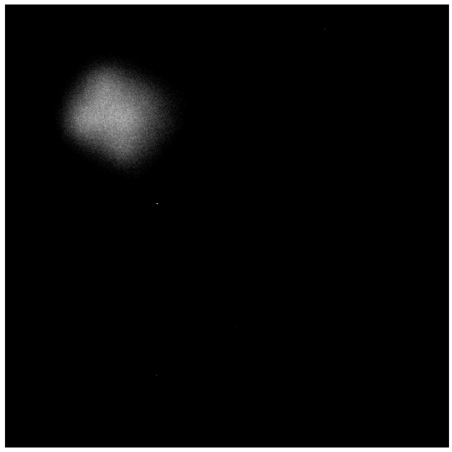

(b) Image.

Figure 5.27: Experimental images: source is Tc-99m and the acquisition mode is DRI. The diameter of the cylinders is 6 mm.

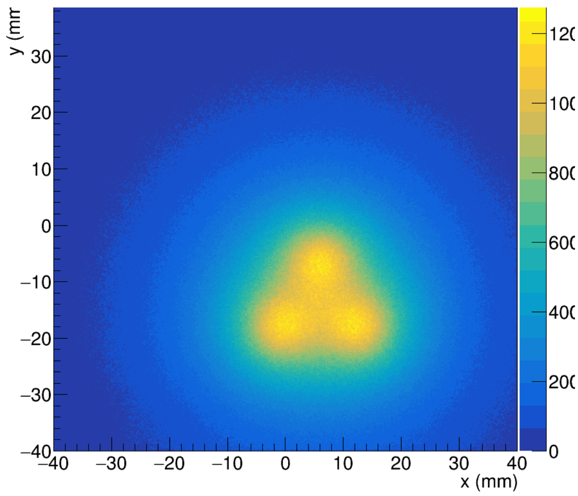


(a) 7 mm diameters simulated image.

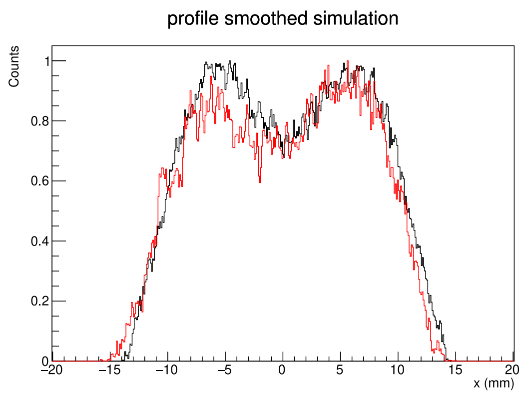


(b) 7 mm diameters image profile across two cylinders.

Figure 5.28: Simulated images: source is Tc-99m, phantom is in Roma, diameter is 7 mm and the acquisition mode is DRI. A cutoff on counts is set for the profile.

The next DRI experimental image that we analyse is with Tc-99m in 6.0 mm diameter cylinders of Roma phantom, in figure 5.27. The circles of different cylinders seems overlapped in a unique bright cloud. Thus, we say that these cylinders are not resolved.

In figure 5.28 we show the simulation for DRI acquisition of Tc-99m in 7 mm diameter cylinders of Roma phantom. The cylinders are resolved as in the experimental image in figure 5.24b.

Since in the experimental image a minimum value for the intensity of the pixels was set, we need to apply an analogous cutoff also in the simulated image. In order to match the experimental profiles in figure 5.26, we removed all the counts below a threshold equal to half times the maximum counts in the histogram. More explicitly, considering a bin $i$ with bin content $h_i$ and a threshold value $h_T$, we created a new histogram with bin contents

$$\begin{cases} 0 & \text{if} \quad h_i < h_T \\ h_i - h_T & \text{if} \quad h_i \geq h_T \end{cases} \tag{5.4}$$

As we can see in figure 5.28b, the simulation with the proper cutoff (equal to half of the maximum) is able to follow the experimental curve.

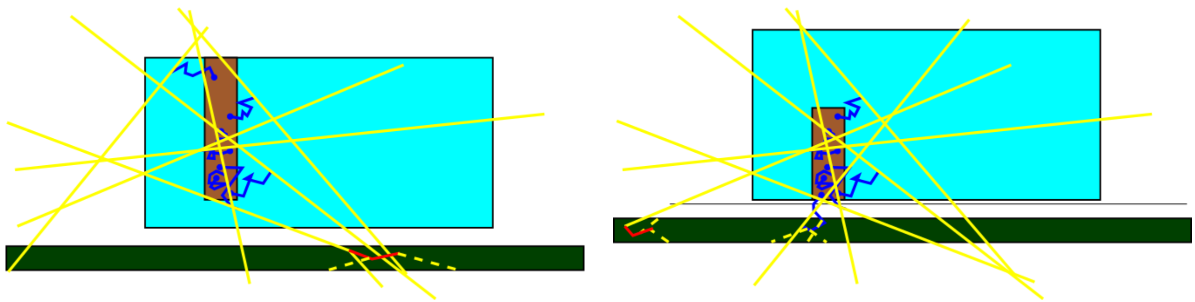

(a) Scintillation scheme in Roma phantom (see figure 4.3a).

(b) Scintillation scheme in PMMA phantom (see figure 4.2a).

Figure 5.29: Scheme of the scintillation mechanism with Ga-68 in Roma and PMMA phantoms. Yellow solid lines are gamma-rays, yellow dashed lines are optical photons, blue solid lines are positrons and red solid lines are electrons. The brown box on bottom represents the scintillator screen and the thin line below PMMA phantom represents the plastic wrap. Differently from Roma phantom, once filled PMMA phantom is turned upside down.

### 5.4.2 Direct Radioisotopic Imaging with Ga-68

During Ga-68 decay (and the subsequent positron annihilation) two types of radiation that can generate scintillation photons in DRI are emitted:

**positrons** They are charged particles with average energy below 1 MeV (see table 4.4). They move in materials such as water following non-straight trajectories for lengths of the order of 1 mm.

**gamma-rays** These photons move straight in materials until they interact. They are highly penetrating so the thin phosphor screens will let pass the greatest part of them unaffected.

Due to these features, positrons tend to move away from the original radionuclide much less than gamma-rays. Consequently, the spatial resolution of images obtained with positron scintillation photons will be much better than the one obtained with gamma-rays scintillation photons.

Moreover, positrons are more prone to release energy in the material while gamma-rays overcome frequently the thin screen without interacting. So, when the flux of positrons toward the surface is about the same of gamma-rays, the number of visible photons generated by positron scintillation will be predominant with respect to the number generated by gamma-ray scintillation.

One may think that there is no point in discussing these differences since during the decay of a Ga-68 radionuclide both radiations are produced. On the other hand, in our experimental setup we have the possibility to select partially their contribution to the final scintillation photons distribution. In fact, as depicted in figure 5.29:

- Roma phantom has a thick ($\sim 1$ mm) PMMA basement that prevents a huge part of the emitted positrons from reaching the phosphor screen;
- PMMA phantom has only a thin ($\sim 10\,\mu$m) film of plastic wrap that hardly have any effect in terms of positron stopping.

Consequently, as we will see in the experimental images, in Roma phantom gamma-ray based scintillation is predominant while in PMMA phantom positron based scintillation is predominant. In both phantoms there is always a coexistence of both sources of scintillation photons.

In order to simulate the experimental setup, we placed a 1 mm thick layer of scintillator material just below the phantom. This layer simulates the scintillator screen: when ionizing radiation releases its energy within the layer scintillation optical photons are generated. The information of these photons is saved, in particular the spatial coordinates of the points. The thickness may be larger than the real one but changing the thickness within a small range does not affect the spatial resolution in the

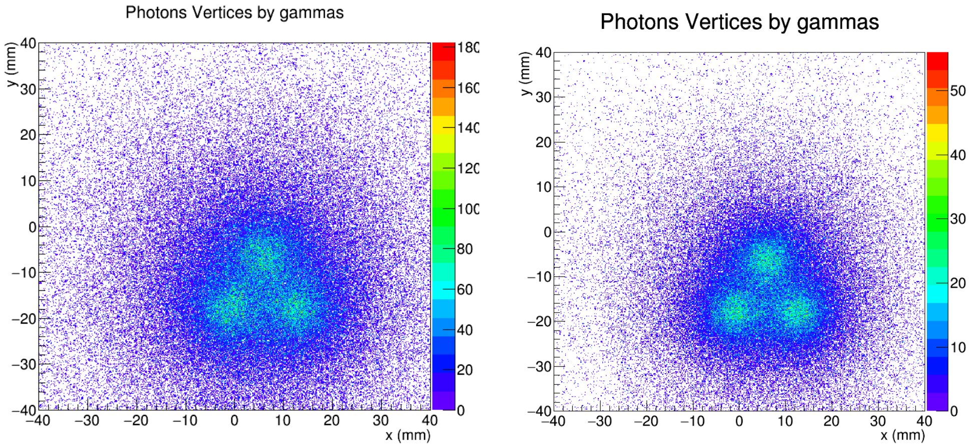


(a) Simulated 2D image for Ga-68.

(b) Simulated 2D image for Tc-99m.

Figure 5.30: Simulations of gamma-rays-induced DRI with Ga-68 and Tc-99m. 7 mm diameter cylinders of Roma phantom are filled.

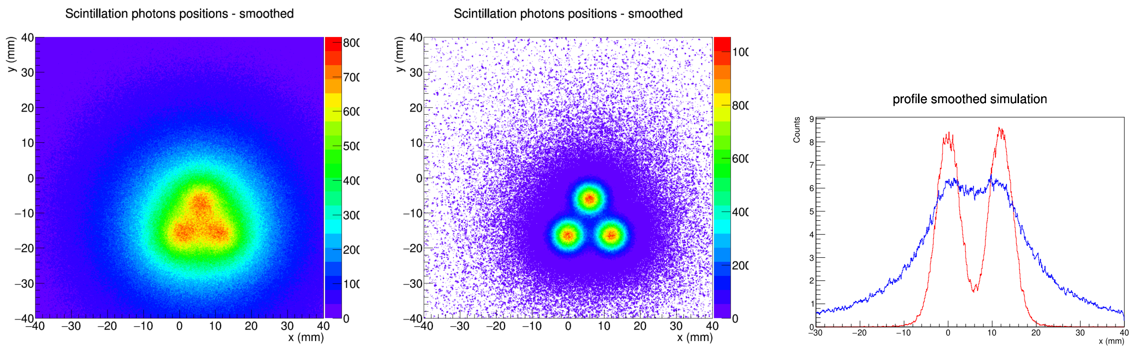


(a) Simulation of gamma-induced scintillation for DRI acquisition with Geant4 for Ga-68.

(b) Simulation of positron-induced scintillation for DRI acquisition with Geant4 for Ga-68.

(c) Profiles across two cylinders for both gamma-induced (blue) and positron-induced (red) scintillation.

Figure 5.31: Simulation of scintillation for DRI acquisition with Geant4 for Ga-68 with comparison between gamma-induced and positron-induced scintillation.

simulation. The output of these simulations can be summarized in 2D histograms in which the xy coordinates of the points where the optical photons were generated are displayed, as for CLI.

At first we assumed that only gamma-ray radiation could reach the scintillator, therefore we set up the simulations neglecting other type of ionizing radiations. With this setup, comparing the simulation of DRI for Ga-68 (figure 5.30a) and Tc-99m (figure 5.30b), one can see that the latter generates images that are slightly more detailed. We expected this hierarchy in the spatial resolution because for Tc-99m the gamma-ray object coincide with the solution volume while for Ga-68 it comprehends a halo that surrounds the solution volume.

Conversely, in the experiment we obtained Ga-68 DRI images where cylinders of diameter as small as 5 mm were resolved while Tc-99m images with cylinders diameter 6 mm were already unresolved.

We perform a simulation with Ga-68 in which we generate scintillation photons within a setup similar to the experimental situation and in which we can check if the primary particle is a positron or a gamma-ray. The results of this simulation are shown in figure 5.31. As we can see, the DRI due to positrons only (figure 5.31b) has a better spatial resolution than the DRI due to gamma-rays only (figure 5.31a).

Evidently, for Ga-68 the gamma-rays alone cannot describe the scintillation properties in the phosphor

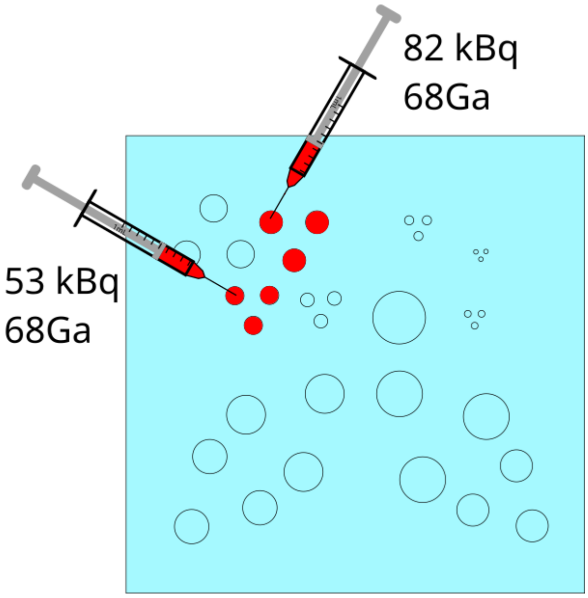


(a) 4 mm and 5 mm diameters scheme.

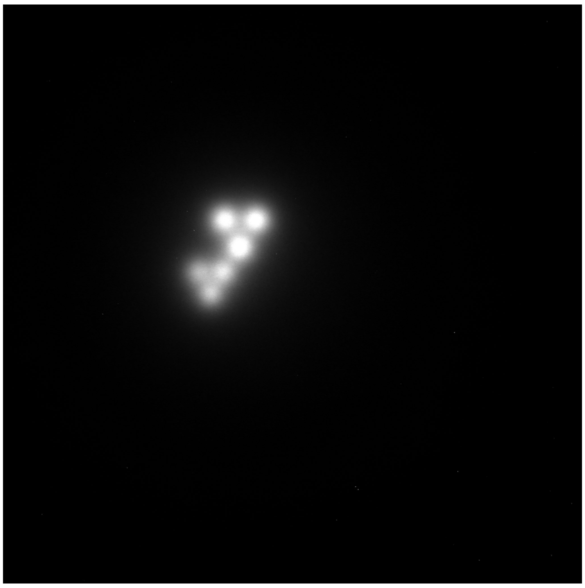

(b) 4 mm and 5 mm diameters image.

Figure 5.32: Experimental images: source is Ga-68, phantom is Roma and the acquisition mode is DRI.

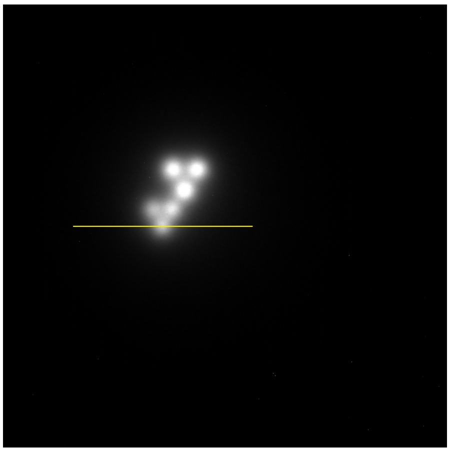

(a) 4 mm diameters and 5 mm diameters image with slices superimposed.

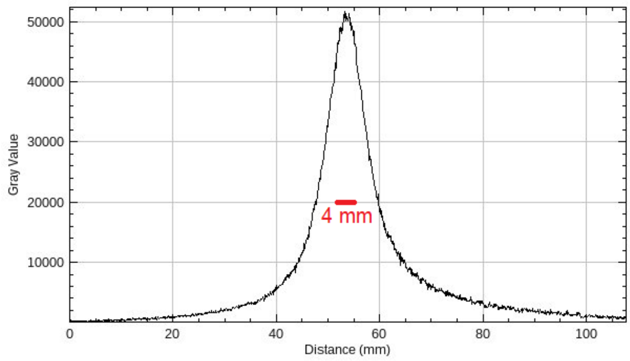


(b) Slice across the left cylinder of 4 mm diameter in figure 5.33a.

Figure 5.33: Experimental images: source is Ga-68, phantom is in Roma and the acquisition mode is DRI.

screen. We have to upgrade our simulation tracking also the positrons together with the gamma-rays.

In figure 5.32 we show the experimental image we mentioned above. It is a DRI acquisition with Ga-68 in Roma phantom. The diameters of the cylinders filled are 4 mm and 5 mm. All the cylinders in the image are distinguishable.

The profile across one cylinder of 4 mm diameter is plot in figure 5.33. The shape of the distribution is bell-like, there is no visible interface effect. We can note that the curve is more smooth than the one for CLI, probably because the statistics is bigger. Small but well defined tails of signal are present even far away from the cylinder. The FWHM is $\sim 10$ mm.

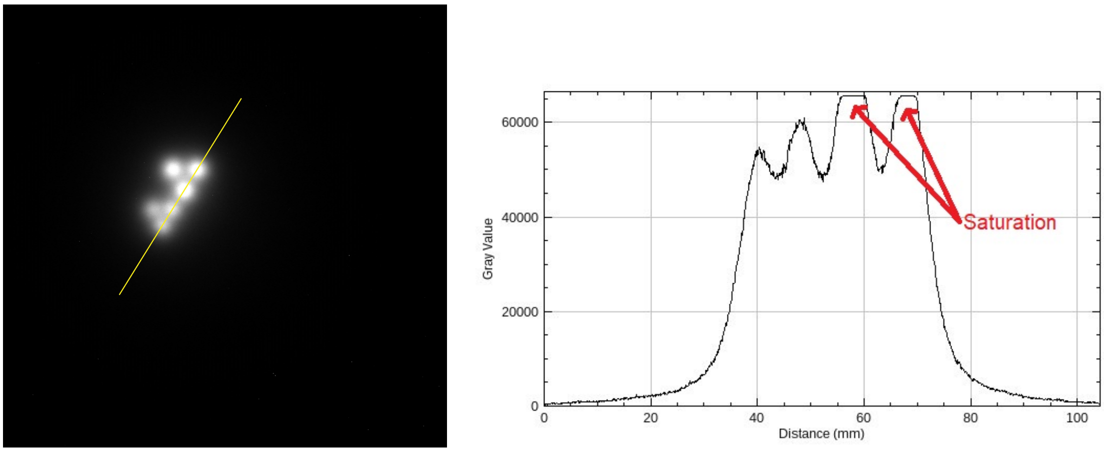


(a) 4 mm diameters and 5 mm diameters image with slices superimposed.

(b) Slice across the four aligned cylinders in figure 5.34a.

Figure 5.34: Experimental images: source is Ga-68, phantom is in Roma and the acquisition mode is DRI.

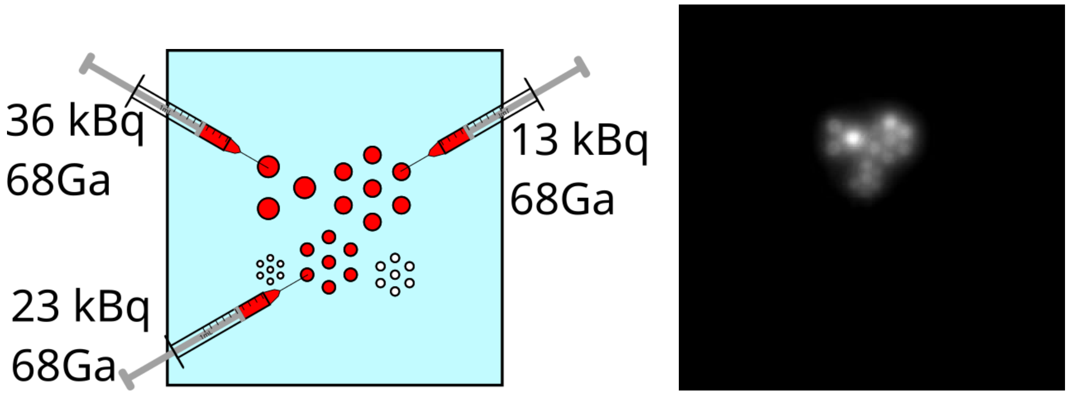


(a) 1.5 mm, 2 mm and 2.5 mm diameters scheme.

(b) 1.5 mm, 2 mm and 2.5 mm diameters image.

Figure 5.35: Experimental images: source is Ga-68, phantom is PMMA and the acquisition mode is DRI.

The profile across four cylinders (two of 4 mm diameter and two of 5 mm diameter) is plot in figure 5.34. The first thing that draws our attention is the flat top of the distributions of the cylinders of 5 mm diameter. Since we expected the peak of a bell shaped curve, such flat top indicates that saturation was reached for these pixels. Saturation is an issue in the measurement of the FWHM because we do not know what is the real maximum nor, consequently, the real half maximum at which the width of the distribution should be measured.

Secondly, we see that the peaks of the four distributions are well separated by drops of counts. Therefore, the 1D histograms clearly confirms the fact that these cylinders are resolved. So, DRI with Ga-68 in Roma phantom achieve a resolution of $\sim 4$ mm.

We look at the DRI acquisition with Ga-68 in PMMA phantom in figure 5.35. The diameters of the cylinders filled are 2.5 mm, 2.0 mm and 1.5 mm. The cylinders of diameter 2.5 mm and 2.0 mm are surely distinguishable. Instead, one may not be sure about the resolution of the cylinder of 1.5 mm diameter.

With PMMA phantom we have resolved cylinders of smaller diameter than the ones resolvable with Roma phantom. As already mentioned, this improvement is the effect of having less material between the source and the scintillator.

Some circles are more bright than others and, again, this fact is probably due to the uneven filling of the cylinders.

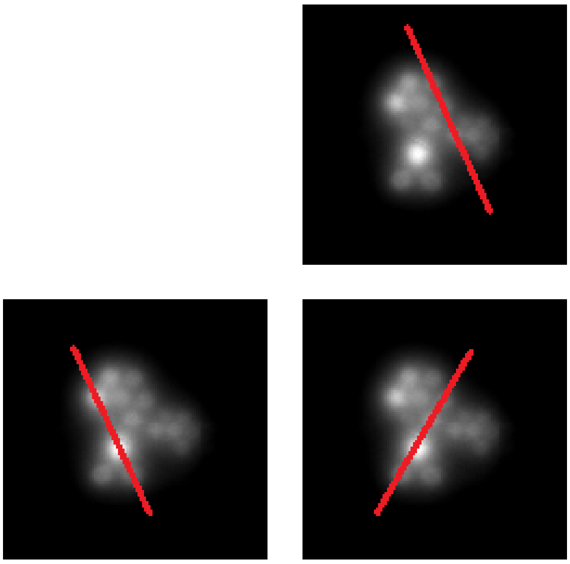

(a) Scheme of the slices positions.

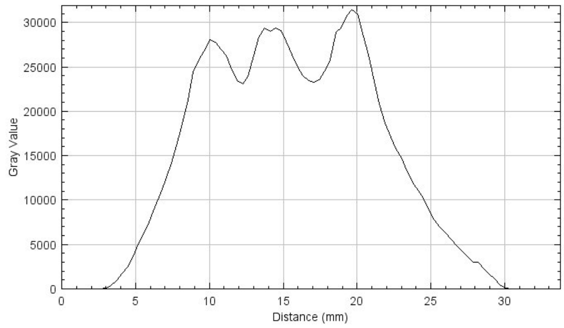


(b) Profile across two centres of 2.0 mm diameter and two centres of 1.5 mm diameter.

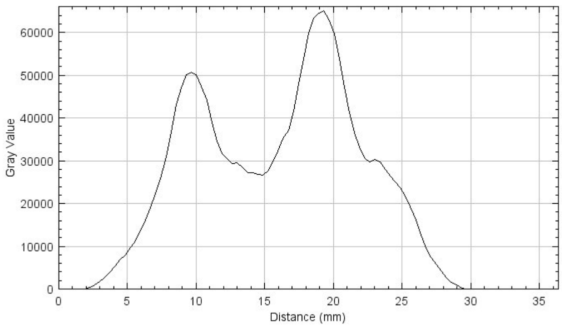


(c) Profile across two centres of 2.0 mm diameter and two centres of 2.5 mm diameter.

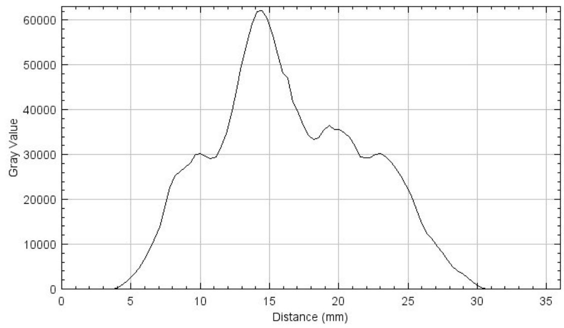


(d) Profile across two centres of 2.0 mm diameter and two centres of 2.5 mm diameter.

Figure 5.36: Profiles across the three groups of cylinders of figure 5.35b with slice across double pairs of centers.

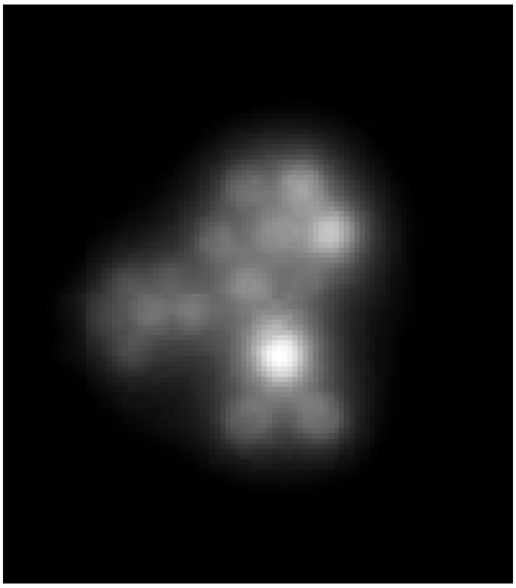

(a) Experiment.

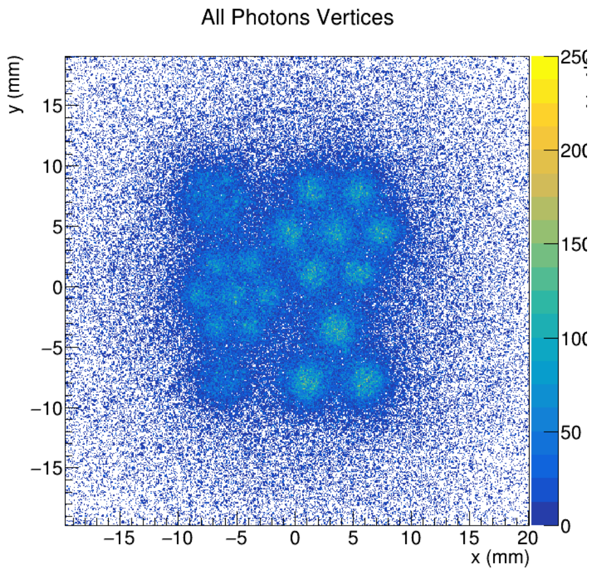


(b) Simulation.

Figure 5.37: Comparison between experiment (left) and simulation (right) of Ga-68 DRI acquisitions in PMMA phantom with varying phantom-scintillator distance.

We look to some profiles acquired slicing the 2D image in figure 5.35b on page 66. The separation of the curves is not very defined but the profile in figure 5.36b clearly shows that the distributions of the cylinders of diameter 2.0 mm are separated.

For 1.5 mm diameter, maybe a more accurate filling would have contributed in separating the cylinders signal. The statistics is already good since the curves are not jagged so increasing the acquisition time probably will not result in improving the spatial resolution.

A key parameter in the simulations for DRI acquisitions is the distance between the phantom and the scintillator screen. We could not directly measure this distance in the experimental site so we are going to repeat the simulation varying this distance within a reasonable range and looking for the best match to the experimental image (figure 5.35b). We choose the following points for the distance: 0 mm, 0.25 mm, 0.5 mm. The three simulated images are shown in figure A.9 on page 88. We propose a visual comparison with the best matching simulated image in figure 5.37, that has a distance of 0.25 mm. The similarity regarding the diameters that are resolved and those who are not suggests that 0.25 mm is the most suitable offset to reproduce the experimental spatial resolution.

With an analogous study we find that an offset of 2 mm describes the simulations in which Roma phantom was used. One has to consider that this phantom has a layer of PMMA material of about 1 mm thickness at the bottom of the holes. For Tc-99m, this layer adds a distance between the radionuclide solution and the scintillator degrading the spatial resolution as described in section 5.4.4. Moreover, for Ga-68, on top of the increased distance effect, there is also a detriment of the spatial resolution due to the scattering and absorption of the positrons in the material.

This last effect implies that increasing distance the relative contribution of positrons and gamma-rays to the scintillation phenomenon is modified in favor of the latter. Therefore, the spatial resolution will get closer to the one simulated initially without the positrons (figure 5.30a).

In the case of PMMA phantom, the only plastic material between the cylinders and the scintillator is a 10 µm foil of cellophane. This layer is enough thin to be negligible in the resulting resolution.

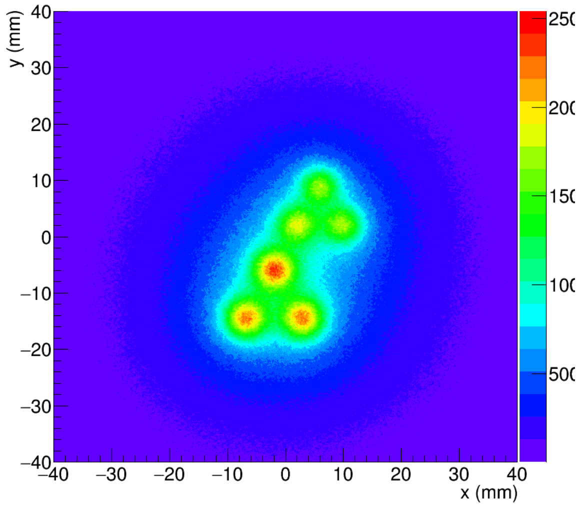


(a) Simulated DRI image for Ga-68 in 4 mm and 5 mm diameter cylinders of Roma phantom. The basement of the phantom is 1 mm and the offset distance is 2 mm.

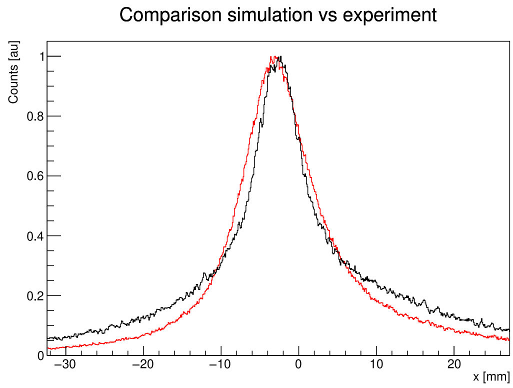


(b) Comparison of the experimental profile (red) with the simulated profile (black) across one cylinder.

Figure 5.38: Simulations of Ga-68 DRI acquisitions with Roma phantom. The PMMA layer on the bottom of the phantom is set to 2 mm thickness.

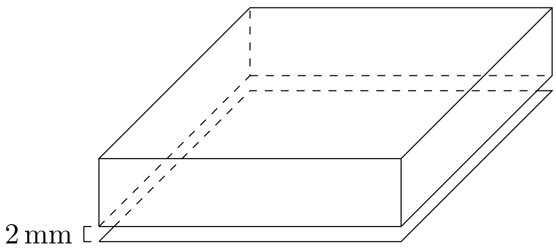


(a) Scheme at 2 mm distance.

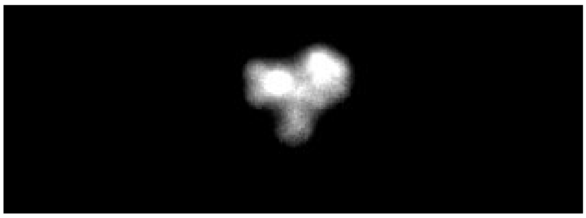

(b) Experimental image at 2 mm distance.

Figure 5.39: Images with Ga-68 in 1.5 mm, 2.0 mm, 2.5 mm diameter cylinders with 2 mm distance between phantom and floor.

We tried different combinations of distance offsets and basement thicknesses in several simulations. For example, we show in figure 5.38 there is the simulated image with Ga-68 in a Roma phantom with basement thickness of 1 mm and air gap offset distance of 2 mm. The simulated 2D image is side by side to a profile plot obtained slicing across one cylinder. In this plot we superimpose the profile of the simulated distributions (black line) with the profile of the experimental images (red line). We see that the combination of parameters used is able to describe the experiment. More simulations can be found in figure A.10 on page 89 with basement thickness between 1 mm and 2 mm thick and the offset distance between 0.25 mm and 3 mm.

### 5.4.3 Study of Direct Radioisotopic Imaging with Ga-68 at different depths

In figure 5.39 we can see the experimental acquisition for DRI with Ga-68 in PMMA phantom that is distant 2 mm from the sample support. The distance is set using the PLA cap (figure 4.5). The spatial resolution is readily worsened even if the distance is only about 2 mm. With respect to CLI modality, DRI spatial resolution seems much more sensitive to the distance between the phantom and sample support. As already mentioned, this distance can also be interpreted as the distance between the phantom and the phosphor screen, therefore, a wider gap means both:

- larger spread of the gamma-rays before being converted into optical photons;
- fewer positrons that are able to reach the scintillator screen.

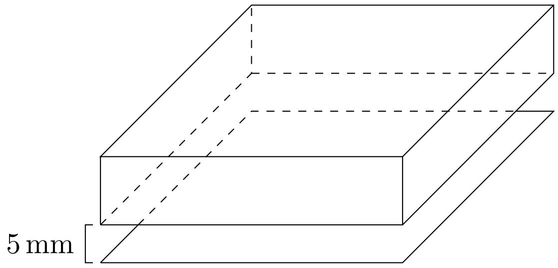


(a) Scheme at 5 mm distance.

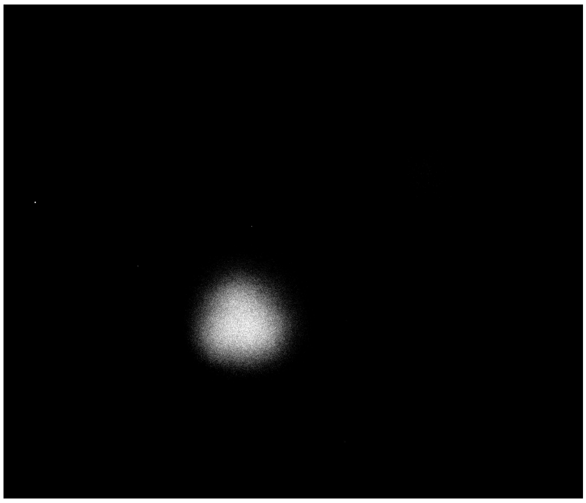

(b) Experimental image at 5 mm distance.

Figure 5.40: Images with Tc-99m in 7 mm diameter cylinders with varying distance between phantom and floor.

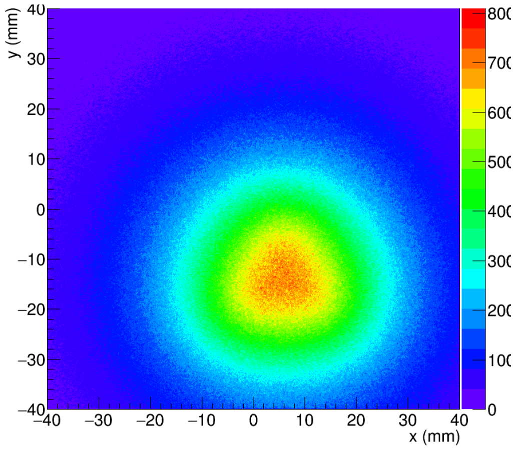


(a) Experimental image at 5 mm distance.

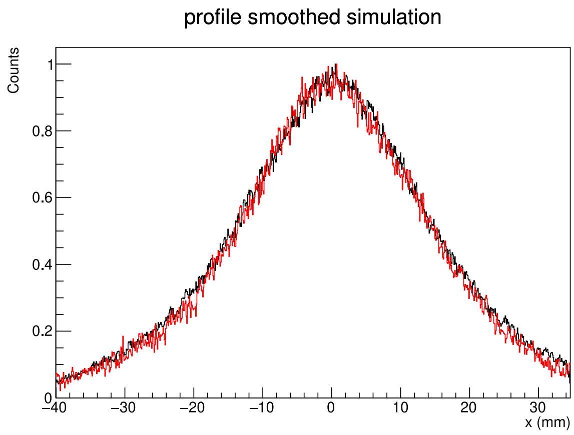


(b) Profiles at 5 mm distance. Simulated profile (black) has a minimum cutoff at 5 % of the maximum.

Figure 5.41: Simulated images with Tc-99m in 7 mm diameter cylinders with 5 mm distance. The profile from this simulation is superimposed to the correspondent experimental slice from figure 5.40b (red).

Instead, for Tc-99m images the latter does not matter.

### 5.4.4 Study of Direct Radioisotopic Imaging with Tc-99m at different depths

Figure 5.40 shows a DRI acquisition with Tc-99m in Roma phantom in cylinders of diameter 7 mm. The distance is set using the thinnest wedge of 5 mm thickness. The circles are no longer distinguishable so the spatial resolution achieved at 0 mm distance is no longer achieved at 5 mm distance. In figure A.12 on page 91 we can see all the three different positions of the Roma phantom with respect to the phosphor screen that we acquired in the experiment.

In order to simulate different distances we just need to add a certain distance between the phantom and the screen in the simulated experimental setup. For these simulations, we are using the Roma phantom basement thickness of 1 mm.

In figure 5.41 we provide the simulation for Tc-99m in 7 mm diameter cylinders for distance equal to 5 mm. The profiles of the simulation and the experiment are superimposed in figure 5.41b. The statistics is not very good but the overall trend and width of the distribution is similar.

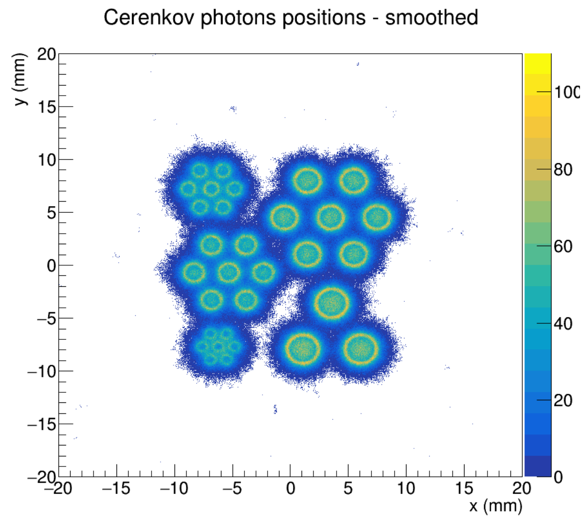


(a) Simulated 2D image.

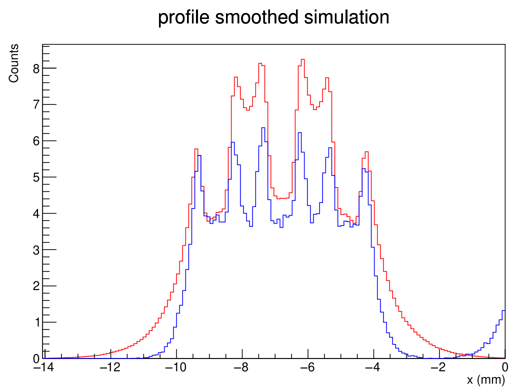


(b) Profiles across three cylinder of 1.0 mm diameter. Blue line is Ag-111 and red-line is Ga-68.

Figure 5.42: Simulations of CLI with Ag-111 in PMMA phantom. The cylinder from 0.7 mm diameter to 2.5 mm diameter are filled. The standard deviation of the applied Gaussian filter is 0.1 mm, the transmission coefficient of the solution is set to 0.4.

## 5.5 Ag-111 Cerenkov Luminescence and Direct Radioisotopic Imaging simulations

In the previous sections we compared experimental data and simulated images with the aim of validating the simulation. Thanks to this validation, we can now simulate other radionuclides for which we could not make any experiment.

As already mentioned in section 4.2 on page 39, the radionuclides used in the experiment were chosen also because of their similarity with the radiation features of Ag-111, that is the final objective of ISOLPHARM collaboration. Table 4.4 contains the main products of their decay.

We simulate in the same phantoms used in the experiment at CAPiR. The simulation were performed with the same Geant4 applications using Ag-111 radionuclides instead of Ga-68 and Tc-99m and using the set of parameters that we determined in sections 5.3 and 5.4. Figure 5.42a shows a simulation in which a PMMA phantom was used, cylinders from diameter 0.7 mm to 2.5 mm are filled with Ag-111. The acquisition modality is CLI. The transmission value for the solution is set to 0.4 and the standard deviation of the Gaussian filter is set to 0.1 mm.

The typical features of CLI in PMMA imaging: increase of counts at the edges, tails rapidly going to zero and central peak are still present. Indeed, if they are due to different optical properties of the media as we stated in section 5.3 then changing the beta-emitter should not affect the shape of the distribution too much.

All the cylinders in the image seem resolved but this figure as it is does not represent the real situation. In fact, in our simulation we are not modeling the noise that in the real experiment played an important role in limiting the spatial resolution.

A priori, we cannot model the impact of noise in the case of Ag-111 images. Therefore, we compare the simulations of Ag-111 and Ga-68. In figure 5.42b we plot the profiles across three cylinders of 1.0 mm diameter of PMMA phantom. The histogram with red line is Ga-68 and the one with blue-line is Ag-111. We can see that the distributions of Ga-68 filled cylinders have a larger spread because of the greater energy of the emitted beta particles in the decay (see table 1.1). We expect the images with Ag-111 to have a better spatial resolution with respect of those with Ga-68. With Ga-68 we were not sure if the cylinders of 1.5 mm diameter were resolved. To be conservative, we can expect at least

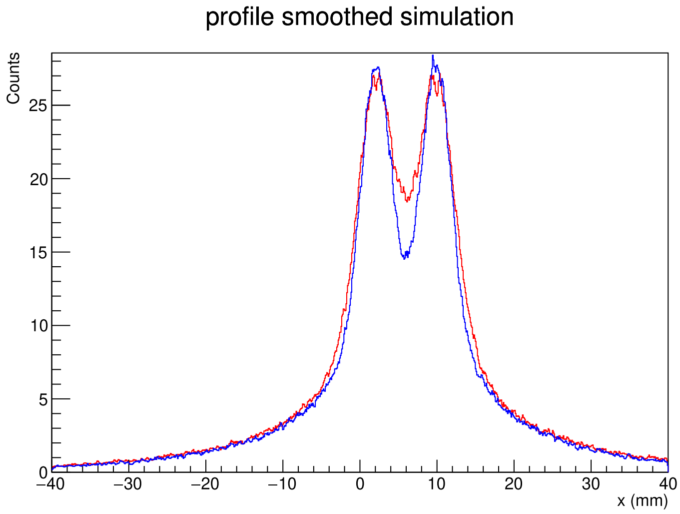


Figure 5.43: Profiles of Ga-68 (red) and Ag-111 (blue) for DRI in 4 mm diameter cylinders of Roma phantom.

to be able to resolve these cylinders with Ag-111.

In figure 5.43 we superimpose the profiles obtained in DRI simulations with 4 mm diameters cylinders in Roma phantom for both Ag-111 and Ga-68. We can appreciate that the blue peaks representing Ag-111 signal are more separated than the red peaks representing Ga-68 signal. Therefore, the simulations predict a better spatial resolution for Ag-111 DRI images. This time too, the cause is in the difference of the energy distribution of the beta particles emitted.

For DRI mode some simulated images at varying distance are shown in figure A.16 on page 95 and in figure A.17 on page 96. If we simulate the same number of decays of Ag-111 as for the other radionuclides, we collect much less scintillation photons since the intensity for the gamma-rays is lower (see table 4.4). In a real experiment, we will need to acquire for longer times in order to acquire images with enough contrast.

Therefore, for DRI with Ag-111 we expect to reach the spatial resolution of Ga-68 (4 mm) when the Roma phantom lays on the sample support.

## 5.6 Study for the minimum detectable activity

As described in section 2.1, shot noise plays a role in the possibility to effectively discern the details in an image. In our setup the number of counts in the CCD will be directly proportional to the number of decay events that took place during the acquisition.

$$N_{\text{counts}} \propto \Delta N \tag{5.5}$$

where $\Delta N$ is expressed in equation 1.11.

Let us suppose to have such a short acquisition time that $t_1 - t_2 \ll \tau$. In this case we can apply equation 1.12 and deduce that we can increase the number of counts linearly with the acquisition time.

$$N_{\text{counts}} \overset{t_1 - t_2 \ll \tau}{\propto} t_1 - t_2 \tag{5.6}$$

We may think that, as long as the condition is respected, any shot-noise limited image may be resolved increasing the acquisition time. Instead, since in real conditions we have to consider the presence of a background flux of counts per pixel per second, this is not guaranteed. If the flux of optical photons that constitutes the signal is lower than the flux of noise then even increasing the acquisition time we will not be able to tell the signal and the background apart.

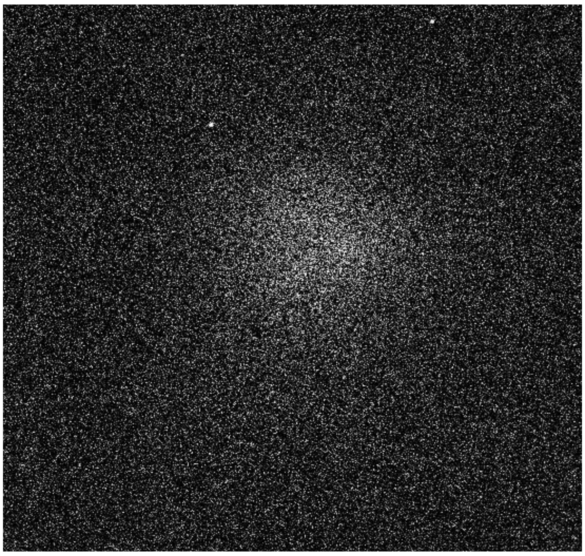

(a) Acquisition for 120 s. Activity per cylinder is 14 kBq. Counts per cylinder are $1.7 \times 10^6$.

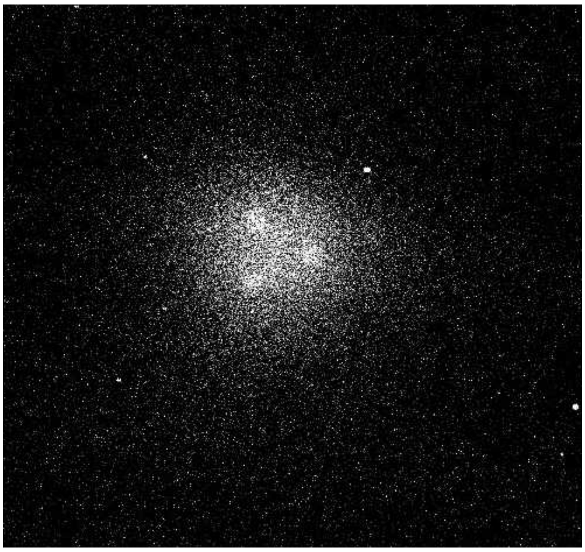

(b) Acquisition for 600 s. Activity per cylinder is 14 kBq. Counts per cylinder are $8.3 \times 10^6$.

Figure 5.44: Acquisitions of Ga-68 in HDPE phantoms with different activity and different time intervals.

We take a sample of images with four combinations of activity and acquisition time. They are shown in figure 5.44. The image obtained with the longest time interval but with the lowest activity (figure 5.44b) is resolved. Thus we can state that samples of Ga-68 with activity $> 14\,\text{kBq}$ can be distinguished from the background. Other images acquired with CLI in 2.5 mm of HDPE phantom with different activities of Ga-68 and for different acquisition time can be seen in figure A.14 on page 93.

## 5.7 Correlation between source activity and image density

Internal dosimetry calculations are one of the tasks of the ISOLPHARM collaboration [106]. A possible way to complete these calculations is by performing Monte-Carlo simulations. They require in input the activity of the source that are usually provided by PET/SPECT images [107].

In this context, Xtreme instrument may be able to supply the activity information necessary to set up dosimetry calculations. We investigate this possibility looking for a correlation between the injected activity in the sources (that is directly proportional to the number of decay events since there are the conditions to apply equation 1.12) and the retrieved intensity of the pixels in the area where the source is imaged.

The injected activity is estimated as described in equation 4.2. We will evaluate ratios of activities per cylinder.

$$\text{ratio} = \frac{\rho_{\text{activity}}(t_1)V_1}{\rho_{\text{activity}}(t_2)V_2} \tag{5.7}$$

We consider the predominant relative error of 30 % on the volumes as described in section 4.3. If we apply error propagation under the assumption of non-correlated volumes, the relative error on the ratios of activities in different cylinders is

$$\frac{\sigma_{\text{ratio}}}{\text{ratio}} \simeq \sqrt{\left(\frac{\sigma_{V_1}}{V_1}\right)^2 + \left(\frac{\sigma_{V_2}}{V_2}\right)^2} \simeq 40\,\% \tag{5.8}$$

This is just a rough indication of the uncertainty affecting the estimation of the ratios of activities.

In case cylinders of different diameter are filled at the same time, we can simplify the ratio to

$$\text{ratio} = \frac{V_1}{V_2} \tag{5.9}$$

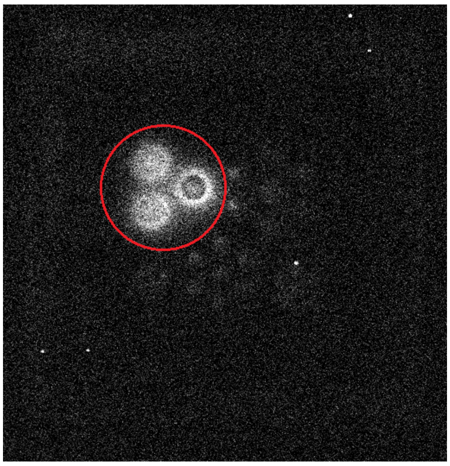

(a) The area considered contains all the cylinders.

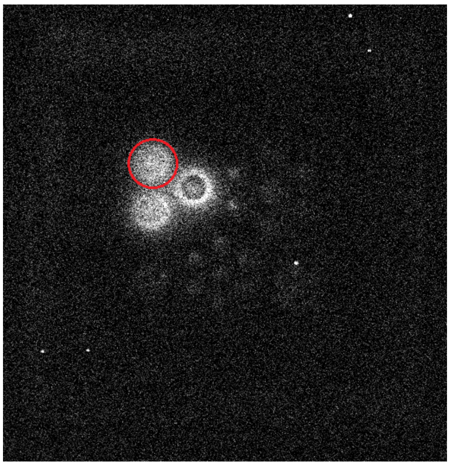

(b) The area considered contains only one cylinder.

Figure 5.45: Two schemes representing the same image (from figure A.1b) and different areas for the measurement.

| Diameter (mm) | Activity per cylinder (kBq) | Intensity per cylinder (a.u.) |
|---|---|---|
| 5 | 82 | 154 |
| 4 | 53 | 98 |
| | Ratio of activities (kBq/kBq) | Ratio of intensities (a.u./a.u.) |
| 5 mm / 4 mm | 1.56 | 1.57 |

Table 5.3: Activity analysis for DRI with Ga-68 in Roma phantom.

For example, we consider the image of Ga-68 CLI inside 2.5 mm diameter cylinders of PMMA phantom in figure A.1b. We can define three identical circles that enclose one of the cylinder area each one, as represented in figure 5.45b. The integral is calculated summing the bin content of all the bins inside the selected area. An integration at the level of the single cylinder can give information also on the distribution of activity within the same image. Instead, the coarse circular selection depicted in figure 5.45a can be used if no spatial information is required and in case the background is negligible with respect to the signal.

The simplest response as function of the activity that we can suppose is a straight line without constant term.

$$y = Bx \tag{5.10}$$

where $y$ is the integrated intensity, $x$ is the activity and $B$ is a constant.

We start this analysis considering the image acquired in DRI with Ga-68 in 4 mm and 5 mm diameter cylinders of Roma phantom (figure 5.32b on page 65). Since in this image there are two sources of different activity, we can test the linear response function. We call $x_1$ the activity in each cylinder of 4 mm diameter and $x_2$ the activity in each cylinder of 5 mm diameter. If equation 5.10 holds, then the ratio of the activities should be equal to the ratio of the correspondent integrated densities $y_1$ and $y_2$.

$$\frac{y_1}{y_2} = \frac{Bx_1}{Bx_2} = \frac{x_1}{x_2} \tag{5.11}$$

We report in the table 5.3 the measured integrated densities, the injected activities and the ratios. The intensities are measured for each cylinder (figure 5.45b).

We can see that the ratios very close to each other so we can expect to be able to build a proper response function collecting more data in future experiments. We stress again that we are not providing any rigorous uncertainty analysis because we are just investigating the features of the Xtreme.

| Diameter (mm) | Activity per cylinder (kBq) | Intensity per cylinder (a.u.) |
|---|---|---|
| 2.5 | 36 | 56 |
| 2.0 | 23 | 33 |
| 1.5 | 13 | 13 |
| | Ratio of activities (kBq/kBq) | Ratio of intensities (a.u./a.u.) |
| 2.0 mm / 2.5 mm | 0.64 | 0.59 |
| 1.5 mm / 2.0 mm | 0.56 | 0.40 |
| 1.5 mm / 2.5 mm | 0.36 | 0.24 |

Table 5.4: Activity analysis for DRI with Ga-68 in PMMA phantom.

| Diameter (mm) | Activity per cylinder (kBq) | Intensity per cylinder (a.u.) |
|---|---|---|
| 2.5 | 65 | 122 |
| 2.0 | 38 | 107 |
| 1.5 | 20 | 17 |
| 1.0 | 7 | 58 |
| | Ratio of activities (kBq/kBq) | Ratio of intensities (a.u./a.u.) |
| 2.0 mm / 2.5 mm | 0.59 | 8.01 |
| 1.5 mm / 2.0 mm | 0.51 | 1.67 |
| 1.0 mm / 1.5 mm | 0.35 | 0.24 |
| 1.0 mm / 2.5 mm | 0.10 | 4.17 |

Table 5.5: Activity analysis for CLI with Ga-68 in PMMA phantom.

The second image that we study is the DRI with Ga-68 in 2.5 mm, 2.0 mm, 1.5 mm diameter cylinders of PMMA phantom (figure 5.35b). In this case three different groups of cylinders with different activity are available. For this image too the intensities are measured for each cylinder (figure 5.45b).

The ratios of activities and intensities in table 5.4 are comparable but they are not as close as for the image in figure 5.32b. We intentionally reported the ratios with the smaller diameter quantity at the numerator and the larger diameter one at the denominator to show that, in this cases, we always measure ratios that are smaller than the expected values. We interpret this fact as a manifestation of the increasing difficulty in filling cylinders of decreasing diameter. In fact, wide cylinders can be easily and completely filled of radioactive solution while a narrower ones can be blocked by air bubbles thus hosting less radioactive solution than expected.

Now we study a case in which the different sources are used in different images. We use the acquisitions with CLI and Ga-68 in PMMA phantom (figure A.1). The diameter of the cylinders filled varies from 2.5 mm to 1.0 mm. The intensities are measured for all the cylinders of each group together because they are not well separated (figure 5.45a). In table 5.5, we report only some of the ratios that can be calculated.

The measured ratios differ from the expected ones. We think this is because we did not keep attention in maintaining the same settings between different acquisitions. The Bruker Molecular Imaging Software offers plenty of parameters to be optimized so we need to practice more to be able to have as much degrees of freedom as possible under control.

Concluding, we verified the possibility to estimate the activity of a source from DRI images. The success of this quantitative analysis is linked to the capability to control the acquisitions settings ensuring their stability during the entire experimental session. We think that if we achieve this stability we can provide a quantitative estimation of the activity also from CLI images.

# Chapter 6

# Conclusions

We introduced the context for the ISOLPHARM project. The development of a radiopharmaceutical based on the radioisotope Ag-111 requires a convenient imaging tool: the Bruker In-Vivo Xtreme II. Such imaging device is able to exploit both beta- and gamma-rays that are emitted in radionuclide decays via two imaging modalities: Cerenkov Luminescence Imaging and Direct Radioisotopic Imaging.

This thesis work is the first step of a very long project involving pre-clinical studies with Ag-111. Indeed, the experiment that we performed at CAPiR was the first one performed by the ISOLPHARM collaboration involving the Bruker In-Vivo Xtreme II. We understood the physics at the basis of its working principles and we individuated several quantities that play a role during the acquisitions. For these quantities, we estimated an approximated range so that we may know what can and can not be imaged with this instrument.

We verified that indeed both imaging modalities work with proper radionuclides. Using experimental data acquired with Ga-68 and Tc-99m we validated a Geant4 Monte-Carlo simulation. Therefore, we can expect that images acquired with Ag-111 sources directly on the phantom support will have spatial resolution:

- 1.5 mm for CLI;
- 4 mm for DRI.

From this point, the collaboration will be able to determine the features of this instrument with increasing precision and, finally, to predict the outcome of new experiments. The latter will be run within the new big-scale experiment, ADMIRAL, that is going to take place in the following three years (2022/2025).

Practically, the next step is to integrate the simulation described in this thesis with a mouse model. We will use MOuse whole BodY (MOBY) phantom, that is a realistic and flexible 4D digital mouse phantom [108]. The high level of accuracy of this model allows to simulate experiments in which the dose is delivered to specific organs. Two views of the mouse phantom in which many organs (but not all the ones available) are visible is shown in figure 6.1. The resulting simulated images will be useful in preparation of the next experiment in which Ag-111 will be injected in mice.

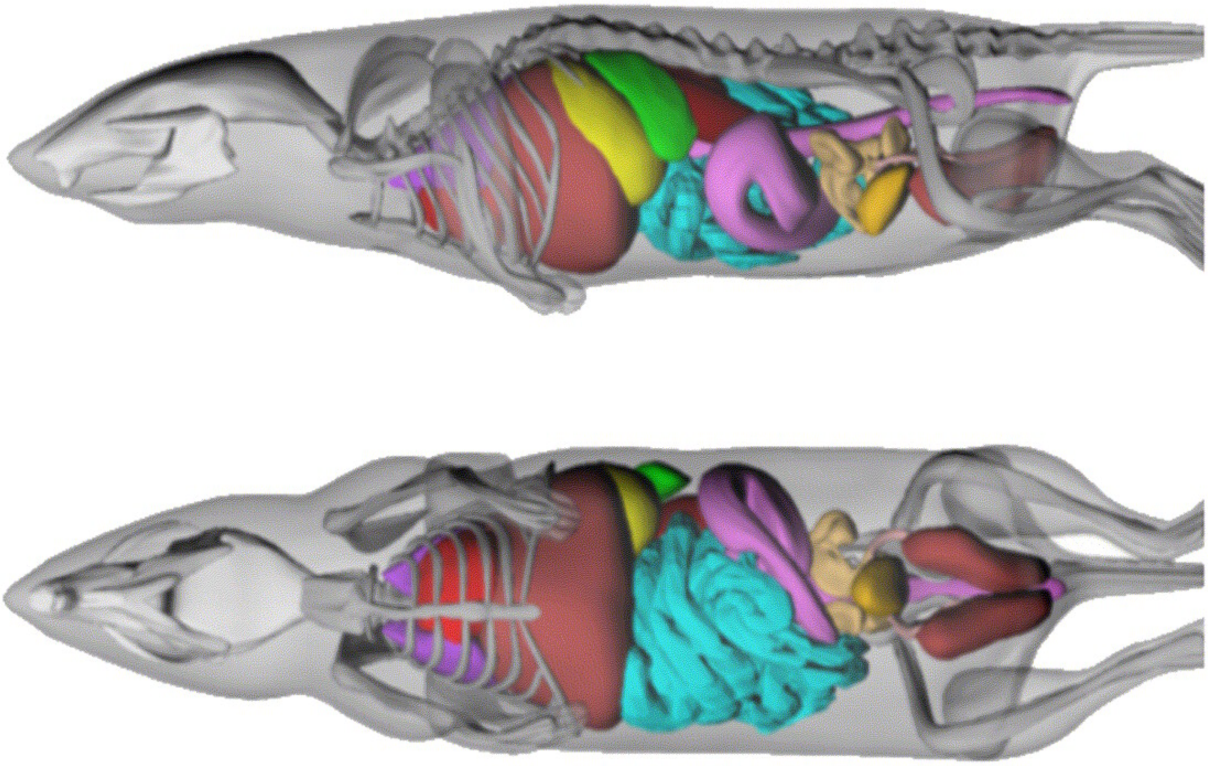

Figure 6.1: Anterior (bottom) and lateral (top) views of the digital mouse phantom. From [108].

# Appendix A

# Additional Figures

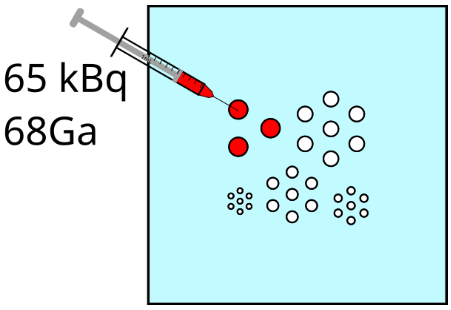


(a) 2.5 mm diameter scheme.

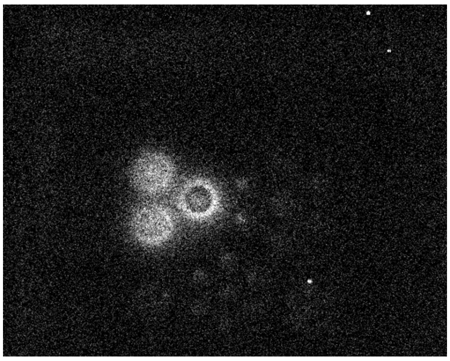

(b) 2.5 mm diameter image.

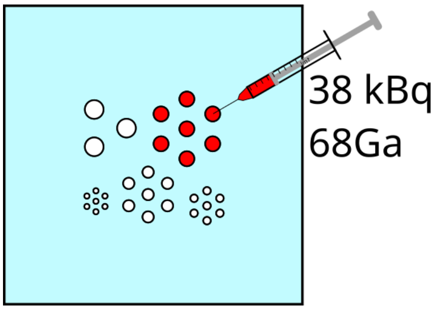


(c) 2.0 mm diameter scheme.

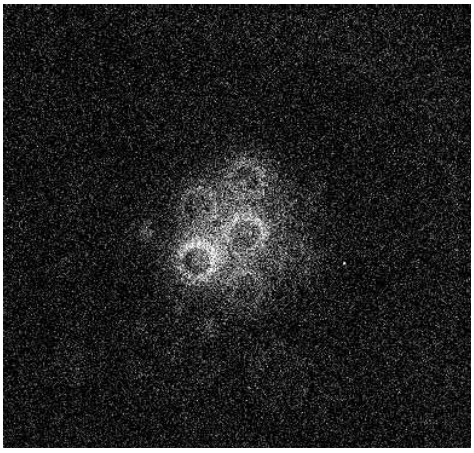

(d) 2.0 mm diameter image.

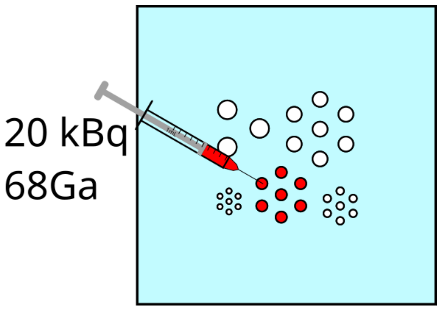


(e) 1.5 mm diameter scheme.

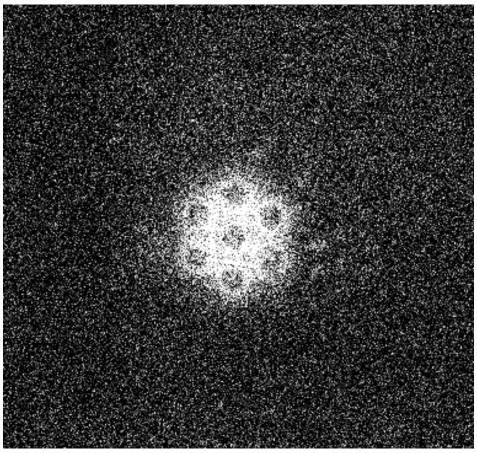

(f) 1.5 mm diameter image.

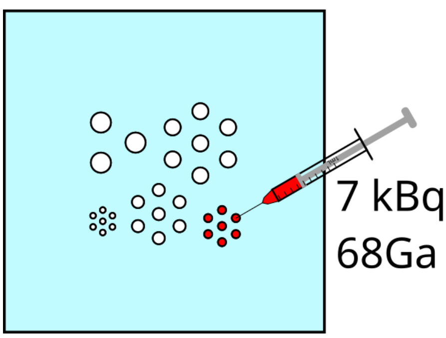


(g) 1.0 mm diameter scheme.

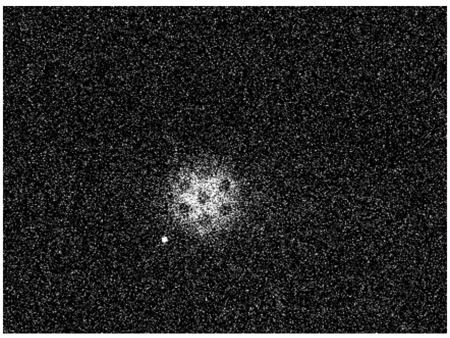

(h) 1.0 mm diameter image.

Figure A.1: Experimental images: source is Ga-68, phantom is in PMMA and the acquisition mode is CLI.

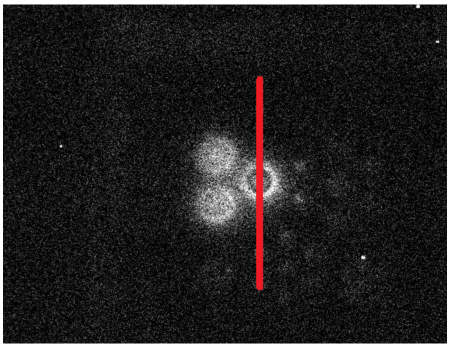

(a) 2.5 mm diameter image.

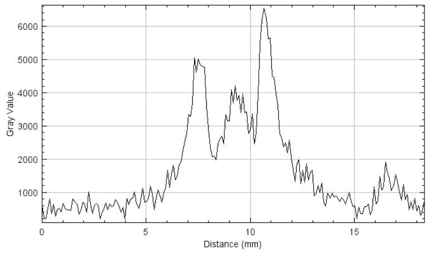


(b) 2.5 mm diameter profile across one cylinder.

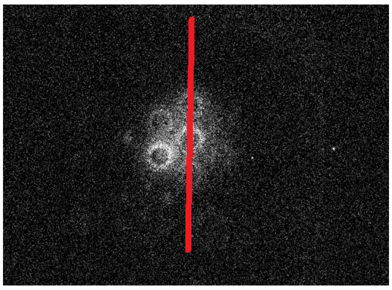

(c) 2.0 mm diameter image.

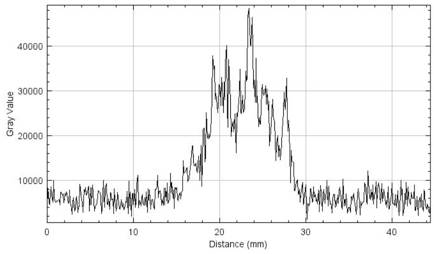


(d) 2.0 mm diameter profile across two cylinders.

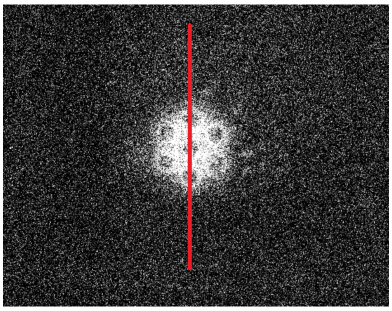

(e) 1.5 mm diameter image.

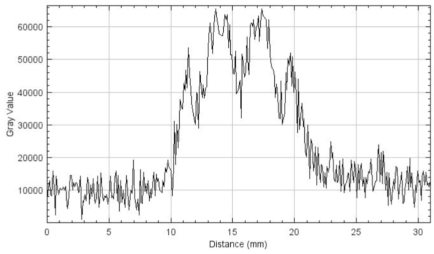


(f) 1.5 mm diameter profile across three cylinders.

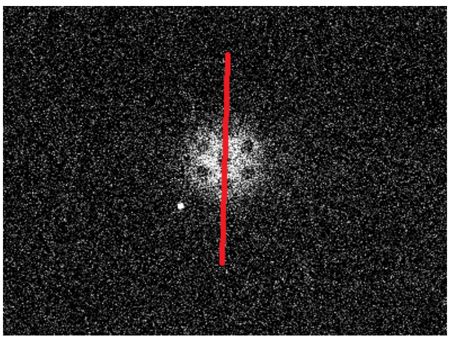

(g) 1.0 mm diameter image.

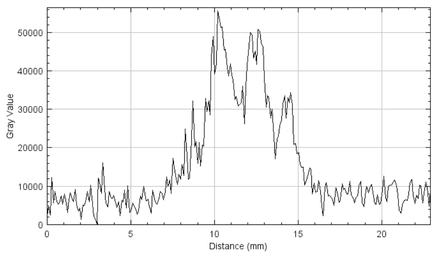


(h) 1.0 mm diameter profile across three cylinders.

Figure A.2: Experimental images: source is Ga-68, phantom is in PMMA and the acquisition mode is CLI for 2 min. On the left column there are the 2D images. A red line indicates the slice that generates the corresponding profile on the right column.

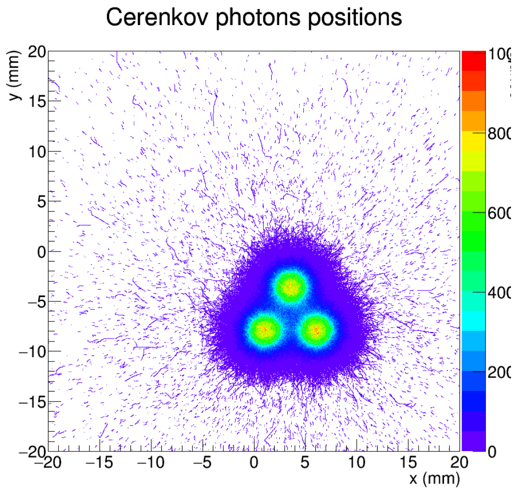


(a) Simulated image with solution refraction index equal to water one and with 100 % transmission.

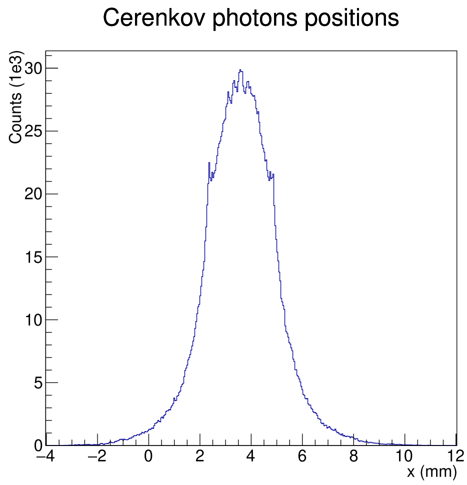


(b) Profile of figure A.3a.

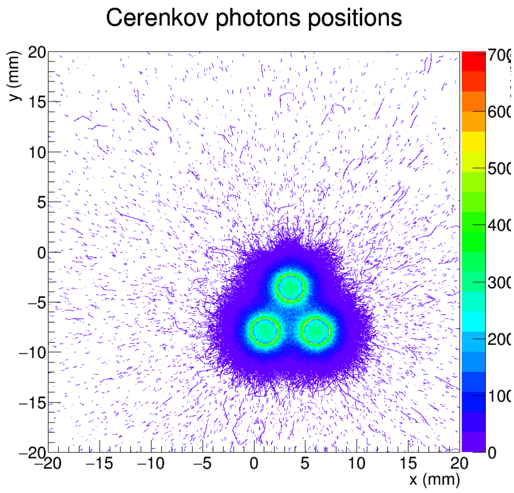


(c) Simulated image with solution refractive index equal to 1.2 and with unitary transmission.

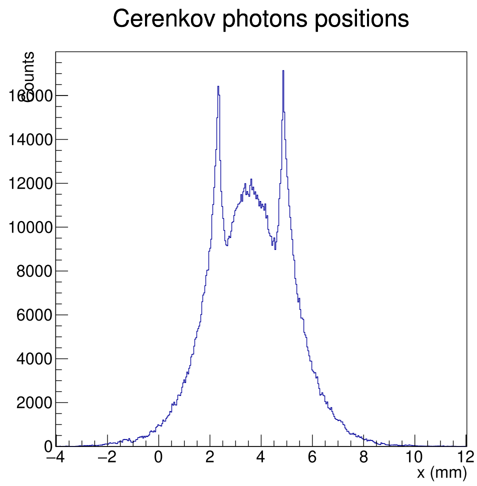


(d) Profile of figure A.3c.

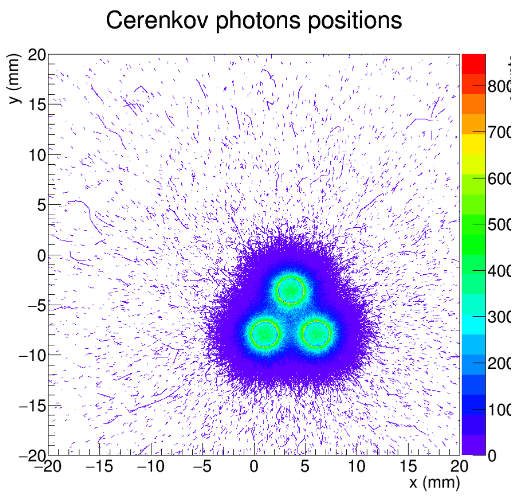


(e) Simulated image with transmission coefficient of optical photons equal to 0.5.

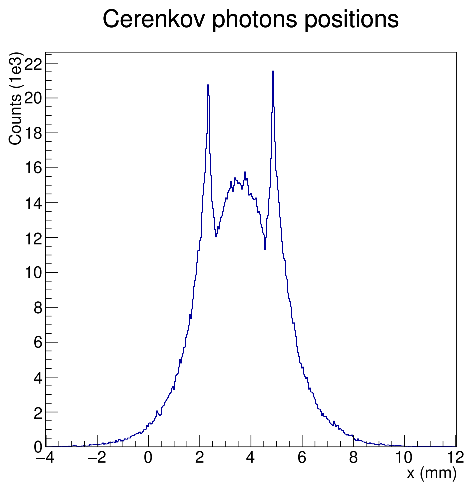


(f) Profile of figure A.3e.

Figure A.3: Simulations of CLI with Ga-68 in PMMA phantoms, 2.5 mm diameter cylinders.

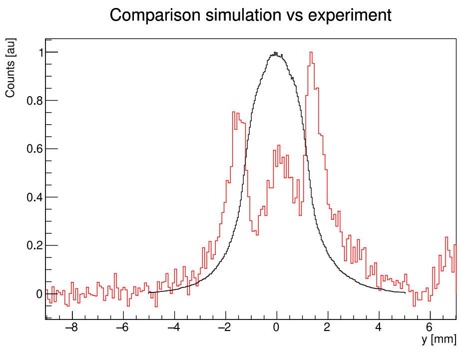


(a) Profile of simulated image with solution refraction index equal to 1.5.

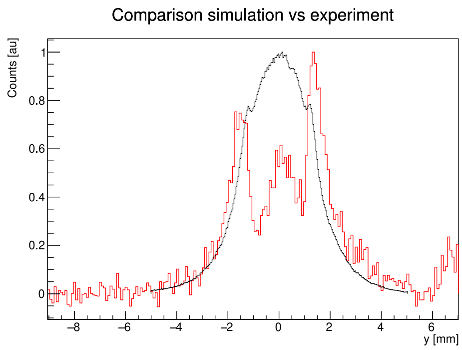


(b) Profile of simulated image with solution refraction index equal to 1.3.

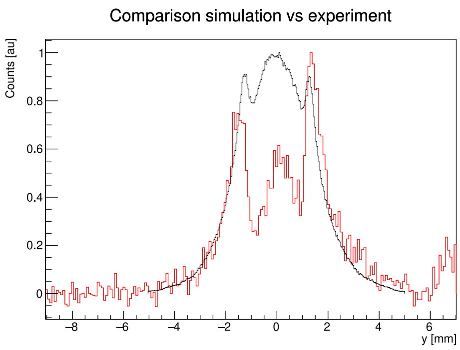


(c) Profile of simulated image with solution refraction index equal to 1.25.

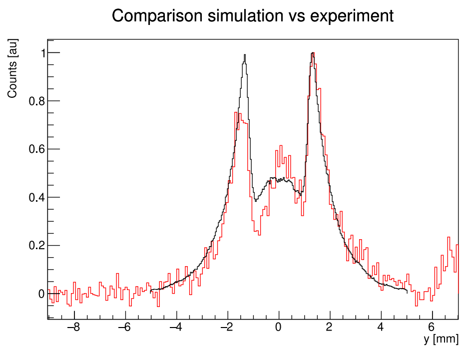


(d) Profile of simulated image with solution refraction index equal to 1.14.

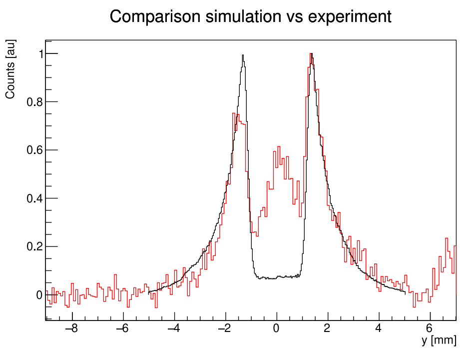


(e) Profile of simulated image with solution refraction index equal to 1.02.

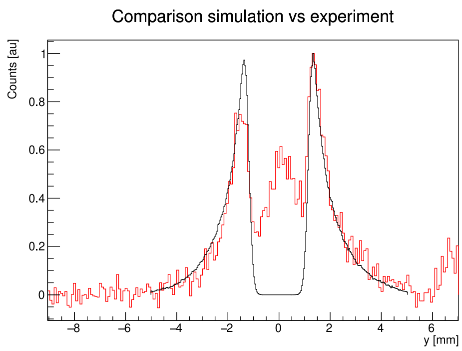


(f) Profile of simulated image with solution refraction index equal to 1.02. The cylinders are non-physically stretched so that no PMMA is present above or below the solution.

Figure A.4: Simulations of CLI with Ga-68 in PMMA phantoms, 2.5 mm diameter cylinders. The refraction index of the solution is varied in the range $[1.02, 1.5]$. The transmission coefficient is unitary.

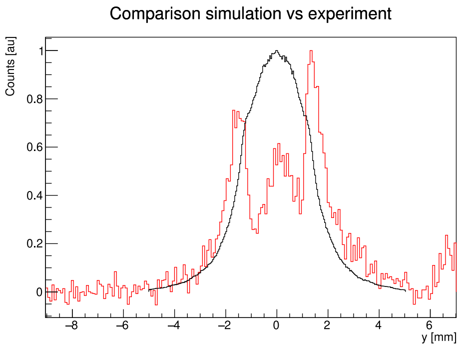


(a) Profile of simulated image with transmission coefficient equal to 1.0.

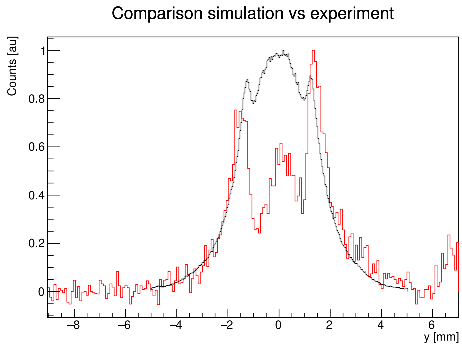


(b) Profile of simulated image with transmission coefficient equal to 0.7.

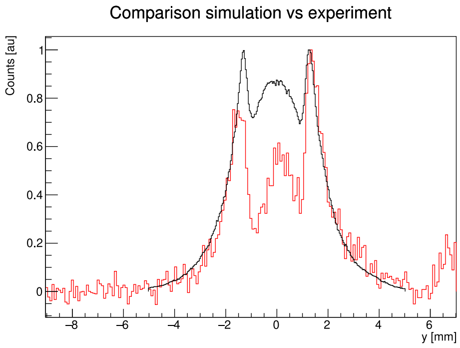


(c) Profile of simulated image with transmission coefficient equal to 0.5.

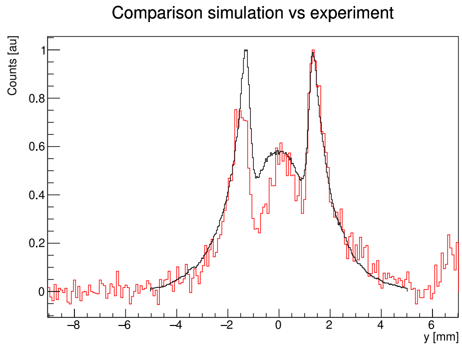


(d) Profile of simulated image with transmission coefficient equal to 0.3.

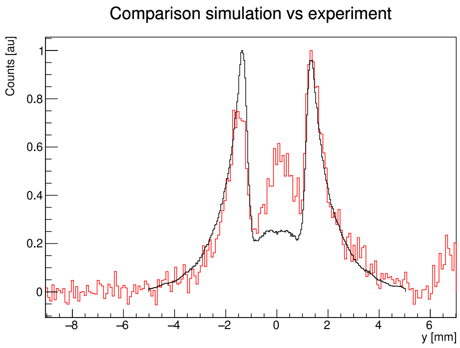


(e) Profile of simulated image with transmission coefficient equal to 0.1.

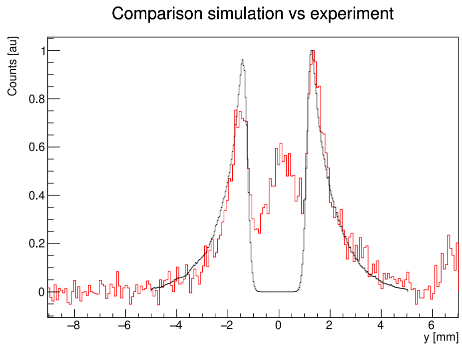


(f) Profile of simulated image with transmission coefficient equal to 0.0. The cylinders are non-physically stretched so that no PMMA is present above or below the solution.

Figure A.5: Simulations of CLI with Ga-68 in PMMA phantoms, 2.5 mm diameter cylinders. The refraction index of the solution is that of water and a Gaussian filter with $\sigma = 0.1\,\mathrm{mm}$ is applied. The transmission coefficient is varied in the range $[0.0, 1.0]$.

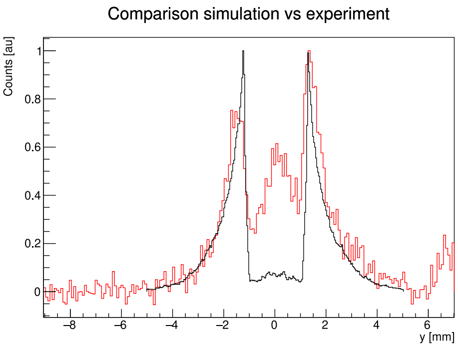


(a) Profile for no Gaussian smoothing.

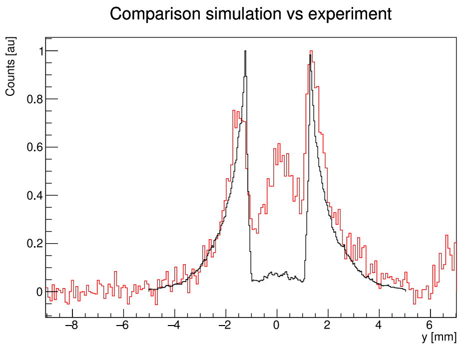


(b) Profile for $\sigma = 0.01\,\text{mm}$ Gaussian smoothing
.

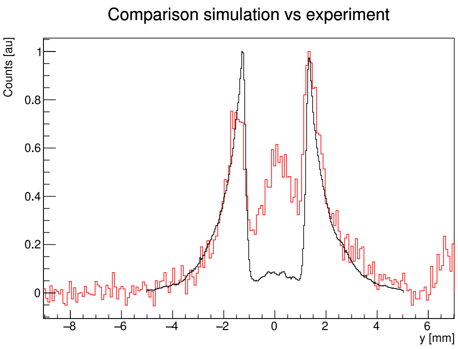


(c) Profile for $\sigma = 0.05\,\text{mm}$ Gaussian smoothing.

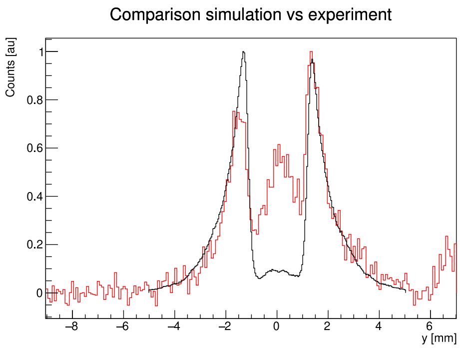


(d) Profile for $\sigma = 0.1\,\text{mm}$ Gaussian smoothing.

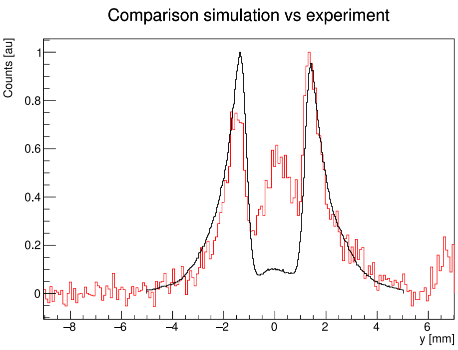


(e) Profile for $\sigma = 0.15\,\text{mm}$ Gaussian smoothing.

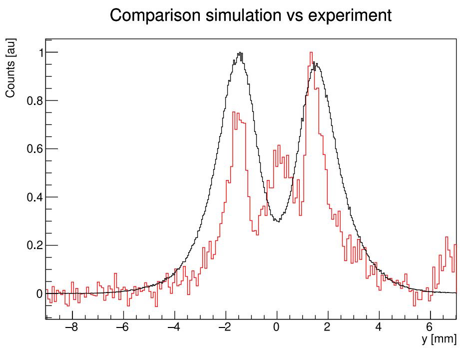


(f) Profile for $\sigma = 0.5\,\text{mm}$ Gaussian smoothing.

Figure A.6: Simulations of CLI with Ga-68 in PMMA phantoms, 2.5 mm diameter cylinders and transmission coefficient equal to 0. The profiles across one cylinder are superimposed with the correspondent profile of the experimental image in figure A.2b.

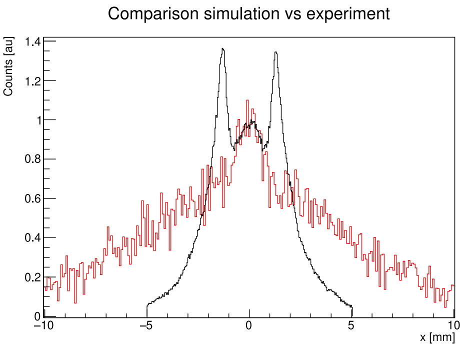


(a) Simulation 1.0 transmission for HDPE.

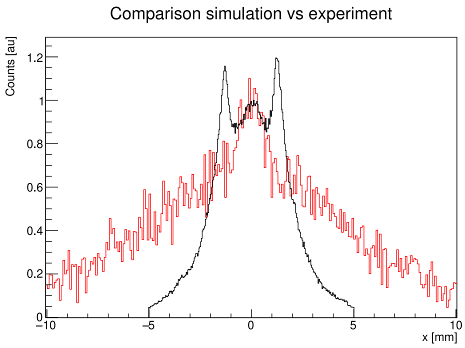


(b) Simulation 0.8 transmission for HDPE.

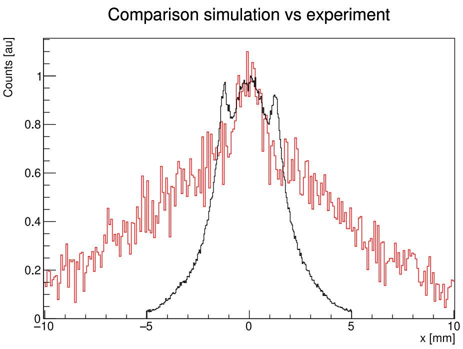


(c) Simulation 0.6 transmission for HDPE.

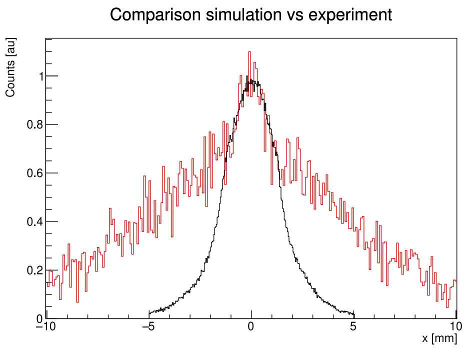


(d) Simulation 0.4 transmission for HDPE.

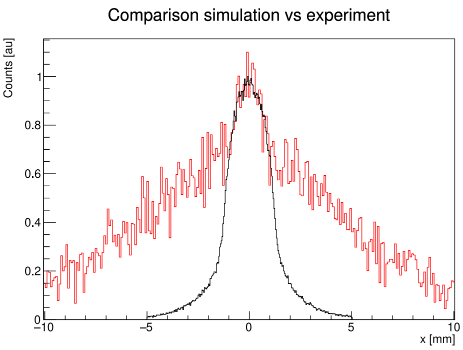


(e) Simulation 0.2 transmission for HDPE.

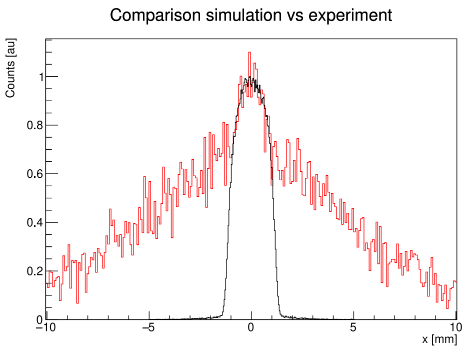


(f) Simulation 0.01 transmission for HDPE.

Figure A.7: Simulations of CLI with Ga-68 in HDPE phantoms. The transmission coefficient of the HDPE material changes between figures in the range $[0, 1]$. The solution has 0.2 transmission coefficient and a Gaussian filter with $\sigma = 0.1\,\mathrm{mm}$ is applied.

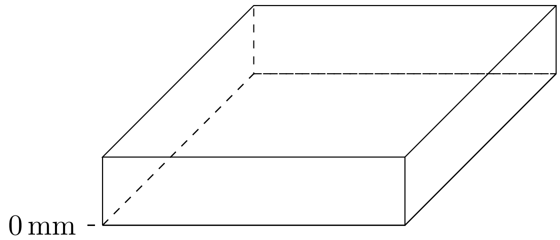


(a) Scheme at 0 mm distance phantom-support.

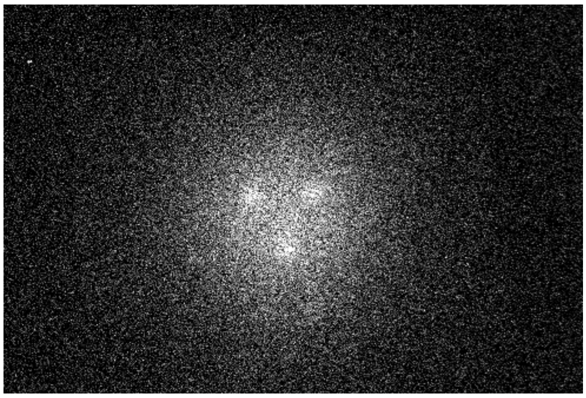

(b) Experimental image at contact. Acquisition time is 2 min.

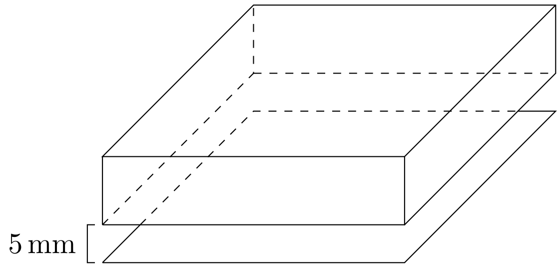


(c) Scheme at 5 mm distance phantom-support.

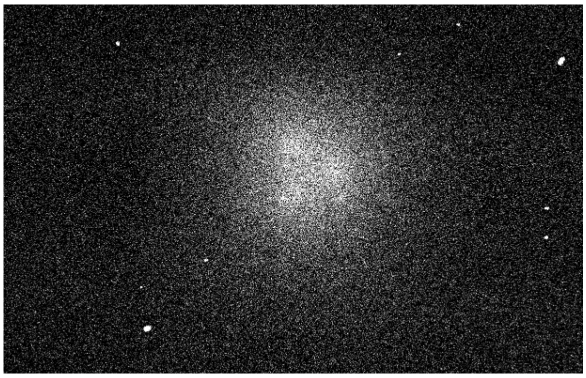

(d) Experimental image at 5 mm distance. Acquisition time is 6 min.

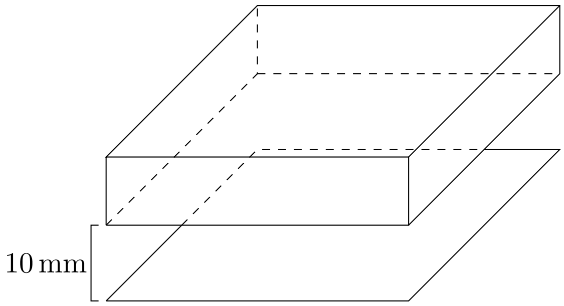


(e) Scheme at 10 mm distance phantom-support.

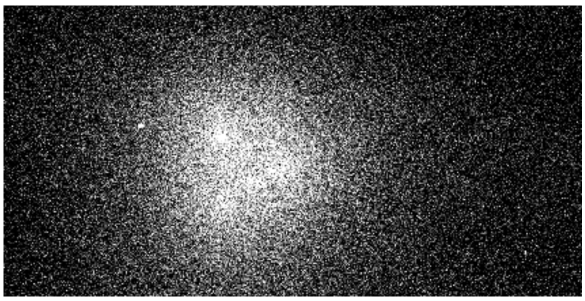

(f) Experimental image at 10 mm distance. Acquisition time is 6 min.

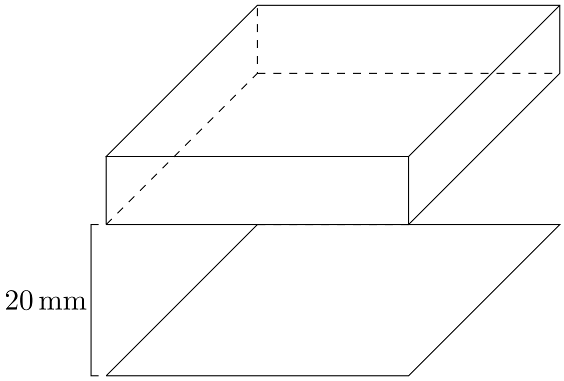


(g) Scheme at 20 mm distance phantom-support.

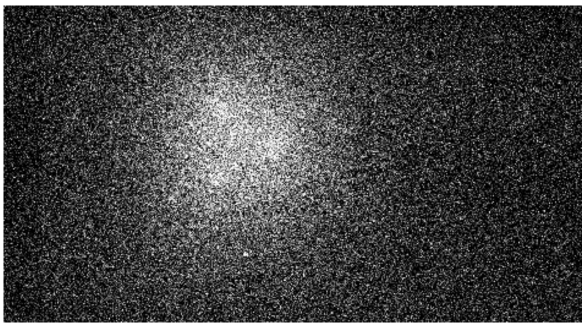

(h) Experimental image at 20 mm distance. Acquisition time is 6 min.

Figure A.8: CLI images with Ga-68 in 2.5 mm diameter cylinders of HDPE phantom with varying distance between phantom and floor.

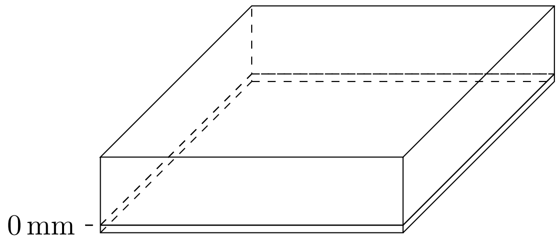


(a) Scheme at 0 mm distance.

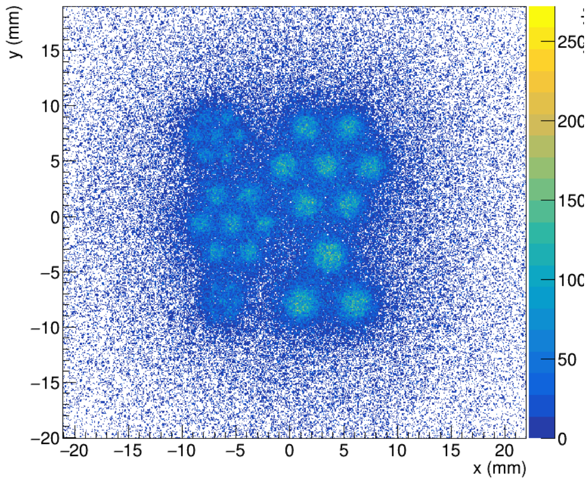


(b) Experimental image at 0 mm distance.

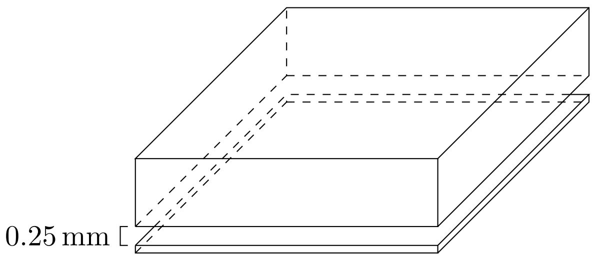


(c) Scheme at 0.25 mm distance.

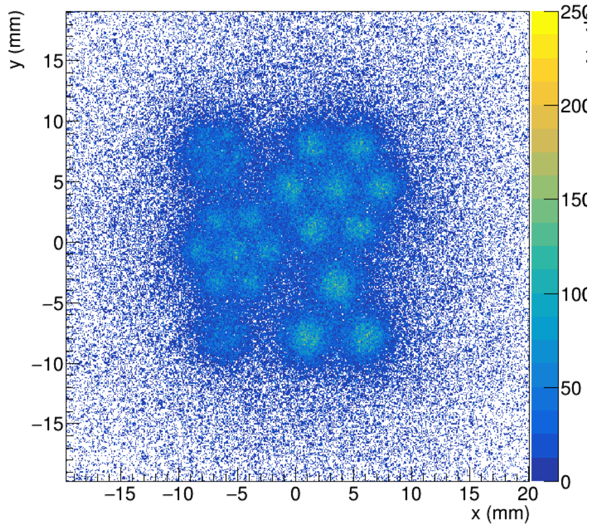


(d) Experimental image at 0.25 mm distance.

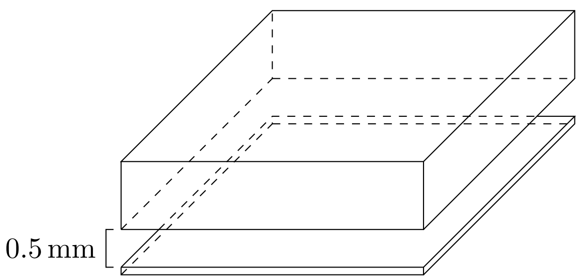


(e) Scheme at 0.5 mm distance.

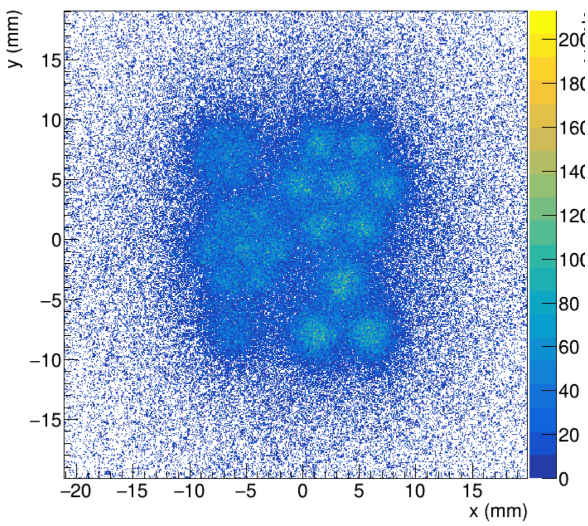


(f) Experimental image at 0.5 mm distance.

Figure A.9: Simulations of Ga-68 DRI acquisitions in PMMA phantom with varying phantom-scintillator distance. On the left the relative position between the phantom and the scintillator screen is schematically represented.

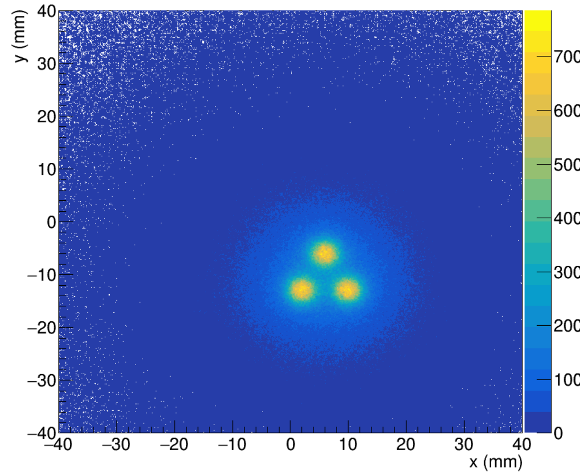


(a) Simulated DRI image for Ga-68 in 4 mm diameter cylinders of Roma phantom. The basement of the phantom is 1 mm and the offset distance is 0.25 mm.

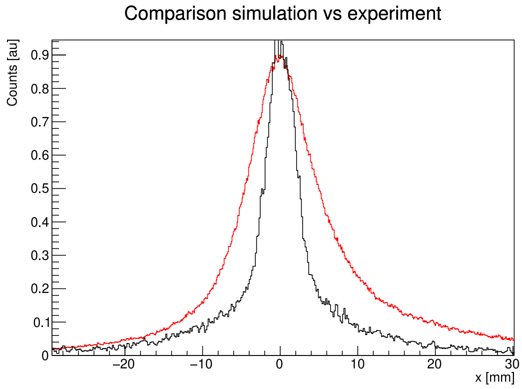


(b) Profile across one cylinder.

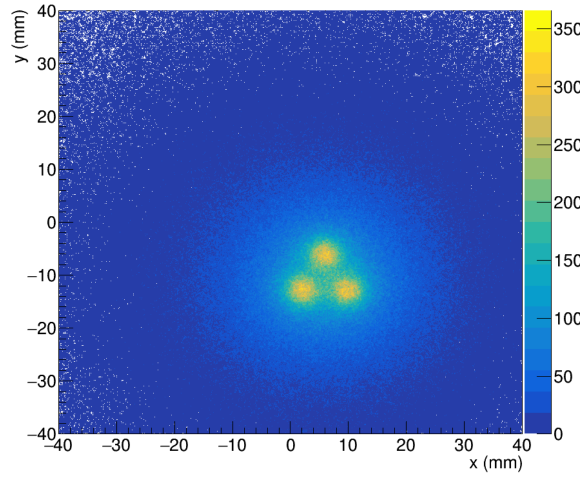


(c) Simulated DRI image for Ga-68 in 4 mm diameter cylinders of Roma phantom. The basement of the phantom is 2 mm and the offset distance is 0.25 mm.

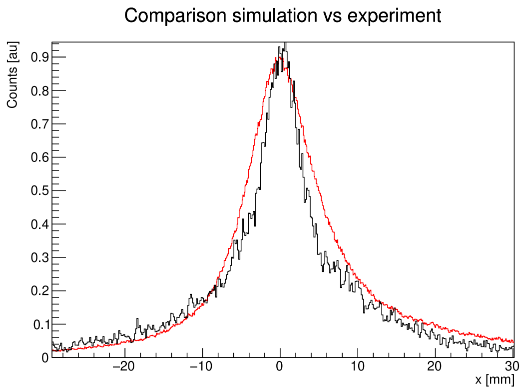


(d) Profile across one cylinder.

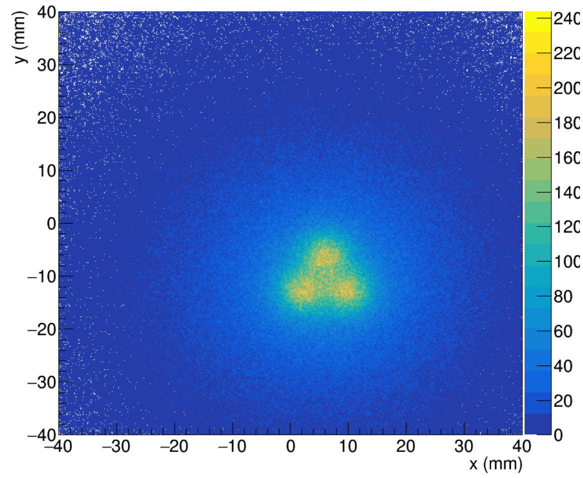


(e) Simulated DRI image for Ga-68 in 4 mm diameter cylinders of Roma phantom. The basement of the phantom is 1 mm and the offset distance is 3 mm.

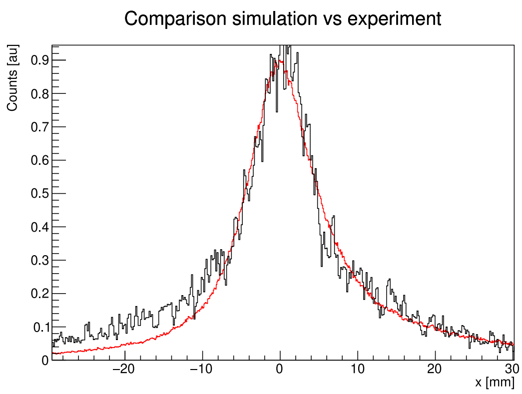


(f) Profile across one cylinder.

Figure A.10: Simulations of Ga-68 DRI acquisitions with Roma phantom. The PMMA layer on the bottom of the phantom is set to 2 mm thickness.

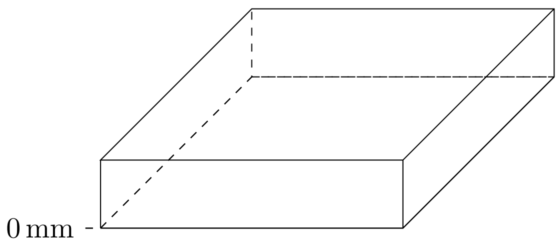


(a) Scheme at contact.

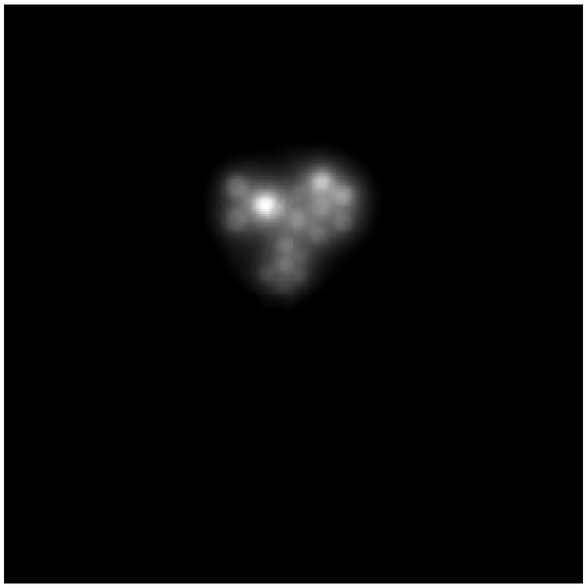

(b) Experimental image at contact.

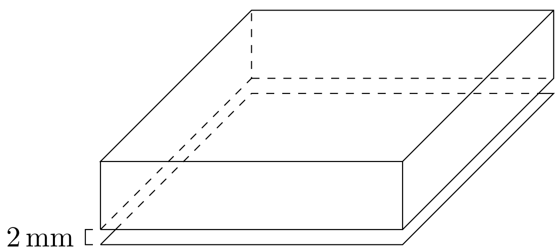


(c) Scheme at 2 mm distance.

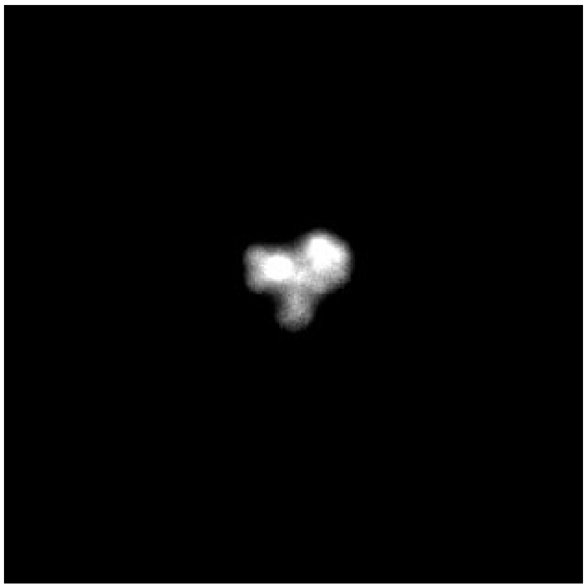

(d) Experimental image at 2 mm distance.

Figure A.11: Images with Ga-68 in 1.5 mm, 2.0 mm, 2.5 mm diameter cylinders with varying distance between phantom and floor.

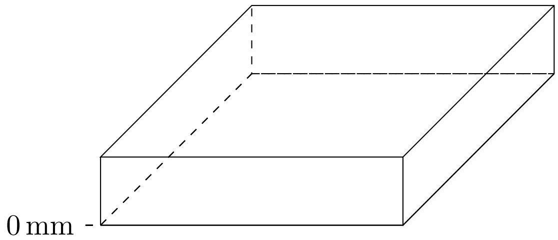


(a) Scheme at contact.

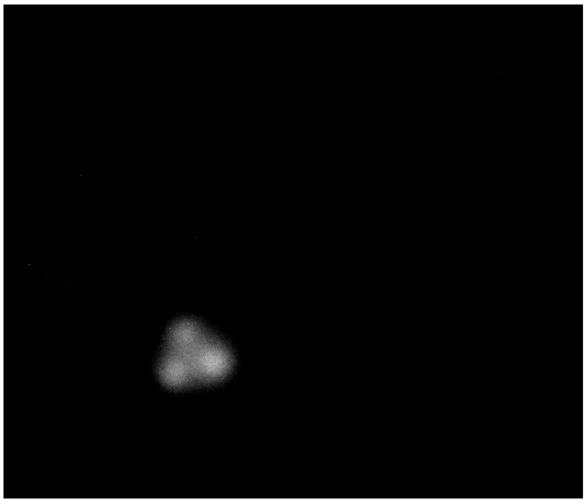

(b) Experimental image at contact.

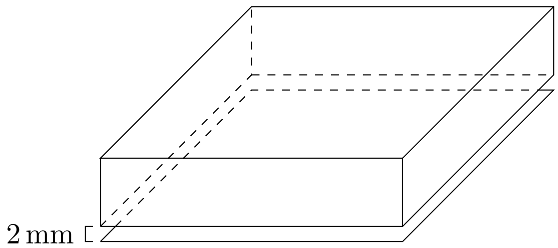


(c) Scheme at 2 mm distance.

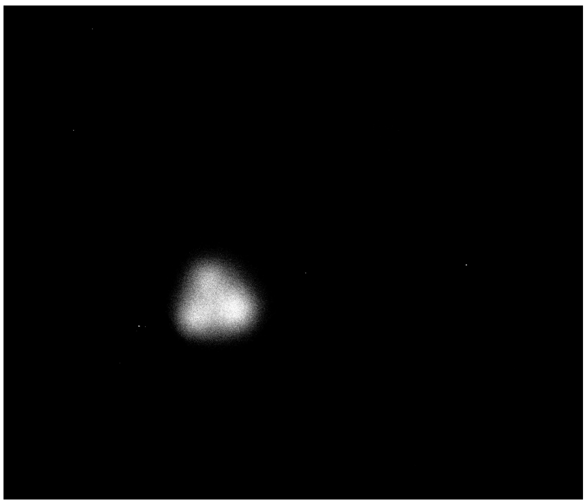

(d) Experimental image at 2 mm distance.

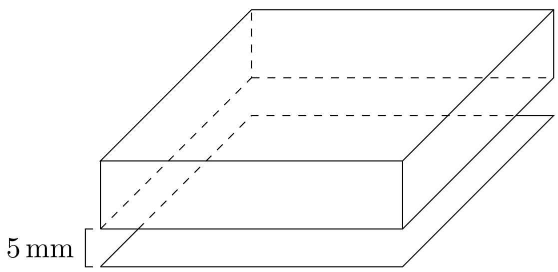


(e) Scheme at 5 mm distance.

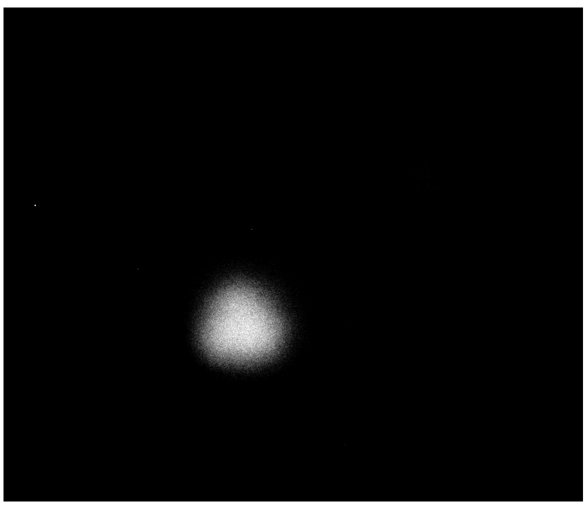

(f) Experimental image at 5 mm distance.

Figure A.12: Images with Tc-99m in 7 mm diameter cylinders with varying distance between phantom and floor.

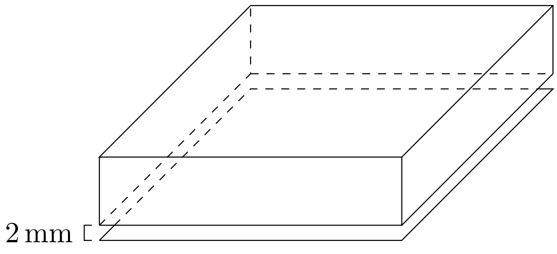


(a) Scheme at 2 mm distance.

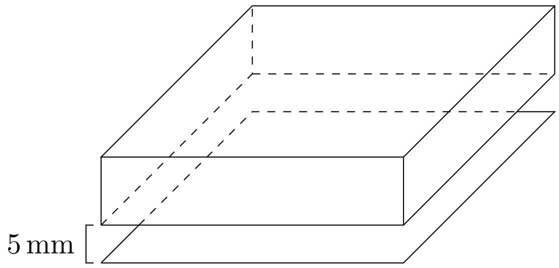


(b) Scheme at 5 mm distance.

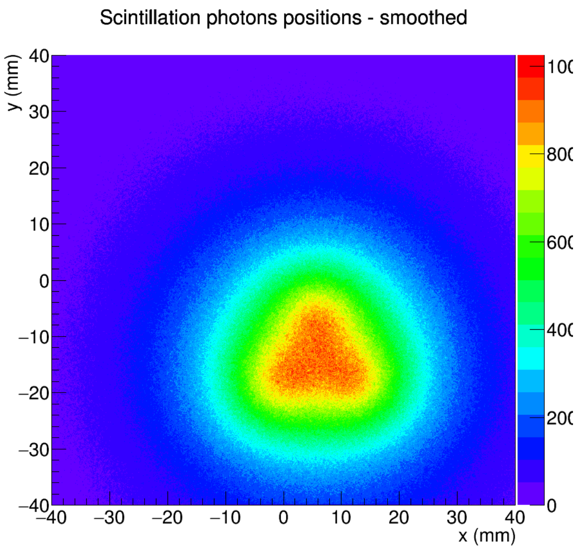


(c) Experimental image at 2 mm distance.

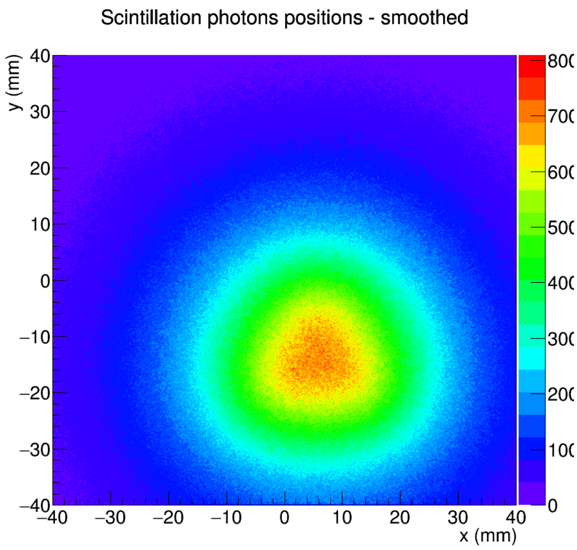


(d) Experimental image at 5 mm distance.

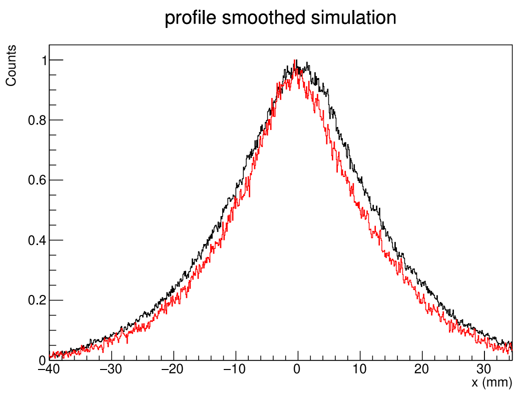


(e) Profile at 2 mm distance.

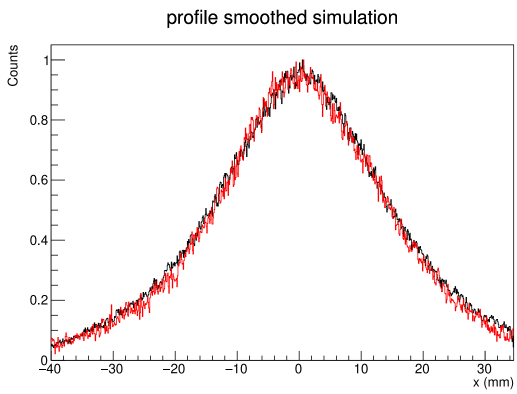


(f) Profile at 5 mm distance.

Figure A.13: Simulated images with Tc-99m in 7 mm diameter cylinders with 2 mm distance on the left column and 5 mm distance on the right column. The profiles from these simulations are superimposed to the ones sliced from figure A.12d and from figure A.12f.

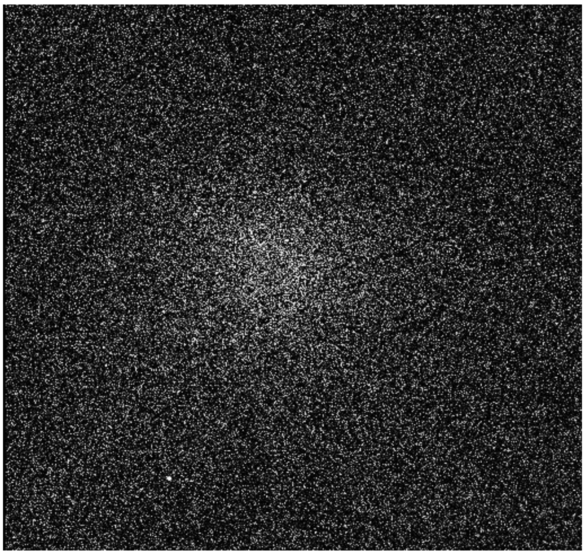

(a) Acquisition for 86 s. Activity per cylinder is 15 kBq. Counts per cylinder are $1.3 \times 10^6$.

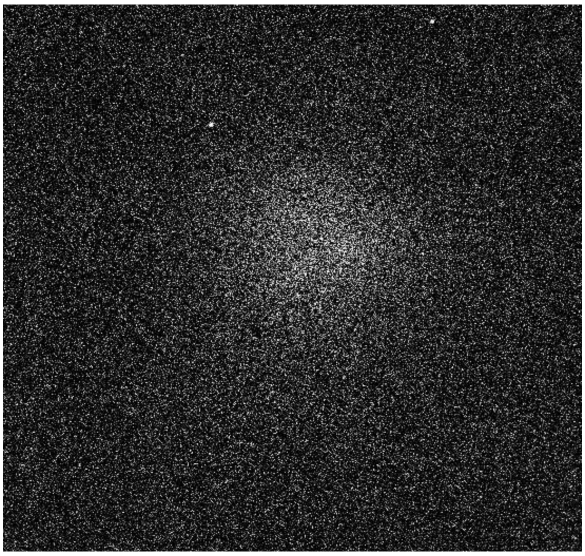

(b) Acquisition for 120 s. Activity per cylinder is 14 kBq. Counts per cylinder are $1.7 \times 10^6$.

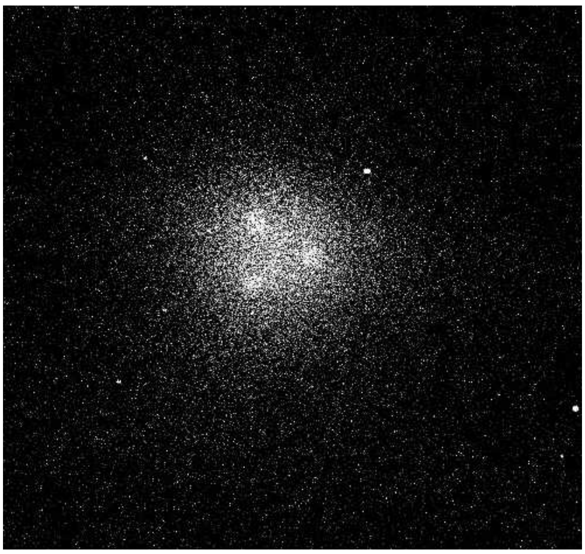

(c) Acquisition for 600 s. Activity per cylinder is 14 kBq. Counts per cylinder are $8.3 \times 10^6$.

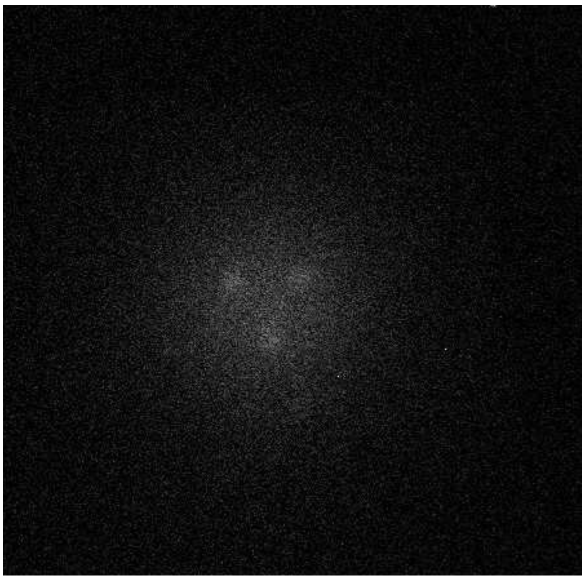

(d) Acquisition for 120 s. Activity per cylinder is 51 kBq. Counts per cylinder are $6.1 \times 10^6$.

Figure A.14: Acquisitions of Ga-68 in HDPE phantoms with different activity and different time intervals.

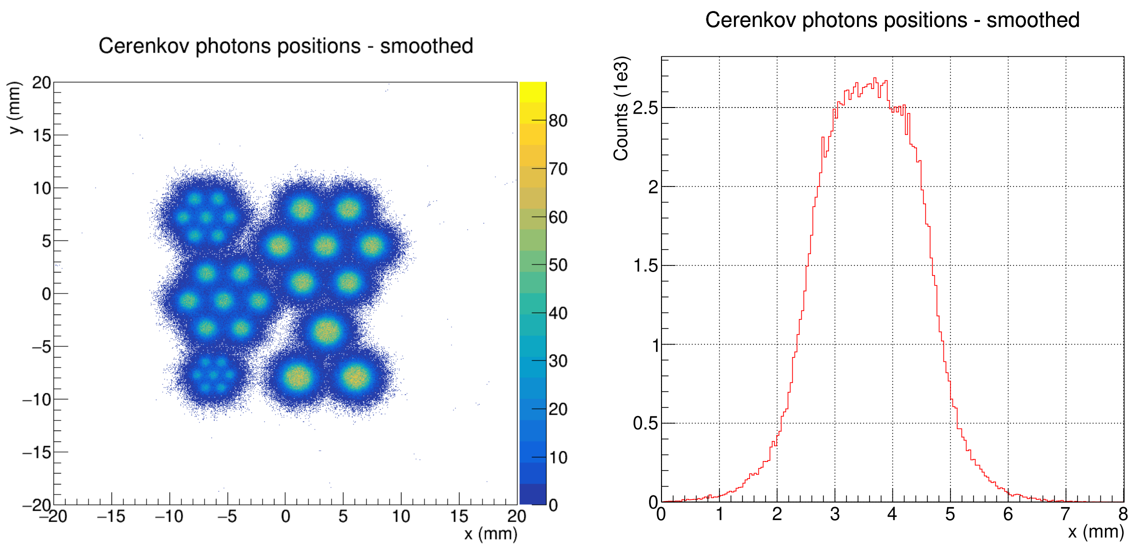


(a) Simulated 2D image.

(b) Profile across one cylinder of 2.5 mm diameter.

Figure A.15: Simulations of CLI with Ag-111 in PMMA (first row) and HDPE (second row) phantoms. The cylinder from 0.7 mm diameter to 2.5 mm diameter are filled. The standard deviation of the applied Gaussian filter is 0.1 mm, the transmission coefficients of the solution and the HDPE material are set to 0.4 and 0.2 respectively.

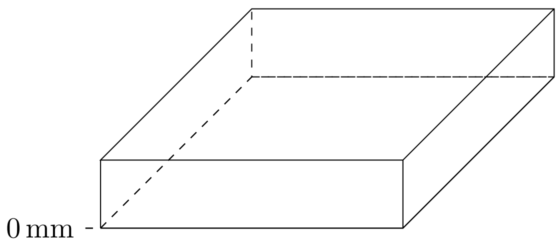


(a) Scheme at contact.

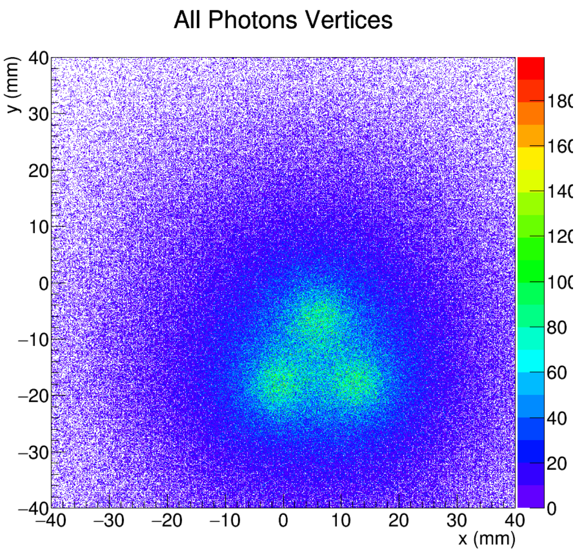


(b) Simulated image at contact.

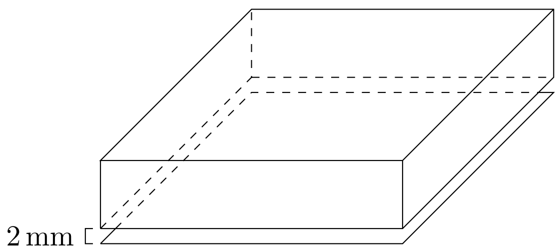


(c) Scheme at 2 mm distance.

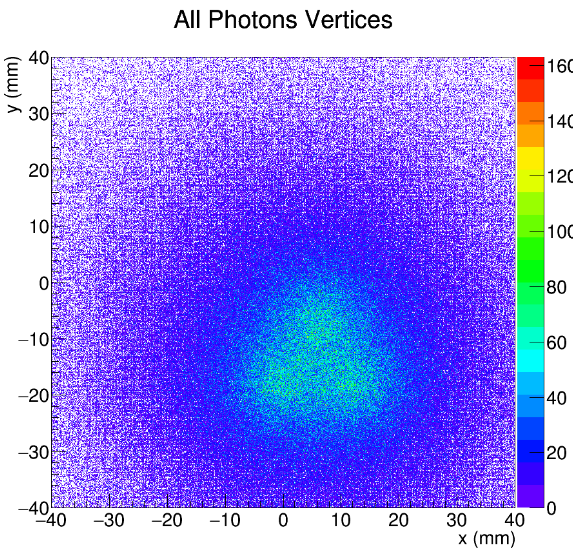


(d) Simulated image at 2 mm distance.

Figure A.16: Images with Ag-111 in 7 mm diameter cylinders of Roma phantom with varying distance between phantom and floor.

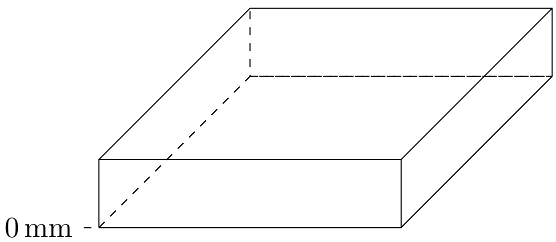


(a) Scheme at contact.

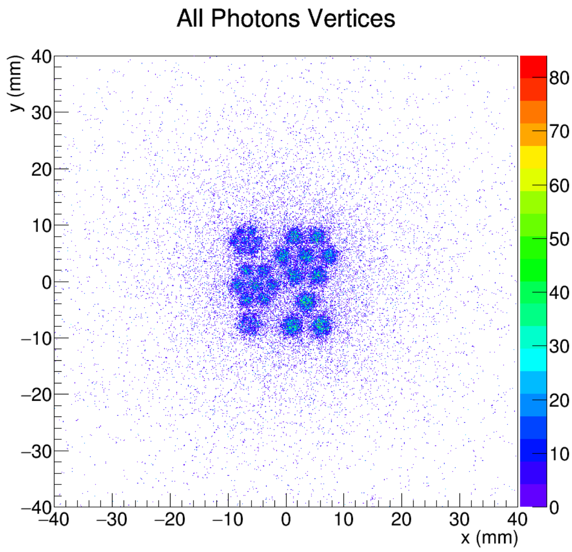


(b) Simulated image at contact.

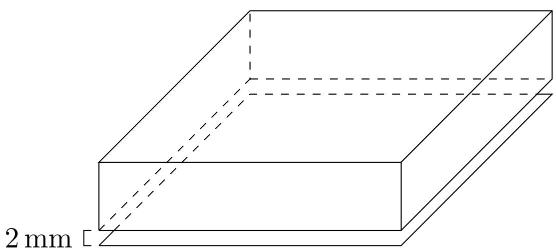


(c) Scheme at 2 mm distance.

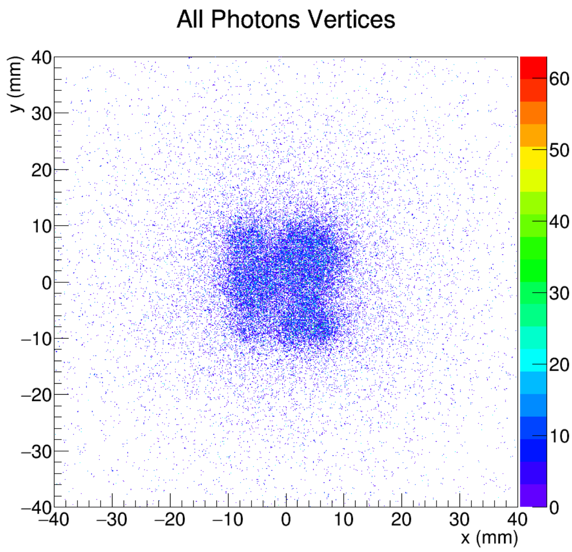


(d) Simulated image at 2 mm distance.

Figure A.17: Images with Ag-111 in PMMA phantom with varying distance between phantom and floor.

# Acronyms

**A/D** Analog-to-Digital. 19

**BLI** BioLuminescence Imaging. 17, 19

**BMI** Bruker Molecular Imaging. 21

**CAD** Computer-Aided Design. 34

**CAPiR** Center for Advanced Pre-clinical *in vivo* Research. 17, 18, 39

**CCD** Charged-Coupled Device. 5, 18, 22, 23, 25, 43

**CLI** Cerenkov Luminescence Imaging. 3, 4, 17, 19, 21, 22, 36, 44, 45, 46, 50, 59, 71, 77

**CSDA** Continuous Slowing Down Approximation. 13

**DICOM** Digital Imaging and COmmunications in Medicine. 21, 43

**DRI** Direct Radioisotopic Imaging. 3, 4, 18, 19, 21, 23, 36, 37, 44, 45, 46, 60, 64, 72, 77

**ENSDF** Evaluated Nuclear Structure DataFile. 26

**FoV** Field of View. 19

**FRI** Fluorescence Reflectance Imaging. 18

**FWHM** Full Width at Half Maximum. 61, 65

**GEANT** Generation of Events ANd Tracks. 25

**HDPE** High-Density PolyEthylene. 35, 38

**IAEA** International Atomic Energy Agency. 26

**INFN** Istituto Nazionale di Fisica Nucleare. 1

**ISOL** Isotope Separation On-Line. 1

**LNL** Legnaro National Laboratories. 1, 34, 35, 36, 37, 38, 46

**MARS** Multimodal Animal Rotation System. 21

**MOBY** MOuse whole BodY. 77

**MSFI** MultiSpectral Fluorescent Imaging. 17

**NMR** Nuclear Magnetic Resonance. 17

**NNDC** National Nuclear Data Center. 26

**PDF** Probability Density Function. 19, 30, 31

**PET** Positron Emission Tomography. 4, 34

**PLA** Poly(Lactic Acid). 37

**PMMA** Poly(Methyl MethAcrylate). 35, 38

**RIB** Radioactive Ion Beam. 1

**ROI** Region Of Interest. 21

**SI** International System of Units. 9

**SNR** Signal-to-Noise Ratio. 19, 20

**SPECT** Single-Photon Emission Computed Tomography. 4, 34

**STL** Standard Triangle Language. 37

# Bibliography


[1] Mazzocco, Marco. ‘Production and Separation of Radioactive Ion Beams’. In: *EPJ Web Conf.* 227 (2020), p. 01014. DOI: 10.1051/epjconf/202022701014. URL: https://doi.org/10.1051/epjconf/202022701014.

[2] A. Andrighetto et al. ‘The ISOLPHARM project: A New ISOL production method of high specific activity beta-emitting radionuclides as radiopharmaceutical precursors’. In: *International Journal of Modern Physics: Conference Series* 48 (2018), p. 1860103. DOI: 10.1142/S2010194518601035. eprint: https://doi.org/10.1142/S2010194518601035. URL: https://doi.org/10.1142/S2010194518601035.

[3] M. Ballan et al. ‘Development of implantation substrates for the collection of radionuclides of medical interest produced via ISOL technique at INFN-LNL’. In: *Applied Radiation and Isotopes* 175 (2021), p. 109795. ISSN: 0969-8043. DOI: https://doi.org/10.1016/j.apradiso.2021.109795. URL: https://www.sciencedirect.com/science/article/pii/S0969804321002001.

[4] P. Van Duppen. ‘Isotope Separation On Line and Post Acceleration’. In: *The Euroschool Lectures on Physics with Exotic Beams, Vol. II.* Ed. by Jim Al-Khalili and Ernst Roeckl. Berlin, Heidelberg: Springer Berlin Heidelberg, 2006, pp. 37–77. ISBN: 978-3-540-33787-4. DOI: 10.1007/3-540-33787-3_2. URL: https://doi.org/10.1007/3-540-33787-3_2.

[5] R. Formento Cavaier et al. ‘Terbium Radionuclides for Theranostics Applications: A Focus on MEDICIS-PROMED’. In: *Physics Procedia* 90.November 2016 (2017), pp. 157–163. ISSN: 18753892. DOI: 10.1016/j.phpro.2017.09.053. URL: http://dx.doi.org/10.1016/j.phpro.2017.09.053.

[6] Maria José Garcia Borge. ‘Nuclear Physics for Medicine’. In: *Nuclear Physics News* 24.2 (2014), pp. 3–4. ISSN: 19317336. DOI: 10.1080/10619127.2014.912054.

[7] F. Borgna et al. ‘A preliminary study for the production of high specific activity radionuclides for nuclear medicine obtained with the isotope separation on line technique’. In: *Applied Radiation and Isotopes* 127.November 2016 (2017), pp. 214–226. ISSN: 18729800. DOI: 10.1016/j.apradiso.2017.06.022. URL: http://dx.doi.org/10.1016/j.apradiso.2017.06.022.

[8] A. Andrighetto et al. ‘Spes: An intense source of Neutron-Rich Radioactive Beams at Legnaro’. In: *Journal of Physics: Conference Series* 966.1 (2018). ISSN: 17426596. DOI: 10.1088/1742-6596/966/1/012028.

[9] *ISOLPHARM.* URL: https://www.lnl.infn.it/en/isolpharm-2/ (visited on 18/07/2022).

[10] Istituto Nazionale di Fisica Nucleare. ‘Metodo per la produzione di radiofarmaci beta-emittenti, e radiofarmaci beta-emittenti così ottenuti’. 102014902229101 (MI2014A000145). 31st Jan. 2014. URL: https://web.infn.it/TechTransfer/index.php/it/schede-brevetti-it/477-andrighetto (visited on 20/09/2022).

[11] Michele Ballan et al. ‘Preliminary evaluation of the production of non-carrier added 111Ag as core of a therapeutic radiopharmaceutical in the framework of ISOLPHARM_Ag experiment’. In: *Applied Radiation and Isotopes* 164 (2020), p. 109258. ISSN: 0969-8043. DOI: https://doi.org/10.1016/j.apradiso.2020.109258. URL: https://www.sciencedirect.com/science/article/pii/S0969804320304085.

[12] A. Andrighetto et al. ‘The ISOLPHARM project: ISOL-based production of radionuclides for medical applications’. In: *Journal of Radioanalytical and Nuclear Chemistry* 322 (1 1st Oct.

2019), pp. 73–77. ISSN: 1588-2780. DOI: 10.1007/s10967-019-06698-0. URL: https://doi.org/10.1007/s10967-019-06698-0.

[13] The University of North Carolina at Charlotte. *Guidelines for Tumor Production in Rats and Mice*. 23rd Mar. 2020. URL: https://research.charlotte.edu/sites/research.charlotte.edu/files/media/files/iacuc/policies/rodent-tumor-load-guidelines.pdf (visited on 23/09/2022).

[14] Jürgen K. Willmann et al. 'Molecular imaging in drug development'. In: *Nature Reviews Drug Discovery* 7 (7 1st July 2008), pp. 591–607. ISSN: 1474-1784. DOI: 10.1038/nrd2290. URL: https://doi.org/10.1038/nrd2290.

[15] Michele Ballan. 'Development of targets for the production of radionuclides of medical interest according to the ISOL technique'. PhD thesis. Università degli Studi di Ferrara, 2018.

[16] Laura De Nardo. 'Nuclear imaging - Gamma camera - SPECT'. Medical Physics course. Second cycle degree in Physics. 2021.

[17] *elephant drawing illustration vector free*. URL: https://www.vectorhq.com/vector/elephant-drawing-clip-art-91637 (visited on 20/09/2022).

[18] Fabio Mammano. 'Image formation'. Biophotonics course. Second cycle degree in Physics. 11th Apr. 2021.

[19] *ImageFormation*. URL: https://svi.nl/ImageFormation (visited on 22/08/2022).

[20] Max Born et al. *Principles of Optics: Electromagnetic Theory of Propagation, Interference and Diffraction of Light*. 7th ed. Cambridge University Press, 1999. DOI: 10.1017/CBO9781139644181.

[21] M. Young. 'Pinhole Optics'. In: *Applied Optics* 10.12 (Dec. 1971), pp. 2763–2767. DOI: 10.1364/AO.10.002763. URL: http://opg.optica.org/ao/abstract.cfm?URI=ao-10-12-2763.

[22] Richard Morin and Mahadevappa Mahesh. 'Contrast Resolution Role in Medical Imaging'. In: *Journal of the American College of Radiology* 5 (7 1st July 2018), pp. 1002–1003. ISSN: 1546-1440. DOI: 10.1016/j.jacr.2018.05.002. URL: https://doi.org/10.1016/j.jacr.2018.05.002 (visited on 21/08/2022).

[23] Gregory Hollows and Nicholas James. *Contrast*. URL: https://www.edmundoptics.com/knowledge-center/application-notes/imaging/contrast/ (visited on 23/08/2022).

[24] Gregory Hollows and Nicholas James. *Resolution — Edmund Optics*. URL: https://www.edmundoptics.com/knowledge-center/application-notes/imaging/resolution/ (visited on 23/08/2022).

[25] H.J. Pfeiffer. *Physik der Radioaktivitaet und die Messung radioaktiver Strahlung*. German. Vol. 18. 1987, pp. 52–62. URL: https://inis.iaea.org/search/search.aspx?orig_q=RN:18084464.

[26] GM Currie et al. 'Radionuclide production'. In: *Radiographer* 58.3 (2011), pp. 46–52. DOI: https://doi.org/10.1002/j.2051-3909.2011.tb00155.x. eprint: https://onlinelibrary.wiley.com/doi/pdf/10.1002/j.2051-3909.2011.tb00155.x. URL: https://onlinelibrary.wiley.com/doi/abs/10.1002/j.2051-3909.2011.tb00155.x.

[27] Sóti, Zsolt, Magill, Joseph and Dreher, Raymond. 'Karlsruhe Nuclide Chart 10th edition 2018 '. In: *EPJ Nuclear Sci. Technol.* 5 (13th May 2019), p. 6. DOI: 10.1051/epjn/2019004. URL: https://doi.org/10.1051/epjn/2019004.

[28] *Radioactivity: Radioactive Activity*. URL: https://www.radioactivity.eu.com/site/pages/Radioactive_Activity.htm (visited on 17/08/2022).

[29] David B. Newell and Eite Tiesinga, eds. *The International System of Units (SI Units)*. 2019th ed. Gaithersburg: National Institute of Standards and Technology, 2019. DOI: 10.6028/NIST.SP.330-2019. URL: https://doi.org/10.6028/NIST.SP.330-2019.

[30] Lorenzo Fortunato. 'Beta Decay'. Fundamentals of Nuclear and Subnuclear Physics. First cycle degree in Physics. 18th Feb. 2019.

[31] Gordon R. Gilmore. 'Radioactive Decay and the Origin of Gamma and X-Radiation'. In: *Practical Gamma-Ray Spectrometry*. John Wiley & Sons, Ltd, 2008. Chap. 1, pp. 1–24. ISBN: 9780470861981. DOI: https://doi.org/10.1002/9780470861981.ch1. eprint: https://onlinelibrary.wiley.com/doi/pdf/10.1002/9780470861981.ch1. URL: https://onlinelibrary.wiley.com/doi/abs/10.1002/9780470861981.ch1.

[32] Craig S Levin and Edward J Hoffman. 'Calculation of positron range and its effect on the fundamental limit of positron emission tomography system spatial resolution'. In: *Physics in Medicine and Biology* 44.3 (Jan. 1999), pp. 781–799. DOI: 10.1088/0031-9155/44/3/019. URL: https://doi.org/10.1088/0031-9155/44/3/019.

[33] R. Nave. *Technetium-99m.* URL: http://hyperphysics.phy-astr.gsu.edu/hbase/Nuclear/technetium.html (visited on 18/08/2022).

[34] *National Nuclear Data Center.* URL: https://www.nndc.bnl.gov/ (visited on 28/08/2022).

[35] Travis M. Shaffer, Edwin C. Pratt and Jan Grimm. 'Utilizing the power of Cerenkov light with nanotechnology'. In: *Nature Nanotechnology* 12 (2 1st Feb. 2017), pp. 106–117. ISSN: 1748-3395. DOI: 10.1038/nnano.2016.301. URL: https://doi.org/10.1038/nnano.2016.301.

[36] J V Jelley. 'Cerenkov radiation and its applications'. In: *British Journal of Applied Physics* 6.7 (July 1955), pp. 227–232. DOI: 10.1088/0508-3443/6/7/301. URL: https://doi.org/10.1088/0508-3443/6/7/301.

[37] H. W. Koch and J. W. Motz. 'Bremsstrahlung Cross-Section Formulas and Related Data'. In: *Rev. Mod. Phys.* 31 (4 Oct. 1959), pp. 920–955. DOI: 10.1103/RevModPhys.31.920. URL: https://link.aps.org/doi/10.1103/RevModPhys.31.920.

[38] Antonello E Spinelli et al. 'Cerenkov radiation allows in vivo optical imaging of positron emitting radiotracers'. In: *Physics in Medicine and Biology* 55.2 (Dec. 2009), pp. 483–495. DOI: 10.1088/0031-9155/55/2/010. URL: https://doi.org/10.1088/0031-9155/55/2/010.

[39] F. Kulcsár, D. Teherani and H. Altmann. 'Study of the spectrum of cherenkov light'. In: *Journal of radioanalytical chemistry* 68 (1 1st Mar. 1982), pp. 161–168. ISSN: 1588-2780. DOI: 10.1007/BF02517618. URL: https://doi.org/10.1007/BF02517618.

[40] Roberto Stroili. 'Interaction of charged particles'. Introduction to Radiation Detectors. Second cycle degree in Physics. 8th Mar. 2021.

[41] Jennifer S Cho et al. 'Cerenkov radiation imaging as a method for quantitative measurements of beta particles in a microfluidic chip'. In: *Physics in Medicine and Biology* 54.22 (Oct. 2009), pp. 6757–6771. DOI: 10.1088/0031-9155/54/22/001. URL: https://doi.org/10.1088/0031-9155/54/22/001.

[42] R. L. Workman et al. 'Review of Particle Physics'. In: *PTEP* 2022 (2022), p. 083C01. DOI: 10.1093/ptep/ptac097.

[43] K. Siegbahn, ed. *Alpha-, Beta- and Gamma-Ray Spectroscopy.* First. 1st Jan. 1979. ISBN: 9780444596994.

[44] George Chabot. *How do positron and electron ranges compare?* 23rd Apr. 2007. URL: http://hps.org/publicinformation/ate/q6240.html (visited on 30/08/2022).

[45] M J Berger and Stephen M Seltzer. *Stopping powers and ranges of electrons and positrons.* Washington, DC: US. Nat. Bureau Stand. Inst. Basic Stand., 1982. URL: http://cds.cern.ch/record/139918 (visited on 07/09/2022).

[46] Martin Berger, J Coursey and M Zucker. *ESTAR, PSTAR, and ASTAR: Computer Programs for Calculating Stopping-Power and Range Tables for Electrons, Protons, and Helium Ions (version 1.21).* en. 1st Jan. 1999.

[47] J.B. Birks. 'The Theory and Practice of Scintillation Counting'. English. In: First. International series of monographs on electronics and instrumentation. Pergamon, 1964. Chap. 4, pp. 68–95. ISBN: 978-0-08-010472-0. DOI: https://doi.org/10.1016/C2013-0-01791-4. URL: https://www.sciencedirect.com/science/article/pii/B9780080104720500094.

[48] Felix Bloch. 'Über die Quantenmechanik der Elektronen in Kristallgittern'. In: *Zeitschrift für Physik* 52 (7 1st July 1929), pp. 555–600. ISSN: 0044-3328. DOI: 10.1007/BF01339455. URL: https://doi.org/10.1007/BF01339455.

[49] Manijeh Razeghi. 'Electrons and Energy Band Structures in Crystals'. In: *Fundamentals of Solid State Engineering.* Boston, MA: Springer US, 2009, pp. 1–55. ISBN: 978-0-387-92168-6. DOI: 10.1007/978-0-387-92168-6_4. URL: https://doi.org/10.1007/978-0-387-92168-6_4.

[50] J. Frenkel. 'On the Transformation of light into Heat in Solids. I'. In: *Phys. Rev.* 37 (1 Jan. 1931), pp. 17–44. DOI: 10.1103/PhysRev.37.17. URL: https://link.aps.org/doi/10.1103/PhysRev.37.17.

[51] Hans-Jürgen Wollersheim. *Scintillators.* 2017. URL: https://web-docs.gsi.de/~wolle/TELEKOLLEG/KERN/LECTURE/Wollersheim/2017/IIT-Ropar/Detector/7-Scintillation-detector.pdf (visited on 04/09/2022).

[52] Frederick Seitz. 'Interpretation of the Properties of Alkali Halide-Thallium Phosphors'. In: *The Journal of Chemical Physics* 6.3 (1938), pp. 150–162. DOI: 10.1063/1.1750216. eprint: https://doi.org/10.1063/1.1750216. URL: https://doi.org/10.1063/1.1750216.

[53] Richard R. Ernst. 'Zurich's Contributions to 50 Years Development of Bruker'. In: *Angewandte Chemie International Edition* 49.45 (2010), pp. 8310–8315. DOI: https://doi.org/10.1002/anie.201005067. eprint: https://onlinelibrary.wiley.com/doi/pdf/10.1002/anie.201005067. URL: https://onlinelibrary.wiley.com/doi/abs/10.1002/anie.201005067.

[54] *50 Years of Innovation. Bruker 1960–2010.* URL: https://www.bruker.com/en/about/history-new/_jcr_content/root/sections/section_1864966682/sectionpar/twocolumns/contentpar-1/calltoaction.download-asset.pdf/links/item0/Bruker50.pdf (visited on 18/08/2022).

[55] Richard R. Ernst. 'The Günther Laukien Prize'. In: *Journal of Magnetic Resonance* 173.2 (2005), pp. 188–191. ISSN: 1090-7807. DOI: https://doi.org/10.1016/j.jmr.2005.02.006. URL: https://www.sciencedirect.com/science/article/pii/S1090780705000273.

[56] *In-Vivo Xtreme. Preclinical Optical/X-ray Imaging System Extremely sensitive, extremely versatile, and extremely fast.* URL: https://www.accela.eu/files/products/32/xtreme_brochure_t149094.pdf (visited on 18/08/2022).

[57] Darlene E. Jenkins et al. 'Bioluminescent imaging (BLI) to improve and refine traditional murine models of tumor growth and metastasis'. In: *Clinical & Experimental Metastasis* 20 (8 1st Dec. 2003), pp. 733–744. ISSN: 1573-7276. DOI: 10.1023/B:CLIN.0000006815.49932.98. URL: https://doi.org/10.1023/B:CLIN.0000006815.49932.98.

[58] Todd A Sasser, Joshua Mchattan and Jens Waldeck. 'The Bruker In-Vivo Xtreme II System for Flexible and Sensitive Multimodal Preclinical Imaging'. 2015. URL: https://capi.lf1.cuni.cz/file/109/optical-in-vivo-xtreme-ii-system.pdf (visited on 04/08/2022).

[59] *Molecular Imaging Software.* Bruker Molecular Imaging Software User Manual. English. IB5438150 Rev. B 12/12. Bruker Corporation. 2012. 372 pp.

[60] Butch Moomaw. 'Chapter 11 - Camera Technologies for Low Light Imaging: Overview and Relative Advantages'. In: *Digital Microscopy.* Ed. by Greenfield Sluder and David E. Wolf. Vol. 114. Methods in Cell Biology. Academic Press, 2013, pp. 243–283. DOI: https://doi.org/10.1016/B978-0-12-407761-4.00011-7. URL: https://www.sciencedirect.com/science/article/pii/B9780124077614000117.

[61] Oliver E. Dial. 'CCD performance model'. In: *Surveillance Technologies.* Ed. by Sankaran Gowrinathan, Raymond J. Mataloni Sr. and Stanley J. Schwartz. Vol. 1479. International Society for Optics and Photonics. SPIE, 1991, pp. 2–11. DOI: 10.1117/12.44514. URL: https://doi.org/10.1117/12.44514.

[62] Roy D. Yates and David J. Goodman. *Probability and Stochastic Processes: A Friendly Introduction for Electrical and Computer Engineers.* John Wiley & Sons, Inc., 2014. ISBN: 978-1-118-32456-1. URL: https://www.wiley.com/en-us/Probability+and+Stochastic+Processes:+A+Friendly+Introduction+for+Electrical+and+Computer+Engineers,+3rd+Edition-p-9781118324561.

[63] Thomas J. Fellers and Michael W. Davidson. *Concepts in Digital Imaging Technology.* CCD Noise Sources and Signal-to-Noise Ratio. URL: http://hamamatsu.magnet.fsu.edu/articles/ccdsnr.html (visited on 04/08/2022).

[64] Ralf Widenhorn et al. 'Temperature dependence of dark current in a CCD'. In: *Sensors and Camera Systems for Scientific, Industrial, and Digital Photography Applications III.* Ed. by Nitin Sampat et al. Vol. 4669. International Society for Optics and Photonics. SPIE, 2002, pp. 193–201. DOI: 10.1117/12.463446. URL: https://doi.org/10.1117/12.463446.

[65] Anna Yudina and Thorsten Thiel. *Bruker BioSpin PreClinical Imaging*. In-Vivo Xtreme II Imaging Concepts. 12th Apr. 2017.

[66] Evan Doney et al. 'Planar Imaging of $^{99m}$Tc Labeled SPECT Probes in Living Mice Using the In-Vivo Xtreme Platform with Radioisotopic Phosphor Screen'. In: (June 2013), pp. 1–5.

[67] Sumith A. Kularatne et al. 'Design, Synthesis, and Preclinical Evaluation of Prostate-Specific Membrane Antigen Targeted 99mTc-Radioimaging Agents'. In: *Molecular Pharmaceutics* 6.3 (2009). PMID: 19361232, pp. 790–800. DOI: 10.1021/mp9000712. eprint: https://doi.org/10.1021/mp9000712. URL: https://doi.org/10.1021/mp9000712.

[68] Todd Sasser. *Bruker Molecular Imaging Software Overview*. URL: https://youtu.be/5lVRiNKCmb4 (visited on 18/08/2022).

[69] R.H. Elrick and R.P. Parker. 'The use of Cerenkov radiation in the measurement of $\beta$-emitting radionuclides'. In: *The International Journal of Applied Radiation and Isotopes* 19.3 (1968), pp. 263–271. ISSN: 0020-708X. DOI: https://doi.org/10.1016/0020-708X(68)90023-9. URL: https://www.sciencedirect.com/science/article/pii/0020708X68900239.

[70] R Robertson et al. 'Optical imaging of Cerenkov light generation from positron-emitting radiotracers'. In: *Physics in Medicine and Biology* 54.16 (July 2009), N355–N365. DOI: 10.1088/0031-9155/54/16/n01. URL: https://doi.org/10.1088/0031-9155/54/16/n01.

[71] *IVIS Imaging systems*. Comparison Table. URL: https://resources.perkinelmer.com/lab-solutions/resources/docs/SHT_011713C_01_IVIS_Comparison_Table.pdf (visited on 07/08/2022).

[72] Gwilz. *Vector diagram of laboratory mouse (black and white)*. 20th Dec. 2013. URL: https://commons.wikimedia.org/wiki/File:Vector_diagram_of_laboratory_mouse_(black_and_white).svg (visited on 28/08/2022).

[73] M J Yaffe and J A Rowlands. 'X-ray detectors for digital radiography'. In: *Physics in Medicine and Biology* 42.1 (Jan. 1997), pp. 1–39. DOI: 10.1088/0031-9155/42/1/001. URL: https://doi.org/10.1088/0031-9155/42/1/001.

[74] Ayush Goel and Peerzada Mohammad Iflaq. *Intensifying screen*. 11th Mar. 2022. URL: https://radiopaedia.org/articles/30319 (visited on 23/08/2022).

[75] Douglas L. Vizard et al. 'Electronic imaging system for autoradiography'. US6346707B1 (United States). 28th July 1998.

[76] Stephen Seltzer and J. Hubbell. *X-Ray Mass Attenuation Coefficients. Tables of X-Ray Mass Attenuation Coefficients and Mass Energy-Absorption Coefficients from 1 keV to 20 MeV for Elements Z = 1 to 92 and 48 Additional Substances of Dosimetric Interest*. 17th Feb. 2022. DOI: 10.18434/T4D01F. URL: https://www.nist.gov/pml/x-ray-mass-attenuation-coefficients (visited on 09/08/2022).

[77] *In-Vivo Xtreme*. Bruker In-Vivo Xtreme Imaging System User manual. English. IB5438663 Rev. D 12/12. Bruker Corporation. 2012. 214 pp.

[78] *Overview*. geant4.web.cern.ch. URL: https://geant4.web.cern.ch/ (visited on 17/08/2022).

[79] R Brun et al. *GEANT 3: user's guide Geant 3.10, Geant 3.11; rev. version*. Geneva: CERN, 1987. URL: https://cds.cern.ch/record/1119728.

[80] R Brun et al. *Simulation program for particle physics experiments, GEANT: user guide and reference manual*. Geneva: CERN, 1978. URL: https://cds.cern.ch/record/118715.

[81] S. Agostinelli et al. 'Geant4—a simulation toolkit'. In: *Nuclear Instruments and Methods in Physics Research Section A: Accelerators, Spectrometers, Detectors and Associated Equipment* 506.3 (2003), pp. 250–303. ISSN: 0168-9002. DOI: https://doi.org/10.1016/S0168-9002(03)01368-8. URL: https://www.sciencedirect.com/science/article/pii/S0168900203013688.

[82] Steffen Hauf et al. 'Radioactive Decays in Geant4'. In: *IEEE Transactions on Nuclear Science* 60.4 (Aug. 2013), pp. 2966–2983. DOI: 10.1109/TNS.2013.2270894. arXiv: 1307.0996 [physics.comp-ph]. URL: https://doi.org/10.1109%5C%2Ftns.2013.2270894.

[83] Jagdish K. Tuli. 'Evaluated Nuclear Structure Data File and Related Products'. In: *AIP Conference Proceedings* 769.1 (2005), pp. 265–267. DOI: 10.1063/1.1945002. eprint: https:

//aip.scitation.org/doi/pdf/10.1063/1.1945002. URL: https://aip.scitation.org/doi/abs/10.1063/1.1945002.

[84] P. Truscott et al. 'Geant4-a new Monte Carlo toolkit for simulating space radiation shielding and effects'. In: *2000 IEEE Radiation Effects Data Workshop. Workshop Record. Held in conjunction with IEEE Nuclear and Space Radiation Effects Conference (Cat. No.00TH8527).* IEEE, July 2000, pp. 147–152. ISBN: 0-7803-6474-0. DOI: 10.1109/REDW.2000.896281.

[85] Robley D. Evans. *The Atomic Nucleus.* Tata McGraw-Hill Publishing Company Ltd., 1955.

[86] Esther Ciarrocchi and Nicola Belcari. 'Cerenkov luminescence imaging: physics principles and potential applications in biomedical sciences'. In: *EJNMMI Physics* 4.1 (2017). ISSN: 21977364. DOI: 10.1186/s40658-017-0181-8.

[87] *Physics Processes.* URL: https://geant4-userdoc.web.cern.ch/UsersGuides/ForApplicationDevelope html/TrackingAndPhysics/physicsProcess.html#scintillation (visited on 19/08/2022).

[88] Siddharth Misra et al. 'Chapter 2 - Unsupervised clustering methods for noninvasive characterization of fracture-induced geomechanical alterations'. In: *Machine Learning for Subsurface Characterization.* Ed. by Siddharth Misra, Hao Li and Jiabo He. Gulf Professional Publishing, 2020, pp. 39–64. ISBN: 978-0-12-817736-5. DOI: https://doi.org/10.1016/B978-0-12-817736-5.00006-5. URL: https://www.sciencedirect.com/science/article/pii/B9780128177365000065.

[89] Eric W. Weisstein. *Convolution.* From MathWorld–A Wolfram Web Resource. URL: https://mathworld.wolfram.com/Convolution.html (visited on 03/09/2022).

[90] *About ROOT.* analyzing petabytes of data, scientifically. URL: https://root.cern/about/ (visited on 16/08/2022).

[91] Rene Brun et al. *root-project/root: v6.18/02.* Version v6-18-02. Aug. 2019. DOI: 10.5281/zenodo.3895860. URL: https://doi.org/10.5281/zenodo.3895860.

[92] *Jaszczak con Flangia.* ELSE Solutions. URL: https://www.elsesolutions.com/prodotti/nuclear-medicine/quality-control/phantoms/deluxe-jaszczak/ (visited on 30/08/2022).

[93] Albert Hirtl et al. 'Technical Note: Fully-automated analysis of Jaszczak phantom measurements as part of routine SPECT quality control'. In: *Medical Physics* 44.5 (2017), pp. 1638–1645. DOI: https://doi.org/10.1002/mp.12150. eprint: https://aapm.onlinelibrary.wiley.com/doi/pdf/10.1002/mp.12150. URL: https://aapm.onlinelibrary.wiley.com/doi/abs/10.1002/mp.12150.

[94] *About FreeCAD.* URL: https://wiki.freecadweb.org/About_FreeCAD (visited on 04/08/2022).

[95] Josef Prusa. *General Info.* Prusa Knowledge. URL: https://help.prusa3d.com/article/general-info_1910 (visited on 07/08/2022).

[96] Mary Jo Zimbro et al., eds. *Difco™ & BBL™ Manual.* Manual of Microbiological Culture Media. Second. Becton, Dickinson and Company, 2009. ISBN: 0-9727207-1-5. URL: https://legacy.bd.com/ds/technicalCenter/misc/difcobblmanual_2nded_lowres.pdf (visited on 30/08/2022).

[97] *Crai Pellicola Per alimenti 15 metri.* URL: https://www.craispesaonline.it/prodotto/bosa-via-delle-conce/14185-crai-pellicola-per-alimenti-15-metri (visited on 30/08/2022).

[98] *Medicina Nucleare.* PET. URL: https://www.ospedale-cannizzaro.it/utente/reparti-e-servizi/medicina-nucleare-pet/ (visited on 25/08/2022).

[99] PTW-FREIBURG. *CURIEMENTOR® 3 Isotope Calibrator.* Isotope Calibrator for Radionuclide Activity Measurement in Nuclear Medicine. D610.219.0/3. Sept. 2005. URL: http://www.cpce.ru/tools/leaflet/Cur%5C%203%5C%20new.pdf (visited on 19/09/2022).

[100] Caroline A Schneider, Wayne S Rasband and Kevin W Eliceiri. 'NIH Image to ImageJ: 25 years of image analysis'. In: *Nature Methods* 9 (7 July 2012), pp. 671–675. DOI: 10.1038/nmeth.2089. URL: https://doi.org/10.1038/nmeth.2089.

[101] *Introduction.* URL: https://imagej.nih.gov/ij/docs/intro.html (visited on 19/08/2022).

[102] *Features.* URL: https://imagej.nih.gov/ij/features.html (visited on 19/08/2022).

[103] N. Sultanova, S. Kasarova and I. Nikolov. 'Dispersion Properties of Optical Polymers'. In: *Acta Physica Polonica A* 116.4 (2009), pp. 585–587. DOI: 10.12693/APhysPolA.116.585. URL: https://bibliotekanauki.pl/articles/1795587.

[104] Donald R. Smith and Ernest V. Loewenstein. 'Optical constants of far infrared materials. 3: plastics'. In: *Applied Optics* 14.6 (June 1975), pp. 1335–1341. DOI: 10.1364/AO.14.001335. URL: http://opg.optica.org/ao/abstract.cfm?URI=ao-14-6-1335.

[105] George M. Hale and Marvin R. Querry. 'Optical Constants of Water in the 200-nm to 200-$\mu$m Wavelength Region'. In: *Appl. Opt.* 12.3 (Mar. 1973), pp. 555–563. DOI: 10.1364/AO.12.000555. URL: http://opg.optica.org/ao/abstract.cfm?URI=ao-12-3-555.

[106] Alberto Arzenton. 'Monte Carlo based dosimetry using PET/CT and SPECT/CT imaging in radiopharmaceutical therapy in the context of the ISOLPHARM project'. MA thesis. Università degli Studi di Padova, 2021.

[107] Arun Gupta et al. 'Preclinical voxel-based dosimetry through GATE Monte Carlo simulation using PET/CT imaging of mice'. In: *Physics in Medicine & Biology* 64.9 (Apr. 2019), p. 095007. DOI: 10.1088/1361-6560/ab134b. URL: https://doi.org/10.1088/1361-6560/ab134b.

[108] William.P. Segars et al. 'Development of a 4-D digital mouse phantom for molecular imaging research'. In: *Molecular Imaging & Biology* 6.3 (2004), pp. 149–159. ISSN: 1536-1632. DOI: https://doi.org/10.1016/j.mibio.2004.03.002. URL: https://www.sciencedirect.com/science/article/pii/S1536163204002173.